

# Sheffield Hallam University

*Electro-chemical development of CuInGaSe<sub>2</sub>-based photovoltaic solar cells.*

TOLAN, Gavin James.

Available from the Sheffield Hallam University Research Archive (SHURA) at:

<http://shura.shu.ac.uk/20444/>

## A Sheffield Hallam University thesis

This thesis is protected by copyright which belongs to the author.

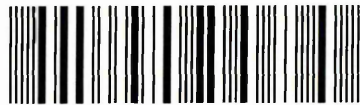
The content must not be changed in any way or sold commercially in any format or medium without the formal permission of the author.

When referring to this work, full bibliographic details including the author, title, awarding institution and date of the thesis must be given.

Please visit <http://shura.shu.ac.uk/20444/> and <http://shura.shu.ac.uk/information.html> for further details about copyright and re-use permissions.

Sheffield S1 1WB

101 911 088 0



Sheffield Hallam University  
Learning and IT Services  
Adsetts Centre City Campus  
Sheffield S1 1WB

**REFERENCE**

ProQuest Number: 10701090

All rights reserved

INFORMATION TO ALL USERS

The quality of this reproduction is dependent upon the quality of the copy submitted.

In the unlikely event that the author did not send a complete manuscript and there are missing pages, these will be noted. Also, if material had to be removed, a note will indicate the deletion.



ProQuest 10701090

Published by ProQuest LLC (2017). Copyright of the Dissertation is held by the Author.

All rights reserved.

This work is protected against unauthorized copying under Title 17, United States Code  
Microform Edition © ProQuest LLC.

ProQuest LLC.  
789 East Eisenhower Parkway  
P.O. Box 1346  
Ann Arbor, MI 48106 – 1346

**Electro-Chemical Development of  $\text{CuInGaSe}_2$   
based Photovoltaic Solar Cells**

Gavin James Tolan

A thesis submitted in partial fulfilment of the requirements of  
Sheffield Hallam University  
for the degree of Doctor of Philosophy

October 2008

“We have at our disposal three main sources of life-sustaining energy; fuel, water-power and the heat of the sun's rays...If we use our fuel to get our power, we are living on our capital and exhausting it rapidly. This method is barbarous and wantonly wasteful, and will have to be stopped in the interest of coming generations. The heat of the sun's rays represents an immense amount of energy vastly in excess of waterpower...”

Nikola Tesla 1916

## Abstract

The aim of this work was to make low cost, high efficiency, graded bandgap, thin film CuInGaSe<sub>2</sub> solar cells by electrodeposition, using novel device designs proposed by Dharmadasa et al. These new designs were first experimentally tested using well researched GaAs and Al<sub>x</sub>Ga<sub>(1-x)</sub>As materials grown using MOCVD, these ideas were then transferred to electrodeposited CuInGaSe<sub>2</sub>.

New designs of graded bandgap solar cells based on p-type window materials, using the well researched GaAs and Al<sub>x</sub>Ga<sub>(1-x)</sub>As alloy system, have been experimentally tested. The size of the cell was gradually scaled up from 0.5 mm diameter (0.002 cm<sup>2</sup>) to 3×3 mm<sup>2</sup> (0.090 cm<sup>2</sup>) and to 5×5 mm<sup>2</sup> (0.250 cm<sup>2</sup>), these were then assessed using I-V and QE techniques. The devices showed V<sub>oc</sub> in the range of 1070-1175 mV, exceeding reported values, FF in the range 0.80-0.87, and J<sub>sc</sub> in the range 11-12 mA cm<sup>-2</sup>. The reason for the low current density was believed to be due to the GaAs capping layer used in the device, which acted as a filter. To confirm this, a second set of devices was fabricated, replacing the GaAs cap with GaAlP, this increased the J<sub>sc</sub> to ~ 14 mA cm<sup>-2</sup>, V<sub>oc</sub> and FF remained the same.

New PV device structures based on CuInGaSe<sub>2</sub> starting from the front contact, instead of the conventional Mo back contact, have been grown by electrodeposition from aqueous solutions using a single bath. In order to investigate the effect of bath concentrations on the film properties, 3 different bath concentrations were used. PEC was used to determine the electrical conduction of these layers, and it was found that it was possible to grow p<sup>+</sup>, p, i, n, n<sup>+</sup> layers by changing the deposition voltage. XRF was used to determine the stoichiometry of the corresponding layers, and XRD to investigate the bulk structure. The morphological properties were studied using AFM and SEM. A four-layer n-n-i-p solar cell structure was initially fabricated and I-V measurements were carried out to assess the devices. The devices were PV active with parameters V<sub>oc</sub>~235 mV, J<sub>sc</sub>~22 mA cm<sup>-2</sup>, FF~0.38 and η~2.0%.

Due to problems annealing CdS at high temperature and the difficulty of incorporating gallium into the layer, CuInSe<sub>2</sub> cells with Mo as the substrate were deposited. To understand the mechanisms of film growth, detailed cyclic voltammetry was carried out, leading to the construction of a Pourbaix diagram for the Cu-In-Se system. Depositing the films at -0.476 V for 20 minutes, followed by 50 minutes at -0,576 mV gave the best quality films, with p-type electrical conduction. XRF and XRD were used to determine stoichiometry and structural properties respectively. A method to anneal the CuInSe<sub>2</sub> layers without the use of H<sub>2</sub>Se was devised, and a detailed study using SEM to determine the effects of annealing time and temperature was carried out. Annealing the films at 550°C for 30 minutes gave the best results. I-V measurements were carried out using an electrolyte contact, the devices were photo active, (V<sub>oc</sub>~866 mV, J<sub>sc</sub>~0.9 mA cm<sup>-2</sup>, FF~0.40).

Abstract	i
Contents	ii
Overview of thesis	vii
List of abbreviations and symbols	ix
Acknowledgments	xi
<b>Chapter 1: Introduction</b>	<b>1</b>
1.1 Background	1
1.2 Types of solar cells	
1.2.1 First and second generation cells	3
1.2.2 Third Generation cells	5
1.3 How photovoltaic cells work	6
1.3.1 P-N junction	8
1.3.2 Metal-semiconductor junction	10
1.3.2.1 The rectifying contact (Schottky barrier)	11
1.3.2.2 The ohmic contact	13
1.3.2.3 The MIS contact	14
1.3.2.4 Dangling bonds and Fermi level pinning	16
<b>Chapter 2: Background to CuInGaSe<sub>2</sub> (CIGS) based Solar Cells</b>	<b>17</b>
2.1 Properties of CuInSe <sub>2</sub> and its alloys	17
2.1.1 Introduction	17
2.1.2 Advantages of I-III-VI <sub>2</sub> compound for thin film Photovoltaic devices	17
2.1.3 Crystallography of CuInSe <sub>2</sub>	19
2.2 Deposition Techniques	21
2.2.1 Physical Vapour Deposition (PVD)	21
2.2.2 Chemical Vapour Deposition (CVD)	22
2.2.3 Molecular Beam Epitaxy (MBE)	22
2.2.4 Chemical Bath Deposition (CBD)	23
2.2.5 Spray Pyrolysis	23
2.2.6 Flash Evaporation	23

2.2.7	Pulsed Laser Deposition (PLD)	24
2.2.8	Electrodeposition (ED)	24
2.3	CuInGaSe <sub>2</sub> (CIGS) solar cells current development	26
2.3.1	Introduction	26
2.3.2	Effects of sodium	28
2.3.3	Effects of sulphur	29
2.3.4	Effects of gallium	30
2.3.5	ODC layer (Ordered Defect Compound)	31
2.4	Buffer layers	32
2.4.1	Cadmium Sulphide (CdS) buffer layer	32
2.4.2	Alternative buffer layers	34
<b>Chapter 3:</b>	<b>Electrodeposition</b>	<b>36</b>
3.1	Introduction	36
3.2	Theory	36
3.2.1	Nucleation and growth	38
3.3	Electrochemical diagrams	39
3.3.1	Pourbaix diagrams	39
3.3.1.1	Reactions used to plot Cu-In-Se system Pourbaix diagram	40
3.3.2	Cyclic Voltamogram	42
3.4	Double Layer	43
3.4.1	Helmholtz Layer	43
3.4.2	Gouy-Chapman Layer	43
3.5	Three Electrode Cell	45
3.6	Electrodeposition of CuInSe <sub>2</sub>	46
<b>Chapter 4:</b>	<b>Characterisation Techniques</b>	<b>47</b>
4.1	Material characterisation	47
4.1.1	Introduction	47
4.1.2	X-Ray Diffraction (XRD)	47
4.1.1.2	Glancing angle X-ray diffraction	49

4.1.3	Photoelectrochemical Cell (PEC)	52
4.1.4	Scanning Electron Microscopy (SEM)	53
4.1.5	Atomic Force Microscopy (AFM)	54
4.1.5.1	Introduction	54
4.1.5.2	Principle of AFM	55
4.1.6	X-Ray Fluorescence (XRF)	56
4.1.7	Optical absorption	56
4.1.7.1	UV-visible spectroscopy	58
4.2	Device characterisation	59
4.2.1	Introduction	59
4.2.2	Current Voltage measurements (I-V)	59
4.2.3	Quantum Efficiency (QE)	63
4.2.4	Capacitance voltage measurements (C-V)	64
<b>Chapter 5:</b>	<b>Development of AlGaAs devices with p-type window material</b>	<b>66</b>
5.1	Introduction	66
5.2	Background to the development of the 'new model'	66
5.2.1	The new model (~2002)	67
5.3	Experimental	71
5.3.1	Details of MOCVD growth	71
5.4	I-V and QE results	72
5.4.1	First batch (0.002 cm <sup>2</sup> ) 0.5 mm diameter solar cells	72
5.4.2	Second batch (0.090 cm <sup>2</sup> ) 3×3 mm <sup>2</sup> solar cells	74
5.4.3	Third batch (0.250 cm <sup>2</sup> ) 5×5 mm <sup>2</sup> solar cells	76
5.4.4	Calculation of other parameters from I-V data	78
5.5	Capacitance Voltage measurements (C-V)	78
5.6	Discussion of results	79
5.7	Second growth of Al <sub>x</sub> Ga <sub>(1-x)</sub> As/GaAs devices	80
5.8	Summary	82

<b>Chapter 6:</b>	<b>Characterisation of FTO and CdS</b>	<b>83</b>
6.1	Fluorine doped Tin Oxide (FTO)	83
6.1.1	XRD analysis of FTO	83
6.1.2	SEM of TEC-7	86
6.1.3	AFM of TEC-7 and TEC-15	86
6.1.4	Optical absorption	87
6.1.5	Four point probe measurements	88
6.2	Cadmium Sulphide (CdS) growth and characterisation	89
6.2.1	Introduction	89
6.2.2	Experimental	89
6.2.3	XRD analysis of CdS	89
6.2.4	Thickness measurements	91
6.2.5	Photoelectrochemical measurements (PEC)	91
6.2.6	Optical absorption	92
6.2.7	SEM analysis.	93
6.3	Summary	94
<b>Chapter 7:</b>	<b>Development of CuInGaSe<sub>2</sub> superstrate devices</b>	<b>95</b>
7.0	Introduction	95
7.1	Electrodeposition of CuInGaSe <sub>2</sub>	95
7.1.1	Linear Sweep Voltametry (LVS) and PEC	97
7.2	PEC analysis	98
7.3	XRD analysis	100
7.3.1	XRD as a function of bath concentration	101
7.3.2	XRD as a function of deposition voltage	101
7.4	XRF investigation	105
7.4.1	Influence of bath concentration	106
7.4.2	Influence of deposition voltage	106
7.5	SEM analysis	107
7.6	Summary of main results for material characterisation	109
7.7	I-V characteristics of preliminary superstrate nnip devices	110
7.8	Discussion of results and conclusions	112

<b>Chapter 8:</b>	<b>Development of CuInSe<sub>2</sub> substrate devices</b>	<b>114</b>
8.1	Introduction	114
8.2	Electrodeposition of CuInSe <sub>2</sub>	114
8.2.1	Cyclic Voltametry (CV)	115
8.2.1.1	Cu-Se-In system	115
8.2.1.2	Cu-In-Se system	117
8.2.1.3	Mechanism of film growth	118
8.3	XRF and XRD analysis of as-deposited samples	120
8.4	Thickness measurements	122
8.5	Annealing conditions	124
8.6	SEM study of effects of annealing under different conditions	125
8.6.1	Effect of temperature and addition of selenium pellets	125
8.6.2	Effect of annealing temperature	126
8.6.3	Effect of annealing time	127
8.7	AFM analysis	129
8.8	XRD analysis	129
8.8.1	Three voltage deposition	129
8.8.2	Effect of annealing	130
8.9	I-V characteristics	132
8.10	Discussion of results and conclusions	134
<b>Chapter 9:</b>	<b>Conclusions and future work</b>	<b>136</b>
	References	139
	List of publications	152

## Overview of thesis

This work is divided into 9 chapters, the first 4 chapters provide an introduction to photovoltaics, the background to  $\text{CuInSe}_2$  based solar cells, the theory of electrodeposition and the characterisation techniques used. The following 4 chapters constitute the bulk of the work carried out, where the experimental results are presented covering AlGaAs devices with p-type window material, FTO and CdS, superstrate  $\text{CuInGaSe}_2$  devices and substrate  $\text{CuInSe}_2$  devices. In the final chapter future work is discussed.

Chapter 1 summarises the different types of solar cells, and outlines the reasons why  $\text{CuInGaSe}_2$  is a good material for inexpensive high efficiency thin film solar cells. It also explains the theory of semiconductor junctions.

Chapter 2 describes  $\text{CuInSe}_2$  in detail, covering the crystallography and properties of  $\text{CuInSe}_2$ . A brief review of deposition techniques used by other groups and industry is given, along with the current development of  $\text{CuInSe}_2$  base solar cells, including the role of the buffer layer.

Chapter 3 describes the electrodeposition technique, which includes the theory of electrodeposition, the construction of the  $\text{CuInSe}_2$  Pourbaix diagram and a description of the 3-electrode cell, which was the deposition method used in this work.

Chapter 4 gives a description of the characterisation techniques, which can be split into two groups: i) material characterisation and ii) device characterisation.

Chapter 5 has a brief description of the background leading to the development of the 'new model', explaining how it relates to most thin film solar cells. The experimental results of the scaling-up process of AlGaAs devices, which are based upon this new model, are also given.

Chapter 6 covers the characterisation of FTO, which is the material on which the  $\text{CuInGaSe}_2$  layer is grown for a superstrate configuration cell. The growth and characterisation of the CdS buffer layer is also detailed.

Chapter 7 describes the development of  $\text{CuInGaSe}_2$  superstrate devices, which includes experimental details of the electrodeposition process, characterisation of the material and results of device performance.

Chapter 8 describes the development of  $\text{CuInSe}_2$  substrate devices, which includes detailed experiments on the electrodeposition of the Cu-In-Se system and an explanation for the mechanism of film growth. The material characterisation results and I-V characteristics are also given.

Chapter 9 discusses future work.

## List of abbreviations and symbols

### Abbreviations

AFM	Atomic Force Microscopy
CBD	Chemical Bath Deposition
CuInGaSe <sub>2</sub>	Copper Indium Gallium Diselenide
CuInSe <sub>2</sub>	Copper Indium Diselenide
CV	Capacitance Voltage
CVD	Chemical Vapour Deposition
EBIC	Electron Beam Induced Current
ED	Electrodeposition
FF	Fill Factor
FTO	Fluorine doped Tin Oxide
I <sub>sc</sub>	Short Circuit Current
ICPMS	Inductively Coupled Plasma Mass Spectrometry
I-V	Current Voltage
JCPDS	Joint Committee on Powder Diffraction Standards
J <sub>sc</sub>	Short Circuit Current Density
MBE	Molecular Beam Epitaxy
MOCVD	Metal-Organic Chemical Vapour Deposition
ODC	Ordered Defect Compound
PEC	Photoelectrochemical Cell
PLD	Pulsed Laser Deposition
PVD	Physical Vapour Deposition
QE	Quantum Efficiency
RTA	Rapid Thermal Anneal
SEM	Scanning Electron Microscopy
SHU	Sheffield Hallam University
SIMS	Secondary Ion Mass Spectroscopy
V <sub>oc</sub>	Open Circuit Voltage
XRF	X-Ray Fluorescence

## Symbols

$\alpha$	Absorption coefficient
$A^*$	Effective Richardson constant
$a_p$	Activity product
$a_r$	Activity reactant
$c$	Speed of light
$e$	Magnitude of electron charge
$\epsilon_0$	Permittivity of free space
$\epsilon_r$	Relative permittivity
$E_0$	Standard reference potential
$F$	Faradays constant
$\phi_b$	Potential barrier height
$\phi_m$	Work function of metal
$\phi_s$	Work function of semiconductor
$G$	Gibbs free energy
$h$	Planks constant
$k$	Boltzmann constant
$N_A$	Acceptor concentration
$N_D$	Donor concentration
$n_i$	Intrinsic charge carrier density
$\rho$	Density
$R$	Gas constant
$T$	Temperature K
$t$	Time (s)
$\nu$	Frequency
$V_{bi}$	Built in potential

## Acknowledgements

I wish to thank Sheffield Hallam University for the funding of this project, and all the academic and technical staff within the MERI.

I would also like to thank Professor Dharmadasa, Professor Jan Evans-Freeman and Dr Samantilleke, for the wealth of experience they brought to this project, which through many useful discussions guided me in the right direction.

Also many thanks to our industrial partners in this project, Ionotec Ltd and Pilkington Group plc, especially Steve Heavens and Paul Warren, for their help and support.

# Chapter 1: Introduction

## 1.1 Background

Worldwide energy consumption is expected to grow by 57% over the next 20 years, with most of this supplied by fossil fuels [1]. Due to limited resources and environmental factors, alternative energy sources are needed. It couldn't be a more important time for the renewable industry as a whole to increase efficiency, bring down production cost and sell its benefits to governments and the public, to fill the ever widening 'energy gap'. With the worldwide consensus to reduce carbon emissions many countries now think this gap can only be filled by nuclear power. However there is only 50 years supply of uranium (if used at the present rate), the carbon cycle of a nuclear plant is certainly nowhere near zero [2] and there is still no ideal solution to the legacy of radioactive waste products.

Despite the concern over energy consumption, worldwide use of renewables is projected to increase by only 38% over the next 20 years [1] from its current figure of 5% (240 GW) [1]. Renewable energy sources mainly include hydro-electric, wind, solar, wave and tidal.

There are 3 major processes for converting solar energy.

1. Heliochemical - The photosynthesis process
2. Heliothermal -
  - i) Hot water panels
  - ii) Hot air engines (e.g. Stirling engine)
  - iii) Convection tower, for electricity production [3]
  - iv) Concentrating collection to drive steam turbines
3. Helioelectrical - Photovoltaic (solar cells)

Photovoltaics could play a major part but their efficiency must be increased and production costs reduced, in order to be viable for large scale energy production.

## 1.2 Types of solar cells

At present solar cells can be categorised by 3 groups:

**First generation** - Si and GaAs single crystal cells.

**Second generation** - Thin film Si, CIGS and CdTe.

**Third generation**. - Solar cells incorporating tunnel junctions, quantum wells, impact ionisation, impurity photovoltaics, dyes, polymers, graded band gap multi-layers and numerous others.

Figure 1.1 shows how the transition from first and second generation cells to third generation cells is expected to reduce cost and increase efficiency.

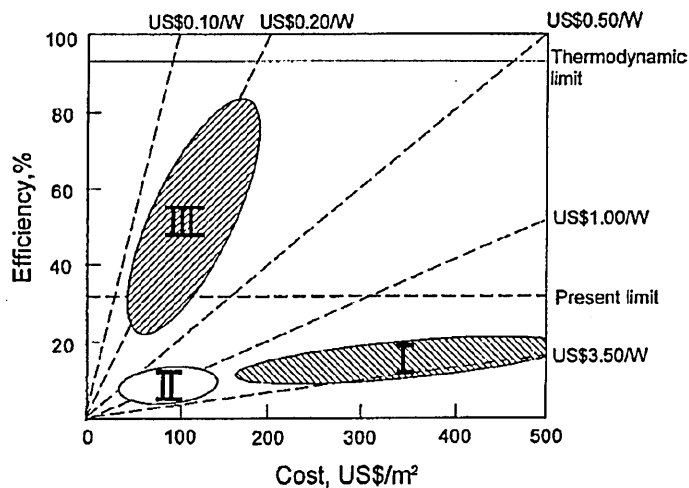


**Figure 1.1.** Efficiency and cost projections for first, second and third generation photovoltaic technology (wafers, thin-films and advanced thin films, respectively) [4].

Figure 1.2 shows how the efficiencies of the best research cells for different materials and types of cell have progressed from 1975 to the present day [5].

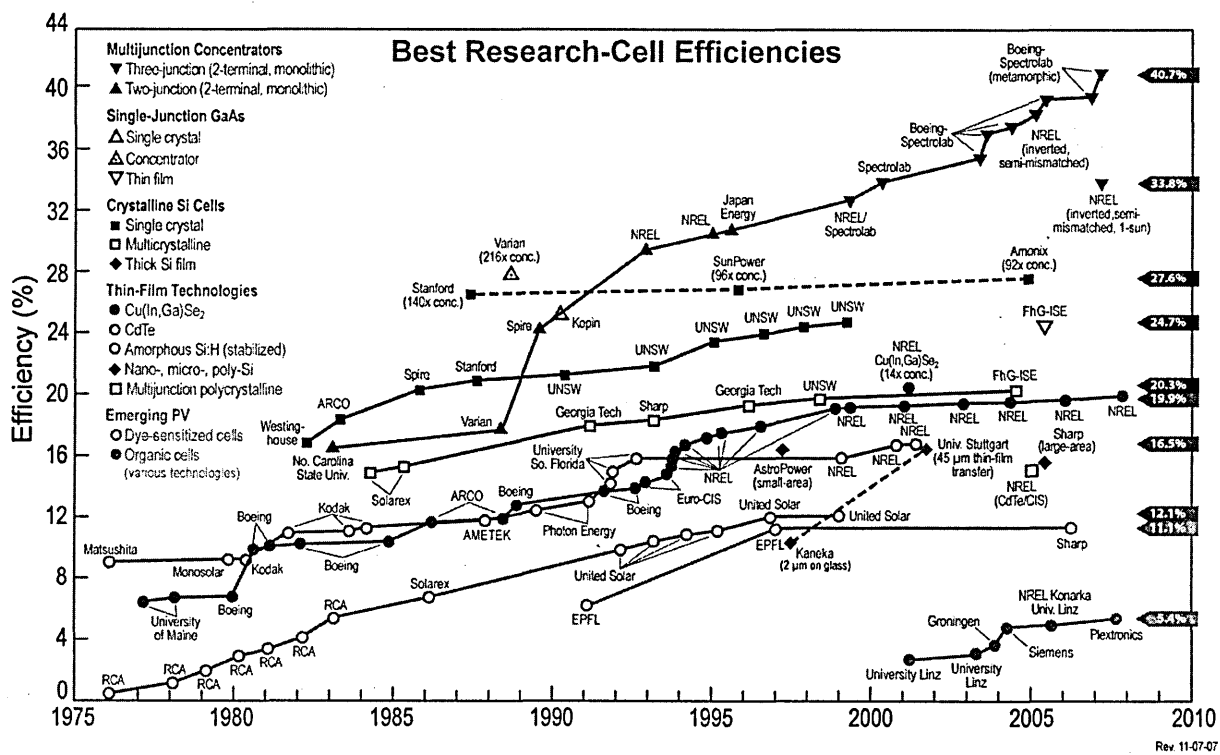


Figure 1.2. Best research cell efficiencies for the main types of cells and materials [5].

### 1.2.1 First and Second Generation Single Junction Solar Cells

Although there is a great deal of research into new materials and designs of solar cells to improve efficiency and reduce the cost, most solar cells presently sold on the market are based on silicon wafers [6]. Although these have achieved efficiencies of 22.7% for single junction large area devices [7], these are expensive single crystal devices requiring complicated fabrication techniques with 50% of the solar panels total cost being due to cost of the silicon wafer [6].

However there are less expensive silicon routes; Sandia/HEM have produced multicrystalline silicon cells with 15.3% efficiency [7]. Pacific Solar have manufactured polycrystalline thin film silicon cells with 8.2% efficiency [8] and amorphous silicon cells have been fabricated directly onto large area glass substrates, reducing the cost with efficiencies of 10.6% on 910×455 mm<sup>2</sup> modules [9].

Cadmium telluride has a band gap close to the optimum 1.4 eV and it is relatively easy to deposit thin films by various techniques giving an efficiency close to 16% [10]. BP

Solar have manufactured large area CdTe monolithic thin film modules with efficiencies of 10.7% [4]. The CdTe solar cell has had some marketing issues due to the toxic nature of cadmium, but the perception is rapidly changing. The large amount of Cd (~20000 tonnes per annum) produced as a by product of mining zinc, is used in Ni/Cd batteries, with the rest ending up in landfill. CdTe solar cells in fact clean up the environment by locking up the Cd in less toxic CdTe, producing clean energy for the future.

III-V solar cells are based on compounds of group III and V elements and show high conversion efficiencies 25.1% for crystalline GaAs [7] and 21.9% for crystalline InP [7], measured under the global AM 1.5 spectrum. III-V's are expensive single crystal cells (usually grown by MOCVD and MBE) and are suited to concentrator systems as the size of the cell can be kept small. The highest efficiency for a single junction concentrator cell is 27.8% [7], using crystalline GaAs with an intensity of 216 suns. With concentrator cells it is also necessary to use a 2 axis tracking system which again adds to the cost. The III-V compounds usually used are gallium arsenide or indium phosphide and are alloyed with Al and Sb to create the desired bandgap.

CuInSe<sub>2</sub> (CIS) and its alloy family with gallium (CIGS) and sulphur (CIGSS) has become one of the most important materials in developing polycrystalline thin film solar cells. Its high absorption coefficient ( $\alpha > 10^5 \text{ cm}^{-1}$ ) [11] and the ability to tailor the bandgap from 1.0 eV – 2.4 eV by changing the In/Ga and Se/S ratios are the main reasons for its use in thin film solar cells [12]. Also stability appears to be not a problem, long term outdoor testing, tests at elevated temperatures and space operation have proved there is no decline in performance [13]. CIGS solar cells have achieved 19.9% efficiencies for lab scale devices [14] and over 13% for large area devices [15].

The aim of the industry worldwide is to produce 2.5 GW of thin film panels by 2011, and to reduce the cost from €124 per m<sup>2</sup> to €30 per m<sup>2</sup> and for CIS related panels to capture 25% of the market by 2020.

### 1.2.2 Third generation solar cells.

Third generation cells refer to cells which are expected to achieve ultra high efficiencies, with conversion values in the range of 45-60%. Listed are a few of the common device designs/concepts which fall into this category.

i) Multi junction cells where individual cells are stacked with the uppermost having the highest bandgap, they have a theoretical conversion efficiency of 86.6% for an infinite stack [4], and lab scale devices to date have achieved efficiencies of 30.3% [16] for 2-junction and 33.3% [17] for 3-junction solar cells. But there are some disadvantages with this approach and removal of these disadvantages could lead to further improvement of device efficiencies [18].

ii) Multiple electron hole pairs per photon; high energy photons use their excess energy to create additional electron hole pairs. This would give an internal quantum efficiency above unity and a theoretical conversion efficiency of 85.4% [4].

Quantum efficiency over unity was first explained by Antocit in 1957 [19] as being due to impact ionisation. This was then verified with experimental work by Koc, Vavilov and Britsyn on silicon and germanium in the late 50's, which yielded quantum efficiencies above unity [18].

iii) Impurity photovoltaics; standard cells rely on electrons being excited from the valence band to the conduction band of the semiconductor, but efficiency can be improved if a third band or impurity level is added, which acts as a kind of 'stepping stone'. This theory has been extended to  $n$  number of bands and the theoretical efficiency of 86.6% has been calculated [4].

Most of the mechanisms mentioned above are incorporated into the 'new model' which has been designed by the SHU group [20].

### 1.3 How Photovoltaic Cells Work

Solar energy reaches the earth as solar radiation, which are distinct packets of energy or photons, with energy  $E$  given by;

$$E = h\nu = \frac{hc}{\lambda}$$

Where symbols have their usual meaning.

Solar radiation covers the range 300 - 2500 nm (4.0 - 0.5 eV) with most of this energy in the visible spectrum (see Figure 1.3). An ideal solar cell would absorb all the energy in this range.

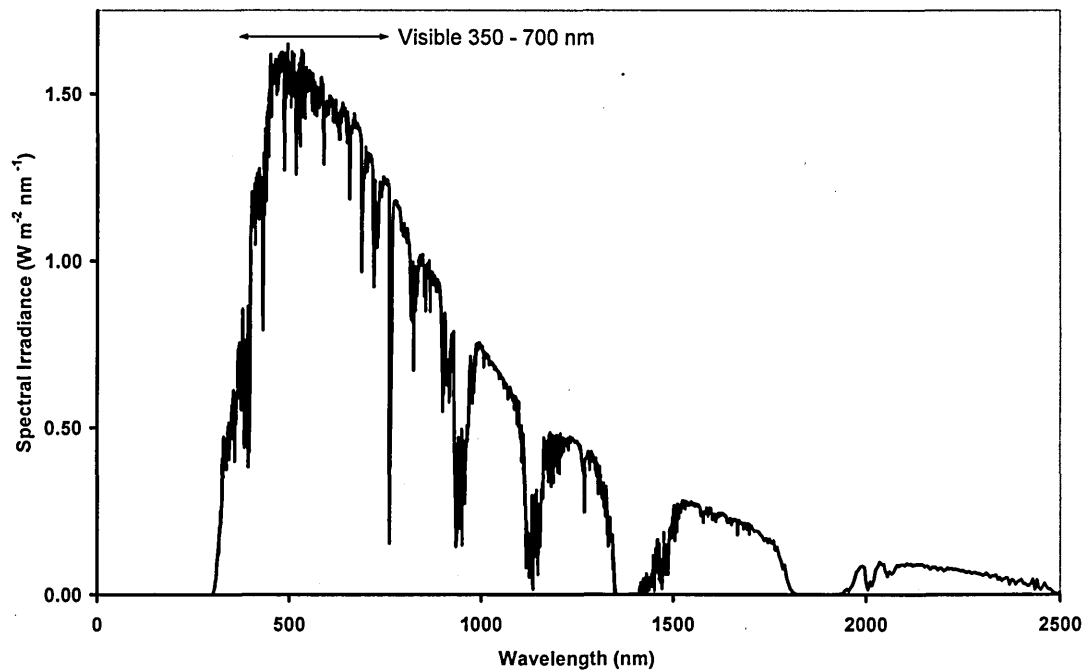


**Figure 1.3.** Standard solar reference spectrum under air mass 1.5 (AM 1.5) conditions.

In a semiconductor, absorption of light happens when the photon has sufficient energy to excite electrons across the energy gap, creating an electron hole pair. If the energy is too low, i.e. not enough energy to excite the electrons, light is not absorbed. If the energy is too high, an electron hole pair is created but the excess energy causes heating in the crystal lattice through thermalisation process which reduces efficiency.

Therefore for a given irradiation there are restrictions for the choice of semiconductor whose properties are suitable for a solar cell, i.e. there must be sufficient absorption of light and the bandgap must match the irradiation.

Theoretical calculations show that semiconductors with bandgaps of 1.0 - 1.8 eV are suitable for solar energy conversion, with an optimum of 1.4 eV [21].

For the electron hole pairs to be useful, recombination must be prevented. To achieve this, an internal electric field is built into the device to separate the electrons and holes, which can then be collected to produce a current in an external circuit.

This electric field gradient is produced by making an interface between two materials and is what lies behind the basis of all semiconductor devices. The p-n junction is the most common and is described in the next section. This can take many forms for example; the homojunction, where the junction is formed from a p-type and an n-type semiconductor of the same material. The heterojunction, the solar cell device consists of two different semiconductors, one with a larger bandgap than the other, in this way the efficiency of the device can be increased, as each material can be matched to different parts of the solar spectrum. Another important junction is the metal-semiconductor junction, this is necessary in all electronic device structures, to connect the device to the external circuit. These junctions can show either rectifying or ohmic behaviour.

### 1.3.1 P-N junction

A basic p-n junction is a device with an n-type semiconducting layer (rich in electrons) and a p-type semiconducting layer (rich in holes) [22].

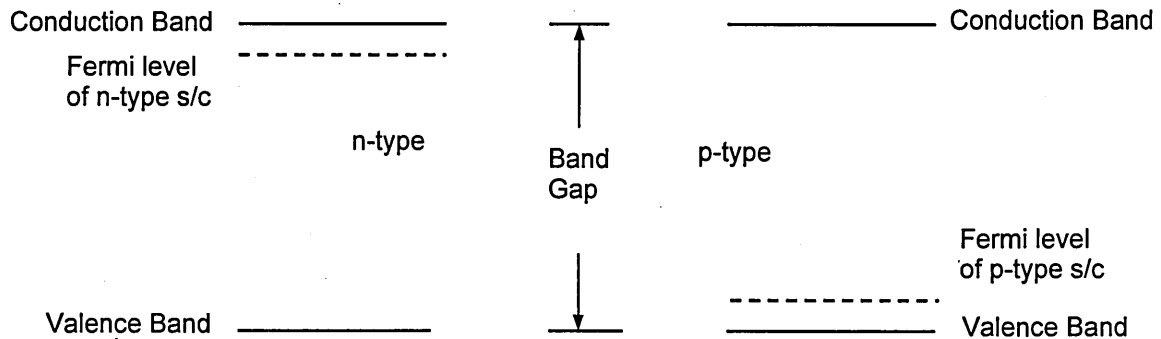


**Figure 1.4.** Band diagrams the showing relative positions of the Fermi levels of an n-type and p-type semiconductor before contact.

When the material is initially brought into contact, free electrons from the n-side and free holes from the p-side diffuse across the junction. When an electron meets a hole recombination takes place and as a result the junction area becomes depleted of electrons and holes. Therefore positively charged ionised donors on the n-side and negatively charged ionised acceptors on the p-side will be left behind in the junction area. These two charged layers produce the internal electric field  $E_i$ , required for the device.

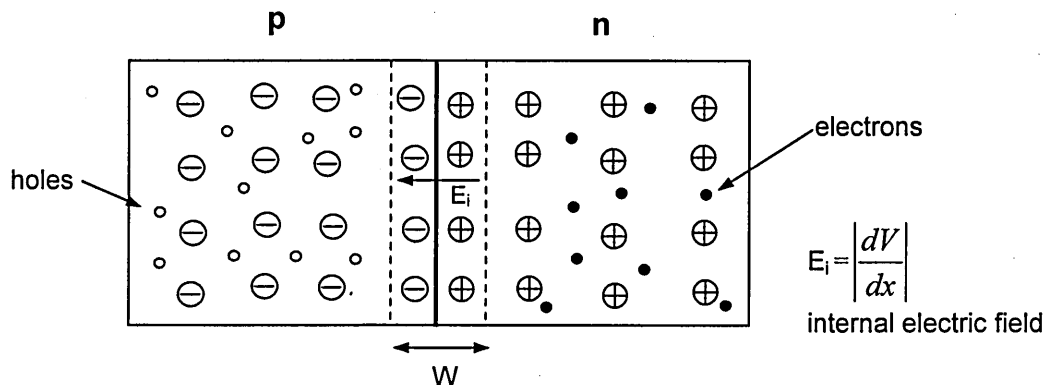


**Figure 1.5.** Schematic diagram of a p-n junction.

This process builds up a space charge region (SCR) around the junction with the resulting internal electric field opposing any more free carrier movement. This initial carrier diffusion down a concentration gradient causes a diffusion current, which is balanced by the opposing drift current with all the free charge carriers having flown out of the junction region.

When the two currents are in equilibrium, there is no net current flow across the junction, the region is depleted of any moving charge (either side of the junction), and hence is called the depletion zone, which typically extends about  $1\ \mu\text{m}$  either side of the junction depending on the doping concentration, leaving the bulk of the material unchanged. Now as there is no net current flow, the system is in equilibrium. Therefore the Fermi level must be the same throughout the materials system and to accommodate this, the valence and conduction bands need to be bent; this results in the formation of a potential barrier between the two sides. This potential is known as 'the built in potential' ( $V_{bi}$ ) and acts as a barrier, keeping the junction swept clean of majority carriers.

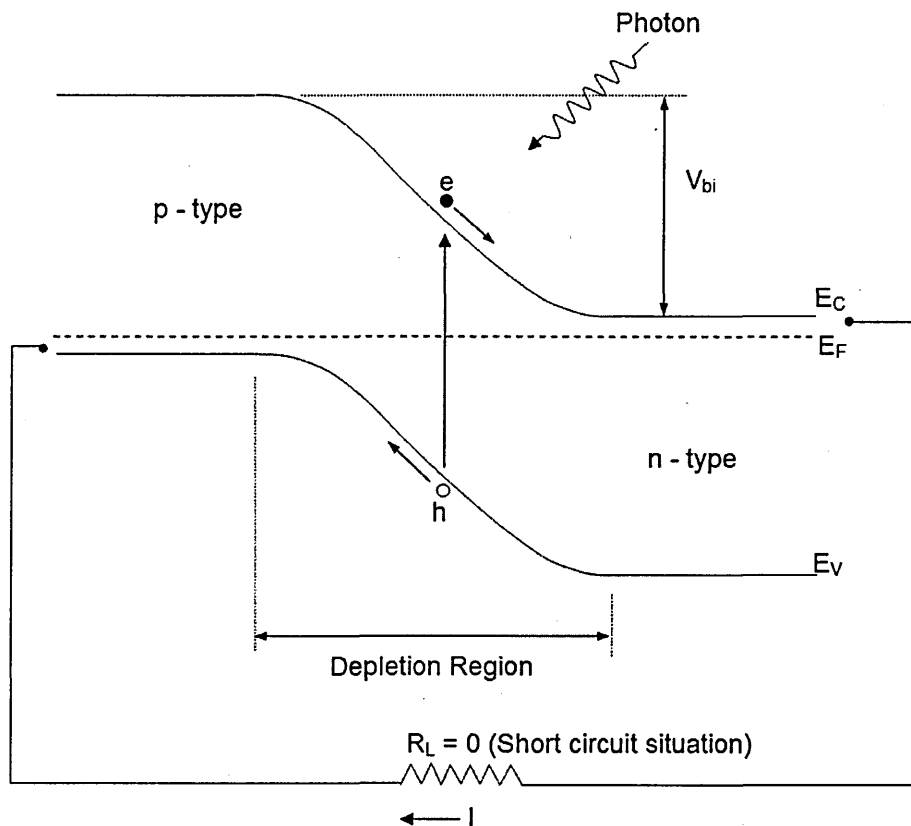


**Figure 1.6.** The band diagram of a p-n junction under illumination, and the representation of the photovoltaic activity.

The built-in potential  $V_{bi}$  of the device is given by;

$$V_{bi} = \frac{E_g}{e} - (V_n + V_p) = \frac{kT}{e} \ln \left( \frac{N_A N_D}{n_i^2} \right) \quad (1.1)$$

Where  $k$  = Boltzmann constant,  $T$  = temperature,  $e$  = magnitude of electronic charge,  $N_A$  = acceptor concentration (p-side),  $N_D$  = donor concentration (n-side) and  $n_i$  = intrinsic charge carrier density.

The width of the depletion layer is given by;

$$w = \sqrt{\left[ \frac{2V_{bi} \epsilon_0 \epsilon_s (N_A + N_D)}{e N_A N_D} \right]} \quad (1.2)$$

When the p-n junction is illuminated and if the incoming photon has enough energy to excite an electron across the bandgap, an electron hole pair will be created. If this pair can diffuse to the depletion region before recombination, photogenerated charge carriers will be separated and this will cause charge to flow through an external load.

### 1.3.2 The metal-semiconductor junction.

Metal-semiconductor contacts are another important system in electronic devices; they either show rectifying or ohmic behaviour. Rectifying contacts allow current flow in one direction only, while ohmic contacts allow current flow in both directions. The nature of the contact is dependant on the Fermi levels of both the semiconductor and the metal [22].

**Table 1.1.**

	Semiconductor	
	n-type	p-type
$\phi_m > \phi_s$	rectifying	ohmic
$\phi_m < \phi_s$	ohmic	rectifying

### 1.3.2.1 The rectifying contact (Schottky barrier).

The rectifying contact is based on the theory developed by Schottky (1938) and Mott in the same year and hence is known as the Mott-Schottky theory, although the junction formed is generally termed as a Schottky barrier [22].

This is very similar to the p-n junction, in that for the Fermi levels to be in equilibrium at the junction the energy bands must bend accordingly. For an n-type semiconductor, if  $\phi_m > \phi_s$ , when the metal and semiconductor are put in contact some of the electrons in the semiconductor move spontaneously into the metal and are collected on the surface. These leave behind positive ions on the n-side and create a negative surface charge on the metal. Figure 1.7 shows the different energy levels in the metal and the semiconductor with respect to the vacuum level before contact.

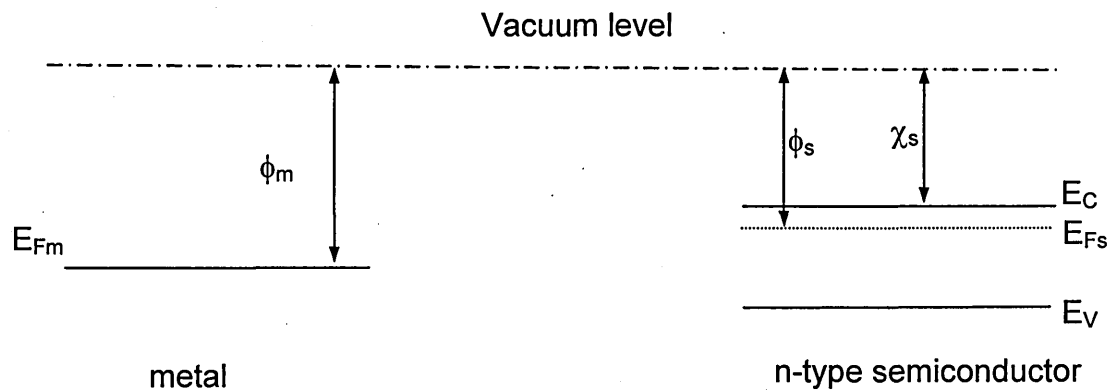


**Figure 1.7.** Band diagram showing relative positions of the Fermi levels before contact of a metal and an n-type semiconductor.

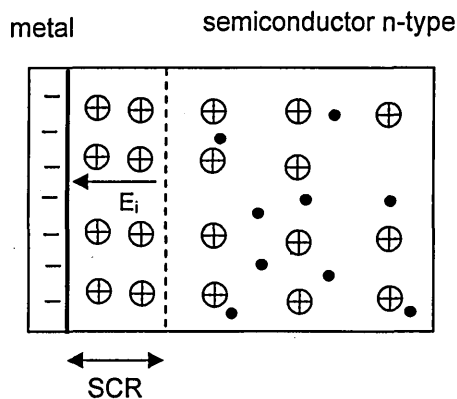


**Figure 1.8.** Schematic diagram of a metal and n-type semiconductor junction.

An electric field is set up, that eventually inhibits any further flow of electrons into the metal. This positively charged region within the semiconductor is depleted of electrons and hence is called the depletion region (or SCR). The width can be calculated using the same equation given for a p-n junction, with slight modification. In equilibrium the Fermi level of the semiconductor and the metal must be constant throughout the system, to accommodate this, the valence and conduction bands are forced to bend upwards at the junction, as shown in figure 1.9. The built in potential,  $V_{bi}$  is given by the difference in the two work functions.

$$V_{bi} = \phi_m - \phi_s \quad (1.3)$$

For an ideal Schottky barrier the height of the barrier is given by;

$$\phi_b = \phi_m - \chi_s \quad (1.4)$$

Where  $\chi_s$  is the electron affinity of the semiconductor.

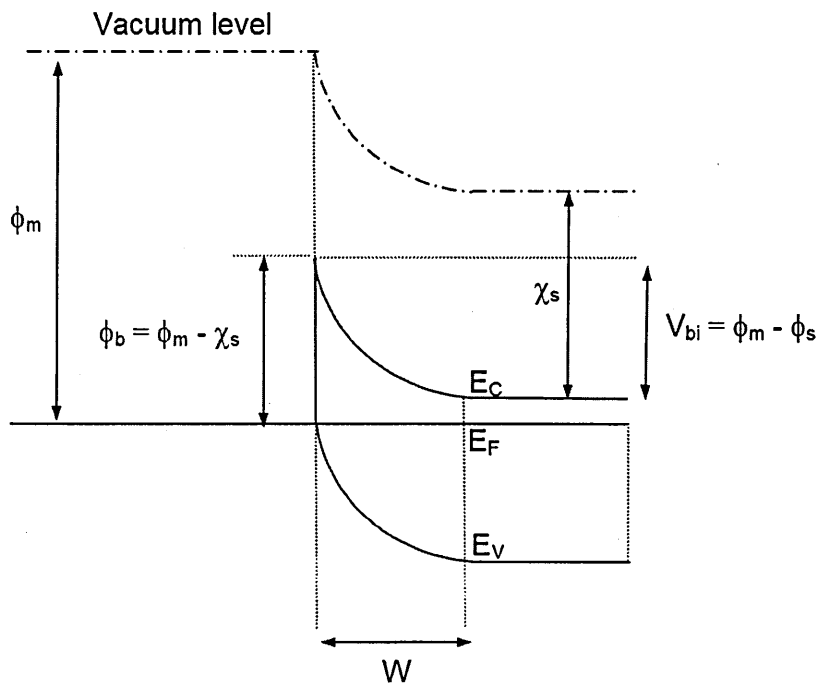


**Figure 1.9.** Band diagram for a metal/n-type semiconductor contact, with  $\phi_m > \phi_s$  after contact.

For a p-type semiconductor with  $\phi_m < \phi_s$ , electrons flow from the metal into the semiconductor, a positively charged layer will be built up on the surface of the metal and a negatively charged close to the surface of the semiconductor. At equilibrium, the Fermi level will align forcing a band bending. The built in potential is given by:

$$V_{bi} = \phi_s - \phi_m \quad (1.5)$$

and

$$\phi_b = E_g - (\phi_m - \chi_s) \quad (1.6)$$

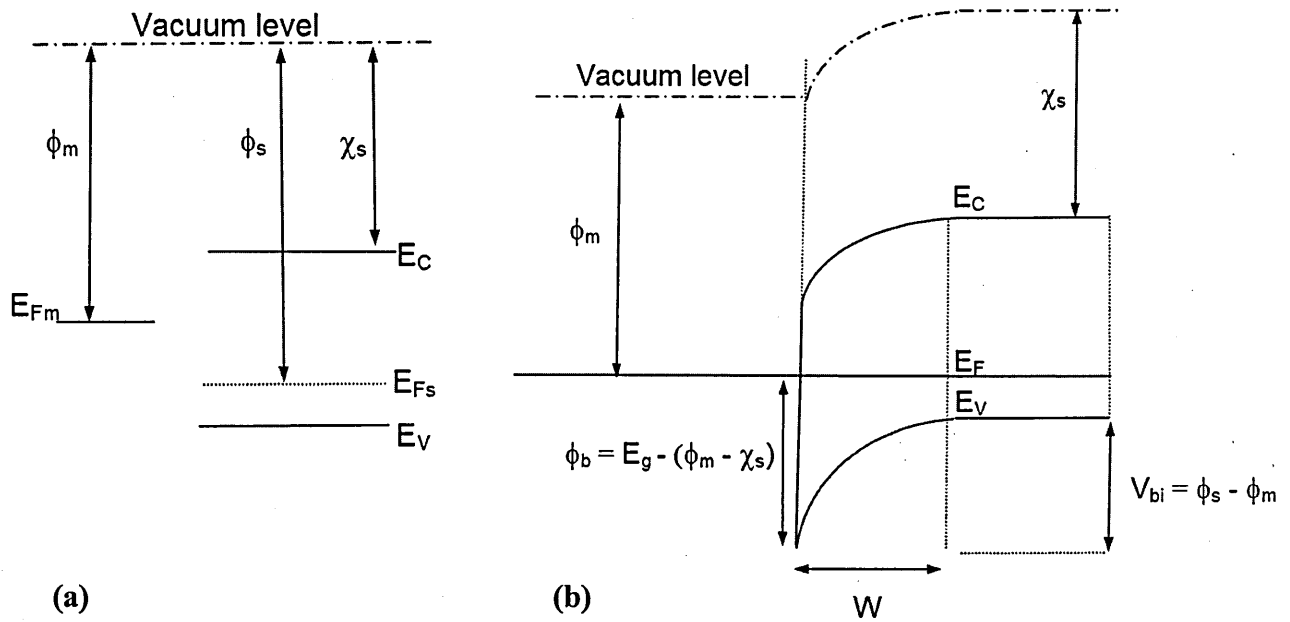


**Figure 1.10.** Band diagram for a metal/p-type semiconductor contact with  $\phi_m < \phi_s$  (a) before contact and (b) after contact.

### 1.3.2.2 The ohmic contact

The ohmic contact is far more common in electronic devices than the rectifying contact, as it is needed to connect the device to external circuitry. Ohmic contacts ideally should have no potential barrier between the metal and semiconductor; this will lead to a linear I-V characteristic in both biasing directions with a low contact resistance. The conditions for an ohmic contact are  $\phi_m < \phi_s$  for an n-type semiconductor and  $\phi_m > \phi_s$  for a p-type. In practice a small thin barrier will exist, and to minimise this, the

semiconductor is heavily doped at the interface. This results in a very thin barrier layer, which can easily be overcome by thermionic emission, external biasing or by tunnelling.

### 1.3.2.3 The Metal Insulator Semiconductor (MIS) contact

A MIS structure is the most useful electronic device in the study of semiconductor surfaces, since most interfaces in reality will have an oxide layer (insulator), whether intentional or not. The MIS structure was first proposed in 1959 by Moll and by Pfann and Garrett, for use as a varistor (variable capacitor) [22]. Its main application today is in Metal Oxide Silicon (MOS) semiconductors and the MIS inversion layer solar cell [22].

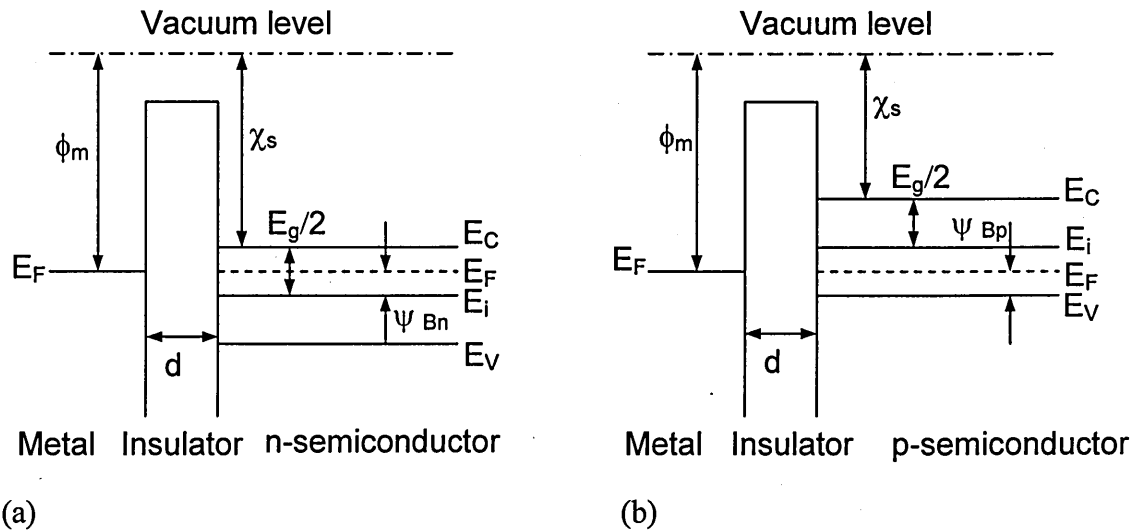


**Figure 1.11.** Energy band diagrams of ideal MIS diodes at  $V=0$ , (a) n-type semiconductor and (b) p-type semiconductor.

An ideal MIS diode is defined as, at zero bias voltage the difference between the metal and semiconductor energy levels is zero, or  $\phi_{ms} = 0$ . The conditions represented by figure 1.11 are equivalent to:

$$\phi_{ms} = \phi_m - \left( \chi + \frac{E_g}{2e} - \psi_{Bn} \right) = 0 \quad \text{For n-type} \quad (1.7)$$

$$\phi_{ms} = \phi_m - \left( \chi + \frac{E_g}{2e} + \psi_{Bp} \right) = 0 \quad \text{For p-type} \quad (1.8)$$

Which is to say there is a flat band condition when there is no applied voltage (figure 1.11). When an ideal MIS diode is biased with a positive or negative voltage, one of three cases will exist. For this purpose only the p-type semiconductor will be described in detail.

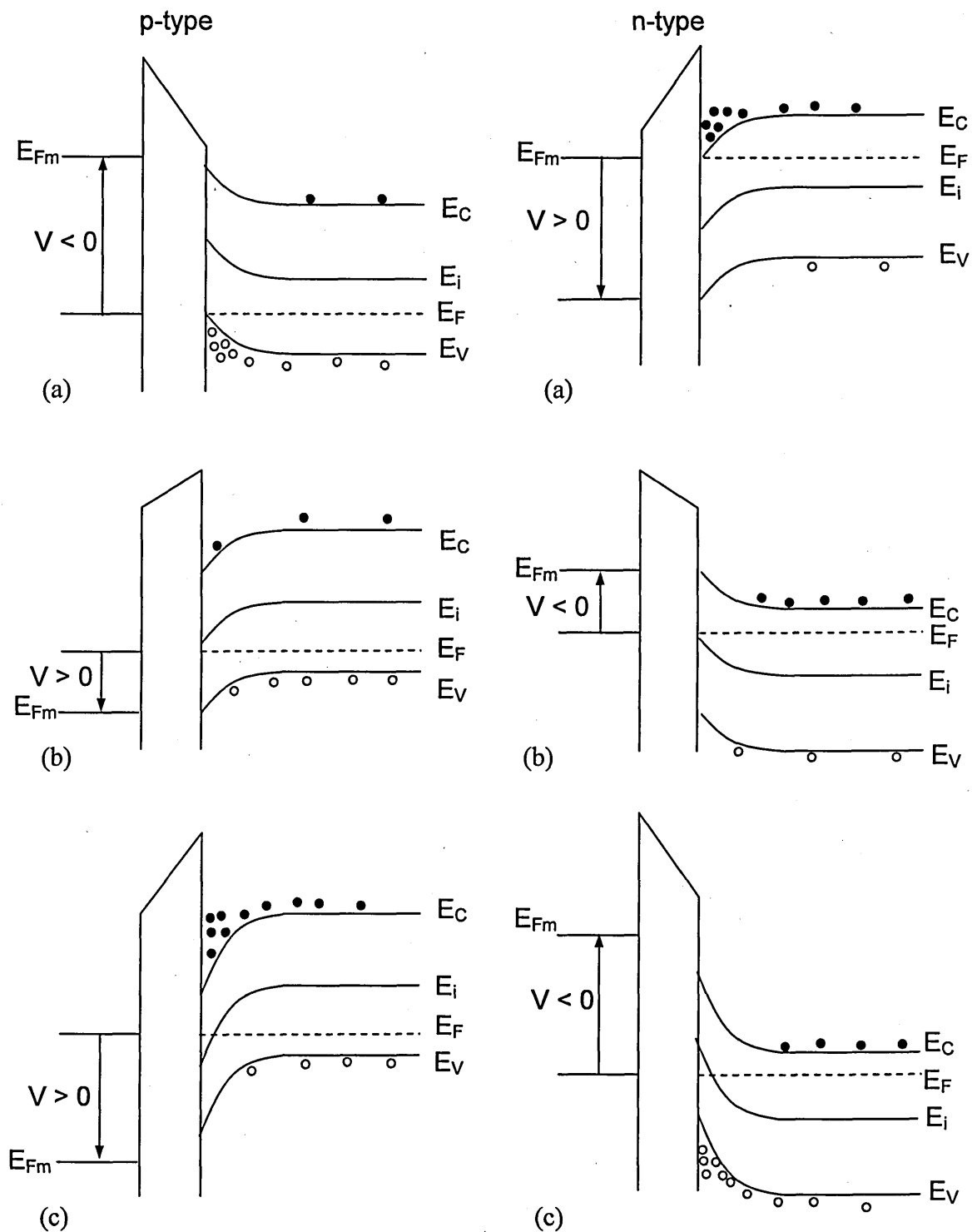


**Figure 1.12.** Energy band diagrams for ideal MIS diodes under different bias conditions, (a) accumulation, (b) depletion and (c) inversion.

When a negative voltage ( $V < 0$ ) is applied to the metal, the valence band will bend up near the surface, which will bring it closer to the Fermi Level (figure 1.12a). In an ideal situation there is no current flow and the Fermi level will remain constant within the semiconductor. The band bending will however cause a majority carrier accumulation (holes) near the surface of the semiconductor. This is called the accumulation case. When there is a small positive voltage applied ( $V > 0$ ), the bands will bend down, and the majority carriers will be depleted (figure 1.12b). This is the depletion case. If the positive voltage is increased further, the bands will bend downwards even more, causing the intrinsic Fermi level ( $E_i$ ) and the semiconductor Fermi level ( $E_F$ ) to cross. At this point the number of electrons (minority carriers) becomes greater than that of holes (figure 1.12c). This is the inversion case. A similar result can be obtained for an n-type semiconductor, but the polarity of the voltages must be inverted (figure 1.13 n-type).

### 1.3.2.3 Dangling bonds and Fermi level pinning

Mott-Schottky theory only applies to an ideal system, as it doesn't take into account interface and surface states. A dangling bond occurs at the surface of a semiconductor and is caused by the atoms only having neighbours on one side, to which it can bind. Therefore some electrons are unpaired which are termed as dangling bonds. These dangling bonds can act as donors, and are responsible for surface defect states. These states generate a barrier which can have either a positive or negative charge at the surface. If the density of states is large and comparable with the doping concentration of the semiconductor, the barrier height will become independent of the metal work function and the Fermi level is said to be 'pinned' (Fermi level pinning) [23].

In the silicon solar cell industry it is a well known technique to passivate these dangling bonds with hydrogen (hydrogen passivation). It is now becoming evident that the buffer layer in CIGS solar cells, whether it is CdS,  $\text{In}_2\text{Se}_3$ , ZnS etc, passivates the surface states and pins the Fermi level [23,24]. The buffer layer with a small thickness in the order of 100 nm acts as a passivation layer, rather than providing the 'n' part of a p-n junction, this is explained later in chapter 2.4 of this thesis.

## Chapter 2: Background to CuInSe<sub>2</sub> based solar cells

### 2.1 Properties of CuInSe<sub>2</sub> and its alloys

#### 2.1.1 Introduction

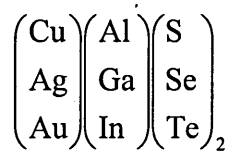
Copper Indium Diselenide (CuInSe<sub>2</sub>) and its alloys are complex compounds of the group I-III-VI<sub>2</sub> semiconductors, and have several interesting properties which make them suitable for high efficiency photovoltaic devices.

- Direct bandgap of ~ 1.04 eV
- High optical absorption coefficient ( $\alpha > 10^5 \text{ cm}^{-1}$ )
- Possibility to produce n- and p- type material by intrinsic doping
- Many suitable deposition techniques

#### 2.1.2 Advantages of I-III-VI<sub>2</sub> compounds for thin film Photovoltaic devices

CuInSe<sub>2</sub> has a relatively small bandgap of 1.04 eV, but by the partial substitution of In with Ga to form Cu(InGa)Se<sub>2</sub> and Se with S, the bandgap can be systematically tailored between 1.04 eV and 2.43 eV, making it possible to produce a graded bandgap PV device capable of absorbing a major part of the solar spectrum.

Other possible compounds can consist of a combination of the following elements.



One of these CuInGaSe<sub>2</sub> or CIGS is a material explored extensively for the development of low cost, high efficiency thin film solar cells over the past decade. CIGS cells have produced 19.9% efficiency for lab scale devices [14] and over 13% efficiency for large scale devices [15].

**Table 2.1.** Bandgaps of ternary semiconductors in the chalcopyrite family.

Compound	$E_g$ (eV)
CuInSe <sub>2</sub>	1.04
CuGaSe <sub>2</sub>	1.68
CuInS <sub>2</sub>	1.55
CuGaS <sub>2</sub>	2.43
CuAlSe <sub>2</sub>	2.67

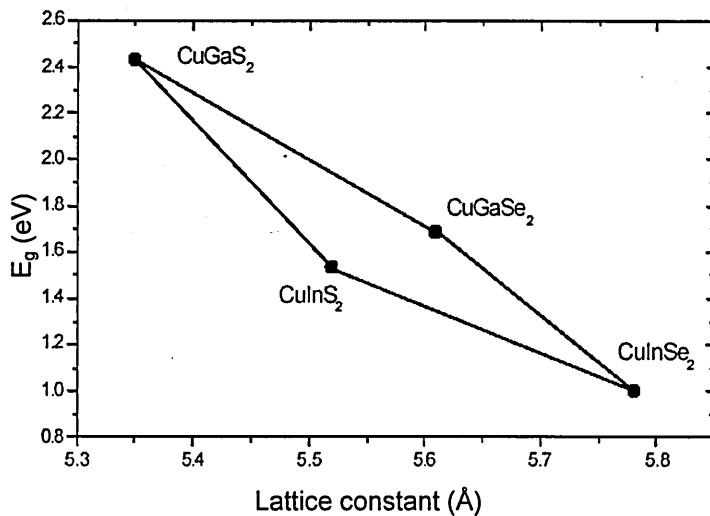


**Figure 2.1.** Bandgap and lattice constants of relevant ternary compounds [25]

CIS has the highest absorption coefficient ( $\alpha > 10^5 \text{ cm}^{-1}$ ) [11] of all known thin film materials, with 99% of all incoming photons being absorbed within the first micrometer of the material [13].

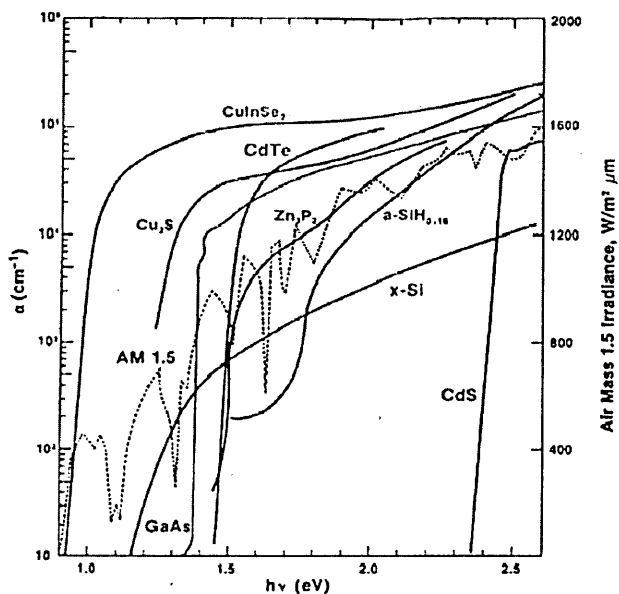


**Figure 2.2.** Absorption coefficients of photovoltaic solar energy materials [25].

### 2.1.3 Crystallography of $\text{CuInSe}_2$

$\text{CuInSe}_2$  belongs to the semiconducting I-III-VI<sub>2</sub> materials family that crystallise in the tetragonal chalcopyrite structure. The primitive cell of this structure is made up of eight tetrahedrons with shared vertices, so the whole cell is just two stacked cubes. Each selenium atom serves as the centre for two Cu and In atoms (see figure 2.3).

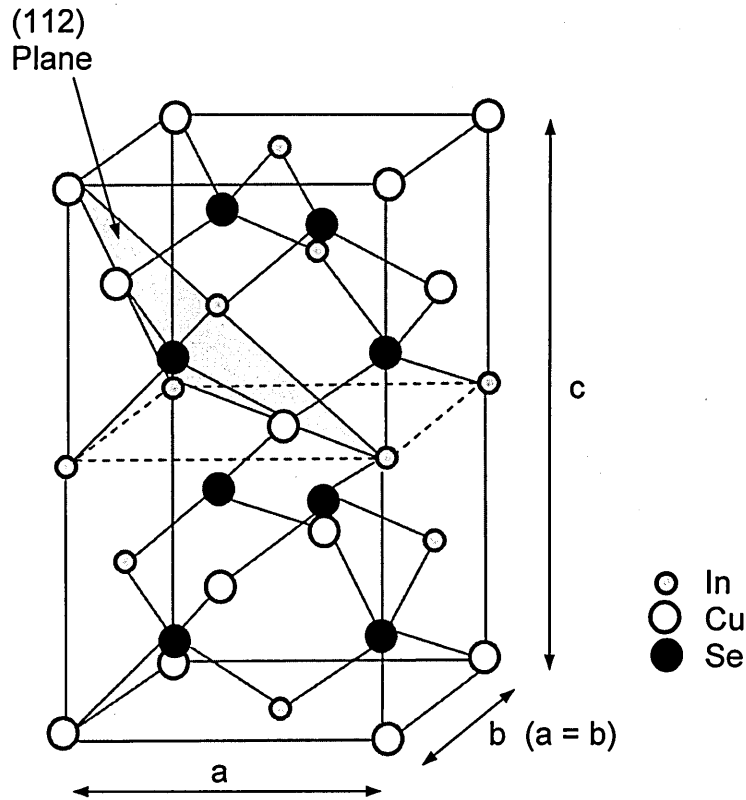


**Figure 2.3.** Primitive cell structure of  $\text{CuInSe}_2$  material [25].

For perfect tetragonal symmetry  $c/a = 2$

For  $\text{CuInSe}_2$  the lattice parameters are;  $a = 0.5784 \text{ nm}$

$c = 1.1620 \text{ nm}$

Whatever preparation technique is used,  $\text{CuInSe}_2$  shows a general growth along the (112) plane.

**Table 2.2.** Selected properties of CuInSe<sub>2</sub>.

Property	Value	Unit	Reference
Structure	Chalcopyrite		[26]
Molecular Weight	336.29	g mol <sup>-1</sup>	[26]
Density	5.77	g cm <sup>-3</sup>	[26]
Colour	Grey		
Melting point	968	°C	[20]
Lattice constant - a	5.78	Å	[20]
- c	11.62	Å	[20]
Thermal expansion coefficient at 273 K			
a axis	8.32	10 <sup>-6</sup> K <sup>-1</sup>	[20]
c axis	7.89	10 <sup>-6</sup> K <sup>-1</sup>	[20]
Thermal conductivity at 273 K	86	mW cm <sup>-1</sup> K <sup>-1</sup>	[20]
Dielectric constant - low frequency	3.6 ± 2.4		[20]
- high frequency	8.1 ± 1.4		[20]
Electron effective mass	0.09	m <sub>e</sub> /m	[27]
Hole effective mass - (heavy)	0.71	m <sub>hh</sub> /m	[20]
- (light)	0.092	m <sub>lh</sub> /m	[20]
Energy gap	1.04	eV	[20]
Electron affinity	4.6	eV	[28]
Absorption coefficient	10 <sup>5</sup>	cm <sup>-1</sup>	[11]

## 2.2 Deposition Techniques

CuInGaSe<sub>2</sub> (CIGS) and CuInSe<sub>2</sub> (CIS) have been grown by a variety of techniques. The next section gives a brief description of some of the most common techniques.

### 2.2.1 Physical Vapour Deposition (PVD)

PVD is the term that covers evaporation and sputtering deposition techniques [29]. It is a vacuum process and very versatile, enabling the deposition of virtually any type of inorganic component and is the most widely used technique for the fabrication of high efficiency CIGS solar cells. In the evaporation process elemental Cu, In, Ga and Se are evaporated onto the substrate by direct electrical heating. In the sputtering process positive gas ions (usually argon ions), produced in a glow discharge, bombard the target material (which is the cathode), this emits material from the target which are then deposited onto the substrate, producing a thin film.

PVD has many advantages; i) it is very versatile, ii) deposits are of high purity, iii) excellent adhesion to the substrate and iv) excellent surface finish. Its main disadvantage is that it is a complex processing technique, requiring very accurate control of all the sources and hence is a very expensive technique.

To date the highest efficiency CIGS solar cells, commercial and lab scale have been produced by PVD. Kushiya et al have produced 13.4% efficient large CIGS modules (30 cm×30 cm), with the Cu-Ga alloy/In precursor layers being deposited by sputtering techniques. This layer was then selenised using H<sub>2</sub>Se gas, then a CIGSS surface layer was produced by sulphidation of the CIGS absorber layer [15,30].

Figure 2.4 shows the three commonly used co-evaporation processes, they all involve the simultaneous evaporation of Cu, In and Ga in the presence of excess Se [31]. They are classified by the Cu evaporation profiles: i) continuous rate, ii) bi-layer process and iii) 3-stage process. The bi-layer process produces larger grains than the continuous rate process, but the 3-stage process developed by Contreras et al (NREL) has produced the highest efficiency lab scale devices, with an efficiency of 19.9% [14,32,33].

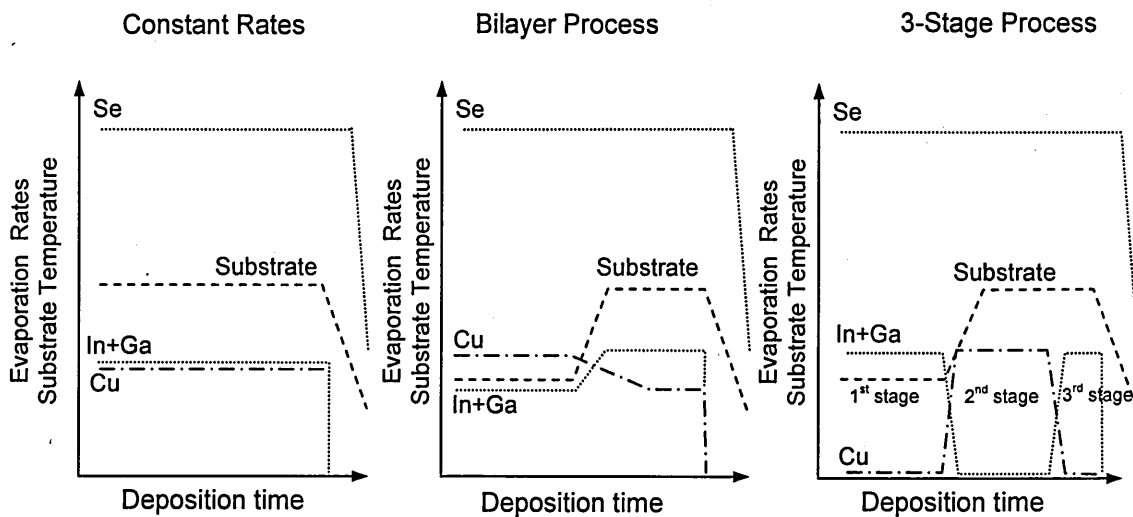


**Figure 2.4.** Schematic diagram of different co-evaporation methods on Mo substrates.

### 2.2.2 Chemical Vapour Deposition (CVD)

CVD is the generic name of a group of processes that involve depositing a solid material from a gaseous phase [29]. Precursor gases are delivered into the reaction chamber at approximately ambient temperatures. As they pass over or come in contact with a heated substrate, they react and decompose forming a solid phase which are deposited onto the substrate.

High quality CIS, CGS and CIGS have been deposited by Hollingsworth et al [34], using a horizontal hot wall spray CVD reactor. Artaud et al [35] have deposited CIS thin films using metalorganic chemical vapour deposition (MOCVD). Metalorganic precursors are used for copper and indium, which react with hydrogen selenide forming a  $\text{CuInSe}_2$  film.

### 2.2.3 Molecular Beam Epitaxy (MBE)

MBE is a high vacuum technique for epitaxial growth, via the interactions of one of several molecular or atomic beams on the surface of a heated substrate [29]. Although high quality CIGS have been produced by MBE [36], this technique is not suitable for depositing large areas, as it is a very expensive and slow process.

## 2.2.4 Chemical Bath Deposition (CBD)

The technique of CBD involves the controlled precipitation from a compound solution onto a suitable substrate. The technique has advantages over some of the other deposition methods as it is simple, relatively low capital expenditure and it is possible to deposit over large areas. However it also has disadvantages, the major one is that it is a very inefficient process, as the material also deposits on the reactor walls. CBD is a batch process which isn't suited for in-line production and there is the problem of disposing/re-cycling the chemicals after each deposition.

The thickness of the deposited layers can be readily controlled by varying the deposition time. Pillia et al deposited CIS layers on FTO/CdS substrates using a mixture of copper citrate, indium citrate and sodium selenosulphite, giving a cell efficiency of 3.1% [37].

## 2.2.5 Spray Pyrolysis

Spray pyrolysis has a number of advantages for thin film deposition; low cost, non vacuum, no high temperature required, fast reproducibility on virtually any substrate and can be scaled up for industrial applications. Krunk et al have grown CIS by this technique, the thin films were prepared by spraying an aqueous solution of ( $\text{CuCl}_2 + \text{InCl}_3 + 3\text{SC}(\text{NH}_2)_2$ ) with the concentrations of 1 mM  $\text{Cu}^{2+}$  [38]. The solution was then sprayed onto a heated substrate in air. The sprayed droplets undergo pyrolytic decomposition and subsequent reactions at the surface of the substrate to form a crystalline thin film [39]. Although this technique is a well investigated technique, only a few results on cell performance have been reported, giving an efficiency of 5% for small area devices [40].

## 1.5.6 Flash Evaporation

Flash evaporation is a well known technique for the evaporation of compounds, it entails the transport of the pulverised compound via a feeder to a super heated evaporation boat to produce complete evaporation of all the elements [41]. The composition of the CIGS thin films can be varied by changing the substrate temperature and deposition rate. Ahmed et al have shown that films grown at higher substrate temperatures improve the film structure and crystallinity [42].

### **2.2.7 Pulsed Laser Deposition (PLD)**

The PLD method of thin film growth involves the evaporation of a solid target in an ultra high vacuum chamber, by using short and high energy laser pulses. The interaction of the laser beam with the target produces a plume of material which is deposited onto a heated substrate. Kuranouchi and Yoshida have produced CIS thin films using polycrystalline CIS powder as the target [43].

### **2.2.8 Electrodeposition (ED)**

Electrodeposition has a number of advantages for thin film deposition [29]; low cost, non vacuum, no high temperature required and it is a proven technology; BP produced 0.81 m<sup>2</sup>, 10.7% CdTe modules [4]. Most ED is carried out using a 3 electrode system, which consists of a bath containing the Cu, In, Ga and Se ions, an anode usually graphite or platinum, a reference electrode and a cathode, which is the substrate onto which the CIGS layer will be deposited, this is normally glass/Mo or glass/FTO depending on cell configuration. The layer then needs to be annealed in carefully controlled environment.

One of the most attractive features of this technique is the simultaneous control of electrical conduction type and the bandgap simply by varying the deposition voltage [23]. These features are crucial for a drastic reduction in the cost of solar cells, in addition these capabilities make it possible to produce the multi-layer graded bandgap device structures as outlined in chapter 5.

Lincot et al have produced 7% efficient 30×30 cm<sup>2</sup> cells [44] and Bhattacharya et al have produced lab scale devices with an efficiency of 15.4% [45]. Electrodeposition is discussed in detail in the next chapter of this thesis.

The main drawback of electrodeposition is that the substrate needs to be conductive. If the sheet resistance of the substrate is high; there is a large voltage drop down the length of the electrode, causing a non-uniform deposition. Another problem is possible contaminates in the electrolyte, this can be remedied in two steps. The first step is to use only high purity chemicals, 5 or 6N. The second step is to self-purify the electrode, this process removes any unwanted background impurities.

---

Self-purification is achieved by applying a slightly lower voltage than the one required for the desired deposition, this voltage is applied for several hours. The 'dirty' electrode is then discarded, then subsequent depositions enable the growth of high purity semiconductors.[23].

## 2.3 CuInGaSe<sub>2</sub> (CIGS) solar cell's current development

### 2.3.1 Introduction

CIGS cells are grown on rigid glass or flexible substrates, with the CIGS absorber layer being of p-type electrical conduction and a second wide bandgap n-type window material is also grown to form a p-n heterojunction, although there is some debate on whether the junction is actually a homojunction buried within the CIGS layer and the window is just a passivating layer [23]. The device is completed with transparent conducting oxide layers and specific metal layers to make the front and back contacts. Further treatment may then be required depending on fabrication method, addition of Na improves device efficiency [46,47] and post deposition heat treatment is necessary for non-vacuum deposition methods.

There are two main device structures; substrate configuration shown in figure 2.5 and superstrate configuration shown in figure 2.6, the former been the most investigated and yielding the highest efficiencies (Table 2.3).

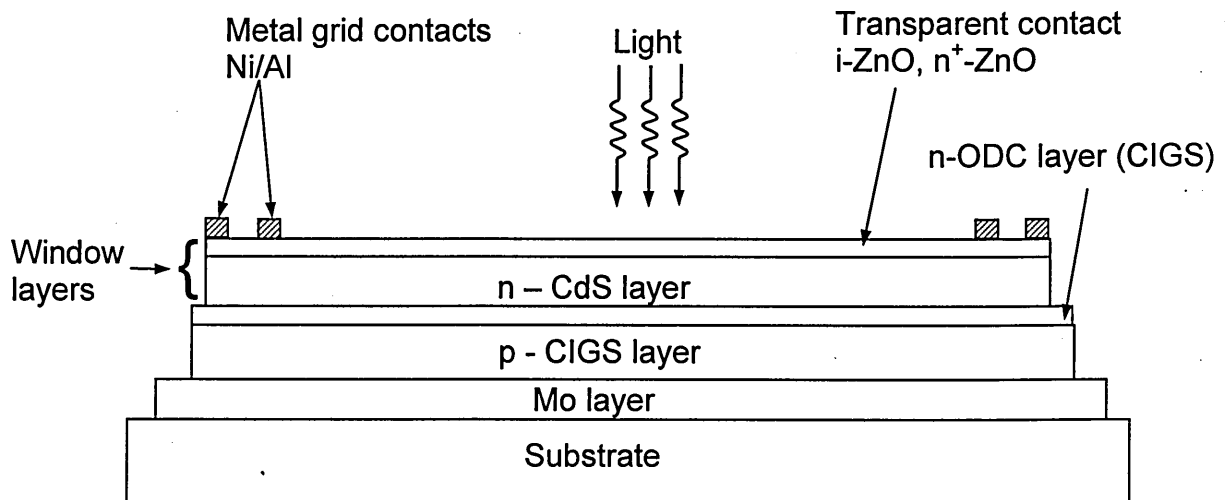


**Figure 2.5.** Layer structure of substrate CIGS thin film solar cell.

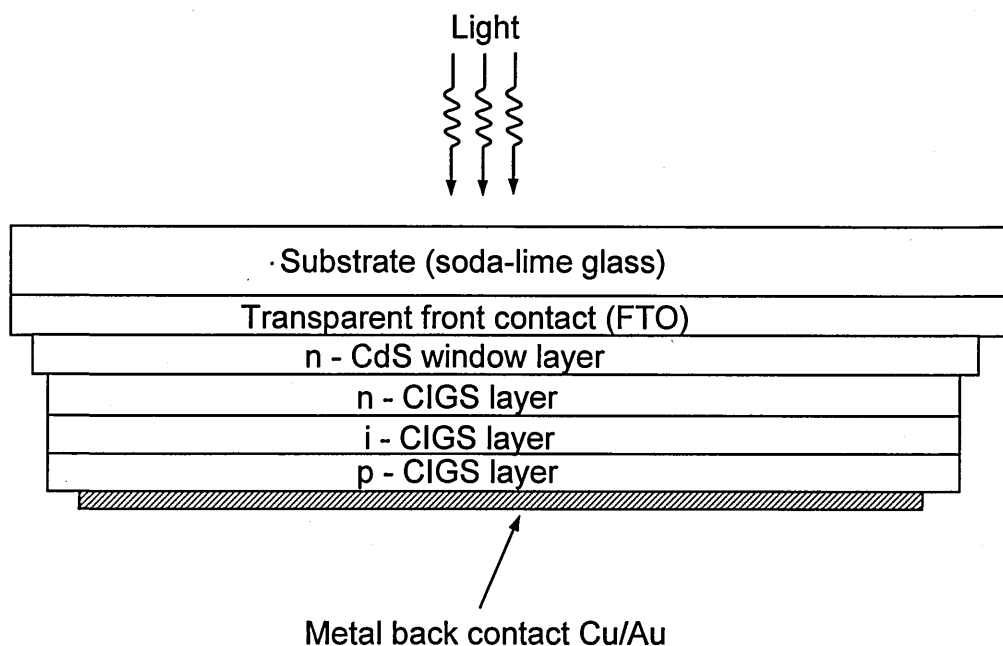


**Figure 2.6.** Superstrate configuration with an nip device structure of CIGS layers.

**Table 2.3.** Efficiencies of CIGS solar cell modules.

Organisation	Device	Size (cm <sup>2</sup> )	Efficiency (%)
Würth Solar	CdS/CIGS	5932	12.5
Shell Solar GmbH	CdS/CIGS	5400	13.1
Global Solar	CdS/CIGS(Stainless steel foil)	7714	7.3
Shell Solar	CdS/CIGSS	3623	12.8
Showa Shell	Zn(O,S,OH) <sub>x</sub> /CIGSS/CIGSS	3454	13.4
NREL	CdS/CIGS (Best lab scale device)	0.419	19.9

Substrate CIGS solar cells give the highest efficiency with 19.9% for lab scale devices [14] and 13.4% for large area modules [15], this is mainly due to favourable process conditions and material compatibility. Generally CdS is used as the window material, due to having very similar lattice constants and its ease of deposition by the CBD method.

Superstrate cells have two major advantages over substrate cells; (i) they don't need a top encapsulation glass layer to protect the cells surface, thereby reducing production steps and hence total cost and (ii) there is no need for a top metal grid contact, which

reduces the efficiency of the device by shading. Early attempts to produce superstrate cells [48], did not yield efficiencies above 5%. The main reason for this low efficiency was the deterioration of the CdS layer and diffusion of Cd into the CIS, at the high temperatures needed for the deposition of CIS.

To overcome this problem more stable buffers were investigated and low temperature deposition methods, notably electrodeposition, but there are still problems as electrodeposited layers need heat treating to 550°C and there are issues with depositing CuInSe<sub>2</sub> directly onto CdS, (this is explained in chapter 7 of this thesis). The highest efficiency superstrate CIGS have been produced by Nakada et al [49], who replaced CdS with undoped ZnO and coevaporated Na<sub>x</sub>Se during the CIGS deposition, to give an efficiency of 12.8%.

### 2.3.2 Effects of sodium

Sodium is known to be a detrimental impurity in semiconductor technology, but Na has a positive influence on the properties of CIGS films [11]. This may be one of the reasons why conventional substrate cells show the highest efficiencies. The substrate, normally soda lime glass (SLG) contains significant amounts of Na (~16 wt%) in the form of Na<sub>2</sub>O. At high temperatures Na diffuses through the Mo into the CIGS layer [45]. In superstrate cells, it is necessary to add the Na as the transparent front contacts inhibit diffusion of Na from the SLG [50]. Rudman et al found very favourable results by adding a 30 nm layer of NaF onto the CIGS layer [51].

The mechanism of why Na improves CIGS performance is still not clear. Although Na has been suspected of doping CIGS, no studies have found any evidence of this, but since Na is a group 1 element it will behave in the same way as Cu in the CI(G)S system, and act as a p-type dopant. Most of the literature suggests Na passivates grain defects and enhances carrier concentration. Rudman et al reported that Na chemically passivates grain boundaries and surfaces by passivating dangling bonds [51]. Its main effect is an increased  $V_{oc}$ , with some groups finding a 50% increase in efficiency after the addition of Na.

### 2.3.3 Effects of sulphur

Adding sulphur to CI(G)S thin films, has been carried out by many groups, and is normally a post deposition treatment, where the sulphidation of CI(G)S is carried out using a H<sub>2</sub>S mixture at high temperatures [52,53]. Sulphidation dramatically increase V<sub>oc</sub> and FF, some groups found a slight reduction in J<sub>sc</sub> [54], but the overall result is an increase in efficiency. Nakada et al reported an increase of cell efficiency from 8-11% before sulphidation to 14.3% after [50] and Showa Shell produce 13.4% efficient modules by using a post deposition sulphidation step [53]. Ohashi et al have tried to eliminate the toxic H<sub>2</sub>S route, by evaporating In<sub>2</sub>S<sub>3</sub> layer after the CIGS deposition and annealing in elemental sulphur vapour, both methods yielded higher efficiencies with the latter showing the greatest improvements, with all parameters increasing [54].

The main reason why sulphur increases cell performance, is that S replaces Se in the CIS lattice, thereby increasing the bandgap of the material, (bandgap of CuInSe<sub>2</sub> = 1.04 eV, CuInS<sub>2</sub> = 1.55 eV) [55] which results an increase in V<sub>oc</sub>. With sulphur being easier to process and more environmentally friendly, some groups have omitted selenium completely. Sulfurcell in Germany produce 0.82 m<sup>2</sup> modules manufactured by evaporation of Cu and In with a H<sub>2</sub>S sulphidation stage, giving an efficiency of 7.4% [56].

Another mechanism for sulphur to improve device parameters is similar to that of Na, by the passivation of surface and grain boundaries of the CIGS layer through the formation of a thin layer of CIGSS [57].

The production of CuInS<sub>2</sub> by one step electrodeposition has proved difficult, with the preferred route been the sulphidation of alloyed or stacked Cu/In electrodeposited layers [58].

### 2.3.4 Effects of gallium

One of the special qualities of CIGS is that its bandgap can be varied. By increasing the Ga/(Ga+In) ratio from 0 to 1, the bandgap increases from 1.04 eV (CIS) to 1.68 eV (CGS). Also with the addition of other elements sulphur and aluminium the bandgap can be effectively varied from 1.04 (CuInSe<sub>2</sub>) to 2.67 eV (CuAlS<sub>2</sub>). As with the addition of sulphur, this increases the built in potential of the device which leads to higher  $V_{oc}$  values [59]. In this way graded bandgap solar cells can be made, which provide a much better match to the solar spectrum and hence improve efficiency by increasing  $V_{oc}$  and  $J_{sc}$ .

Gallium also changes the structural properties of CuInSe<sub>2</sub>, as Ga replaces In in the lattice, because Ga atoms are smaller than In, the lattice parameters  $a$  and  $c$  will also decrease. For CuInSe<sub>2</sub>  $a = 0.578$  nm,  $c = 1.160$  nm and for CuGaSe<sub>2</sub>  $a = 0.562$  nm and  $c = 1.100$  nm. This structural change can be seen by a shift to higher angles in the x-ray diffraction peaks, see chapter 7 of this thesis. There seems to be some disagreement as to how much the Ga/In ratio needs to be to improve device efficiency. Some groups have reported that when the Ga ratio is greater than 0.3, the lattice mismatch between CuInSe<sub>2</sub> and Cu(In<sub>1-x</sub>Ga<sub>x</sub>)Se<sub>2</sub> results in an increase in intrinsic defects, which result in a decrease in efficiency [60,61]. However Miyazaki et al found that cells with Ga content of  $x = 0.6$  yielded higher conversion efficiencies, with improvements in all three parameters,  $V_{oc}$ ,  $J_{sc}$  and FF [62].

To date the highest efficiency CIGS solar cells, both lab scale and commercial all utilise bandgap grading, by increasing the Ga/(Ga+In) concentration during the deposition process, which has resulted in 19.9% efficient lab scale devices [14] and 13.4% efficient commercial modules [15]. Figure 2.7 shows elemental concentration as a function of depth for NREL's 19.5% cells and shows that the Ga/(Ga+In) is 0.5 at the back of the CIGS layer [32].

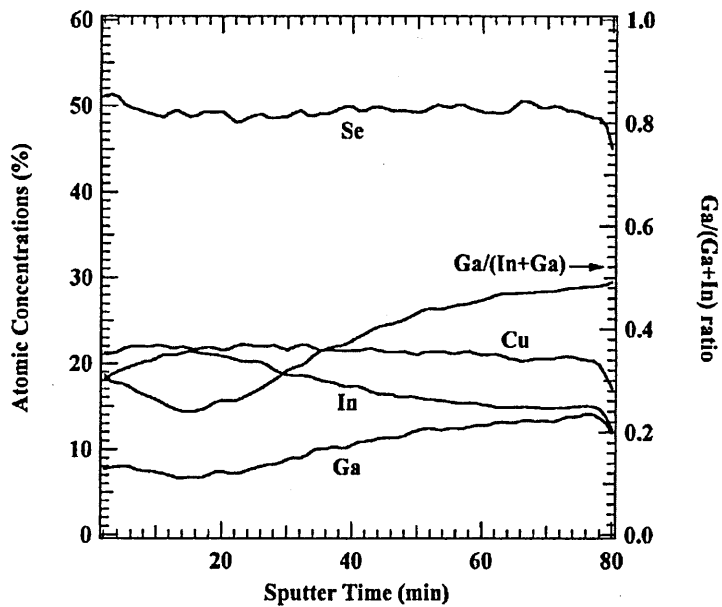


**Figure 2.7.** Elemental concentrations as a function of depth into the CIGS absorber. The right hand axis shows the calculated  $\text{Ga}/(\text{In}+\text{Ga})$  ratio [32].

### 2.3.5 ODC layer (Ordered Defect Compound)

The ODC layer is a Cu deficient surface layer extending  $\sim 10\text{-}15$  nm from the surface of the CIGS. This layer is naturally n-type and exists prior to the deposition of CdS, when CdS is deposited, Cd diffuses into the Cu vacancies, making the layer more n-type [63], (this is explained later in this chapter). It has been proposed that this is where the junction is formed to the p-type CIGS, and this is what causes the large band bending, enabling the device to work [63,64]. Through simulations it has been shown that the doping concentrations in this area are sufficient for n-type conduction [65].

It has also been proposed that the ODC layer is responsible for Fermi level pinning in CIGS layers. Ideally the Fermi level will be pinned closest to the conduction band [66], and this will produce the highest potential barriers. For these reasons it might be another factor why substrate cells out-perform superstrate cells, as the naturally occurring ODC layer is used to benefit the device performance.

## 2.4 Buffer layer

### 2.4.1 Cadmium Sulphide (CdS) buffer layer

CdS has a relatively high bandgap (2.42 eV) and is a chemically stable n-type semiconductor, which is the reason why it is used for the window material in CIGS solar cells. Using this material the highest efficiencies have been achieved, but there are several concerns about this material.

1. With its bandgap of 2.42 eV a considerable amount of light is absorbed in the CdS layer, which reduces the quantum efficiency in the blue part of the spectrum. To minimise this loss the layers need to be made as thin as possible [67,68], Contreras et al [69] found the optimum thickness for the CdS layer is 60-80 nm, for the highest efficiency CIGS solar cells. If the layer is too thick there are losses in transmission, if the layer is too thin or the layer is not there at all, there are losses due to recombination.

2. At present the CdS layer is generally deposited by CBD, which typically consists of dissolved  $\text{Cd}^{2+}$  ions, thiourea and ammonia, but this is a wet process and is not suited for in-line vacuum deposition techniques, however the method is well suited to the electrodeposition technique.

To eliminate the CBD process many groups have deposited CdS by PVD [70], but this method never yields as high efficiencies. In general CBD CdS buffer layers yield efficiencies about 3-4% higher than PVD, as shown by figure 2.8 [70].

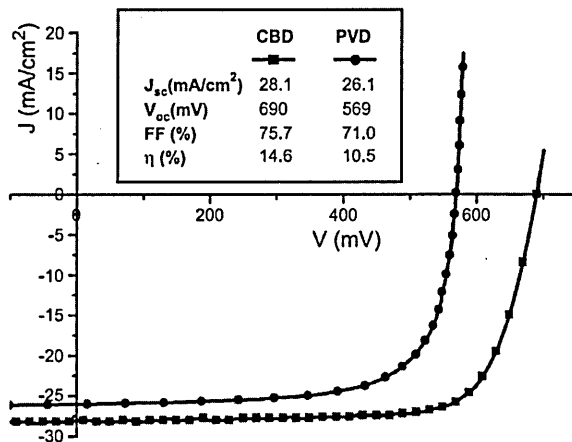


Figure 2.8. I-V curves comparing CIGS cells with CBD and PVD CdS buffer layers.

Three main reasons have been advanced for why CBD out performs PVD:

(i) CBD CdS modifies the surface of the CIGS by forming an n-CdSe or an n-type CIGS layer, as the Cd diffuses into Cu vacancies at the CdS/CIGS interface region to a depth of  $\sim 10$  nm [71] thus forming a buried hetero-junction. This happens because CBD CdS is not a stable compound. It consists of Cd-OH and Cd-O, where the Cd is not strongly bonded and because a CIGS layer is known to be Cu deficient extending to  $\sim 10$  nm from the surface, which is known as the ODC layer, it is easier for the Cd to be substituted into Cu vacancies. This does not occur with PVD CdS, and the absence of the hetero-junction may lead to lower efficiencies.

(ii) Nakada found that CBD CdS grows epitaxially on the CIGS surface. The lattice spacing of  $3.3 \text{ \AA}$  agrees well with the lattice spacing of the (112) planes of CIGS and it was clear that no lattice defects were present. This epitaxial growth may be due to the unique growth mechanism of the CBD process, i.e. cleaning of the CIGS surface by ammonia [71].

(iii) CBD CdS deposited on CIGS can form both hexagonal and cubic crystal structures, but hexagonal is the exception. Nadenau et al [72] found this to be dependant on the substrate temperature. Cubic CBD CdS has a good lattice match to tetragonal CIGS [70] in contrast to hexagonal PVD CdS which has a large lattice mismatch.

3. This brings us onto the current debate on whether the photo-active junction is really formed at the p-CIGS/n-CdS interface [73]. With the CdS layer being usually in the order of a few tens of nm's, it is considered that this is not thick enough to establish a proper n-type semiconductor layer in order to form a p-n type hetero-junction, and therefore some researchers consider that it is only a passivation layer [74], with the possibility of the junction being a homo-junction and buried within the CIGS layer.

There does seem to be some contradiction in the literature, Cavana et al reported "we can note that the CdS layer even if its thickness is very thin is absolutely necessary to reach the highest efficiencies" [73]. Where as Ramanathan et al conclude that "greater improvements in current collection can be achieved by using a thinner CdS window layer or by eliminating the window layer" [32].

4. Another concern with CdS is that the maximum annealing temperature is 450°C, which is only a problem if the device is made in superstrate configuration and by low temperature deposition method. The CIGS is deposited on the CdS and the CIGS needs to be annealed at 550°C for re-crystallisation, this temperature causes the CdS layer to deteriorate or even evaporate. To address this problem Nakada et al [75] have successfully manufactured 11.2% superstrate CIGS solar cells using ZnO as the buffer layer.

#### 2.4.2 Alternative buffer layers

For the 4 reasons outlined above there is much research into finding alternative buffer layers. Hariskos et al have written a comprehensive review paper covering all the alternative buffer layers and deposition methods for modules and lab scale devices and the results are presented in Table 2.4 and Table 2.5 respectively [76]. The most noteworthy is Showa Shells 13.4% efficient 3659 cm<sup>2</sup> module using CBD Zn(O,S,OH)<sub>2</sub> as the buffer layer.

**Table 2.4.** Summary of the best CIGS-based solar module efficiencies fabricated with different Cd-free buffer layer materials.

Buffer Layer	Module area (cm <sup>2</sup> )	η (%)	Institute/company	Ref.
CBD Cds	6500	13.0	Wurth Solar	[77]
CBD ZnS	900	14.3	Showa Shell	[78]
	3659	13.4	Showa Shell	[78]
CBD In <sub>2</sub> S <sub>3</sub>	717	9.7	ZSW	[79]
ALD In <sub>2</sub> S <sub>3</sub>	13	13.4	ZSW	[80]
	714	12.9	ZSW	[81]
CBD ZnSe	20	11.7	HMI/Siemens	[82]
ILGAR ZnO	20	10.9	HMI/Shell Solar	[83]

**Table 2.5.** Summary of the best CIGS-based solar cell efficiencies ( $A \leq 1 \text{ cm}^2$ ), fabricated with Cd-free buffer layers and deposited by different techniques.

Material	Method	$\eta$ (%)	Institute	Ref.
CdS	CBD	19.5	NREL	[32]
ZnS-based	CBD	18.6	NREL/AGU	[84]
	ALD	16.0	ÅSC	[85]
	PE/ILGAR	14.2	HMI/Siemens	[86]
	Evaporation	9.1	ETHZ	[87]
	CBD	14.0	TIT	[88]
In(OH) <sub>3</sub> -based	CBD	15.7	IPE/ ÅSC	[89]
	ALD	16.4	ENSCP/ZSW	[90]
	Evaporation	14.8	IPE	[91]
	Sputtering	12.2	ZSW/HMI/WS	[92]
ZnSe-based	CBD	15.7	HMI/Siemens	[93]
		14.4	HMI/Shell Solar	[94]
	MOVPE	12.6	DESR/Siemens	[95]
		11.6	DESR/IAP/Siemens	[96]
	ALD	11.6	TIT	[97]
	Co-	9.1	TIT	[97]
	Evaporation	9.0	ETHZ	[87]
ZnInSe <sub>x</sub>	Co-	15.3	TIT	[98]
In <sub>x</sub> Se <sub>y</sub>	Co-	13.0	TIT	[99]
ZnMgO	Sputtering	16.2	Matsushita Elec.	[100]
ZnO	CBD	14.3	TIT	[101]
	Sputtering	15.0	NREL	[102]
	PE/Sputt.	14.2	NREL	[103]
	ALD	13.9	TIT	[104]
		14.6		[105]
	MOCVD	13.4	WSU	[106]
	PE/ILGAR	15.0	HMI/Shell Solar	[78]
	ED	11.4	WIS/ENSCP/IPE	[107]
SnO <sub>2</sub>	CBD	12.2	IPE	[108]

It can be noted from Table 2.5 that generally whatever buffer material is used, the CBD process yields higher efficiencies than evaporation methods.

## Chapter 3: Electrodeposition

### 3.1 Introduction

Electrodeposition of metals can be traced back to around 1800 when Luigi Brugnatelli, electrodeposited gold [109]. Today electrodeposition of large area metallic protective coatings is a major industry. Zinc coating for example, being a roll-to-roll process with several metres per minute deposition rates. It is only in the past few decades when the application of this technique has been adopted to grow semiconductors, as semiconducting properties are far more difficult to obtain than metallic properties, involving minority carrier control at ppm levels. However electrodeposition is a promising technique, as it is low cost, low power, simple to set up and is easily scaled up to commercial levels, as BP solar did in 2001 producing 0.81 m<sup>2</sup>, 10.7% efficient CdTe solar modules [7].

### 3.2 Theory

A basic electrodeposition bath consists of an electrolyte containing metal ions, an electrode or substrate (cathode) on which to deposit the material and a counter electrode (anode). When a potential is applied between the two electrodes, the positive ions or cations move towards the cathode where they discharge (reduction). The negative ions (anions) move towards the anode where they release electrons (oxidation). For example if the bath contains a Cu salt (e.g. copper sulphate), the Cu<sup>2+</sup> ions will deposit on the cathode resulting in a copper layer.



The simultaneous discharge of one cation at the cathode and one anion at the anode is equivalent to the transport of one electron from the cathode to the anode through the electrolyte. The process is given by Michael Faraday's laws of electrolysis.

Faradays first law: The total amount of chemical change produced by an electric current is proportional to the total charge passing through the electrolyte.

Faradays second law: The masses of the different substances liberated in the electrolysis are proportional to their chemical equivalent weights.

Utilising these two laws an equation to calculate the theoretical thickness of an electrodeposited film can be derived [110].

$$T = \frac{1}{nFA} \left( \frac{itM}{\rho} \right) \quad (3.2)$$

T = Thickness

i = Average current

F = Faradays constant 96500 Cmol<sup>-1</sup>

A = Area

t = Time (s)

M = Molar mass (g/mol)

n = Number of electrons

ρ = Density

From thermodynamics it can be shown that the cell potential E is related to the Gibbs free energy of the reaction. Gibbs free energy is the chemical potential that is minimized when a system reaches equilibrium at constant pressure and temperature.

$$\Delta G = -nFE \quad (3.3)$$

A change in Gibbs free energy is a useful indicator of whether a reaction will proceed spontaneously. The sign of ΔG indicates the direction of the reaction has to shift to reach equilibrium and the magnitude of ΔG shows how far the reaction is from equilibrium. If the electrode potential is positive, the free energy of the reaction will be negative and the reduction reaction will be spontaneous. If the electrode potential is

negative, the free energy of the reaction will be positive, which means a potential more negative than the reaction potential needs to be applied to force the reduction reaction.

Therefore the potential of an electrochemical cell (E) is a measure of how far a reduction-oxidation (redox) reaction is from equilibrium and is described by the Nernst equation [110].

$$E = E_0 - \frac{RT}{nF} \ln \left[ \frac{ap}{ar} \right] \quad (3.4)$$

$E_0$  = Standard reference potential measured against SHE, concentration 1M, pressure 1 atm and temperature 25°C

R = Gas constant

T = Temperature K

n = Number of electrons

F = Faraday's constant

ap = Activity product

ar = Activity reactant

### 3.2.1 Nucleation and growth

The growth of an electrodeposited material from an electrolyte involves a transformation of phase from the ionic species in the solution to a solid phase on the electrode. This transformation in phase is the cumulative effect of ionic transport, discharge, nucleation and subsequent growth of the material.

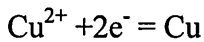
The overall growth of the electrodeposited material is highly influenced by the crystallographic orientation of the substrate. In the case of the work presented in this thesis, the substrate (cathode) was polycrystalline in nature, which has a large number of grains with differing orientations. As a result there are a large number of surface defects, which form nucleation sites, putting their signature on the morphology of the layer being deposited and generally controlling the growth kinetics. Although the nature of the substrate plays a major role in the nucleation and growth process, there are many

other influencing factors: for example, additives in the electrolyte, concentration of metal ions, temperature, pH and applied potential.

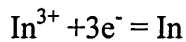
### 3.3 Electrochemical diagrams

#### 3.3.1 Pourbaix diagram

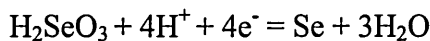
Using the Nernst equation a diagram of pH versus growth potential can be plotted to form a Pourbaix diagram [111] which is a useful tool to predict the formation of different compounds at varying deposition voltages and pH. Below are the Nernst equations for the basic individual reactions for the deposition of copper, indium and selenium.



$$E = E_0 - \frac{RT}{2F} \ln \left[ \frac{\text{Cu}}{\text{Cu}^{2+}} \right] = 0.135 - 0.0295 \log \frac{(\text{Cu})}{(\text{Cu}^{2+})} \quad (3.5)$$



$$E = E_0 - \frac{RT}{3F} \ln \left[ \frac{\text{In}}{\text{In}^{3+}} \right] = -0.545 - 0.0197 \log \frac{(\text{In})}{(\text{In}^{3+})} \quad (3.6)$$



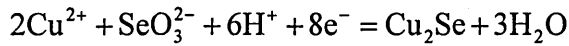
$$E = E_0 - \frac{RT}{4F} \ln \left[ \frac{\text{Se}}{\text{H}_2\text{SeO}_3} \right] = 0.535 - 0.0148 \log \frac{(\text{Se})}{(\text{H}_2\text{SeO}_3)} - 0.0433\text{pH} \quad (3.7)$$

As can be seen from the equations the deposition potential of Se is more positive than Cu, which are both more positive than In. Therefore the order of 'ease' of deposition will be Se, Cu and In. For simultaneous depositions of all three elements, the deposition potentials of all three elements need to come closer together. This can be achieved by

adjusting the pH, adjusting the ion concentration of the electrolyte, adding a complexing agent and by using a supporting electrolyte.

### 3.3.1.1 Reactions used to plot Cu-In-Se system Pourbaix diagram; figure 3.1

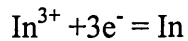
Reactions 3.8 - 3.16 were the selected reactions used for the construction of the Pourbaix diagram for CuInSe<sub>2</sub>, shown in figure 3.1.



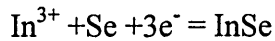
$$E = E_0 - \frac{RT}{nF} \ln \left[ \frac{a_p}{a_r} \right]$$

$$E = 0.697 - \frac{RT}{nF} \ln \left[ \frac{(\text{Cu}_2\text{Se})(3\text{H}_2\text{O})}{(2\text{Cu}^{2+})(\text{SeO}_3^{2-})(6\text{H}^+)} \right]$$

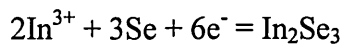
$$E = 0.697 - 0.0074(-2\log(2\text{Cu}^+) - 2\log(\text{SeO}_3^-) + 6\text{pH}) \quad (3.8)$$



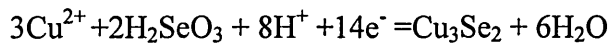
$$E = -0.338 - 0.0197(-3\log(\text{In}^+)) \quad (3.9)$$



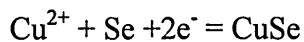
$$E = -0.046 - 0.09591(\log(\text{In}^+)) \quad (3.10)$$



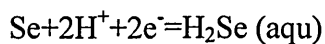
$$E = -0.230 - 0.0099(-3\log(2\text{In}^+)) \quad (3.11)$$



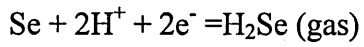
$$E = -0.676 - 0.0042(-2\log(3\text{Cu}^+) + 8\text{pH}) \quad (3.12)$$



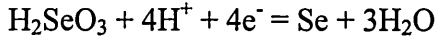
$$E = -0.560 - 0.0296(-2\log(\text{Cu}^+)) \quad (3.13)$$



$$E = -0.399 - 0.0591\text{pH} \quad (3.14)$$



$$E = 0.082 - 0.0591\text{pH} \quad (3.15)$$



$$E = 0.74 - 0.0591\text{pH} \quad (3.16)$$

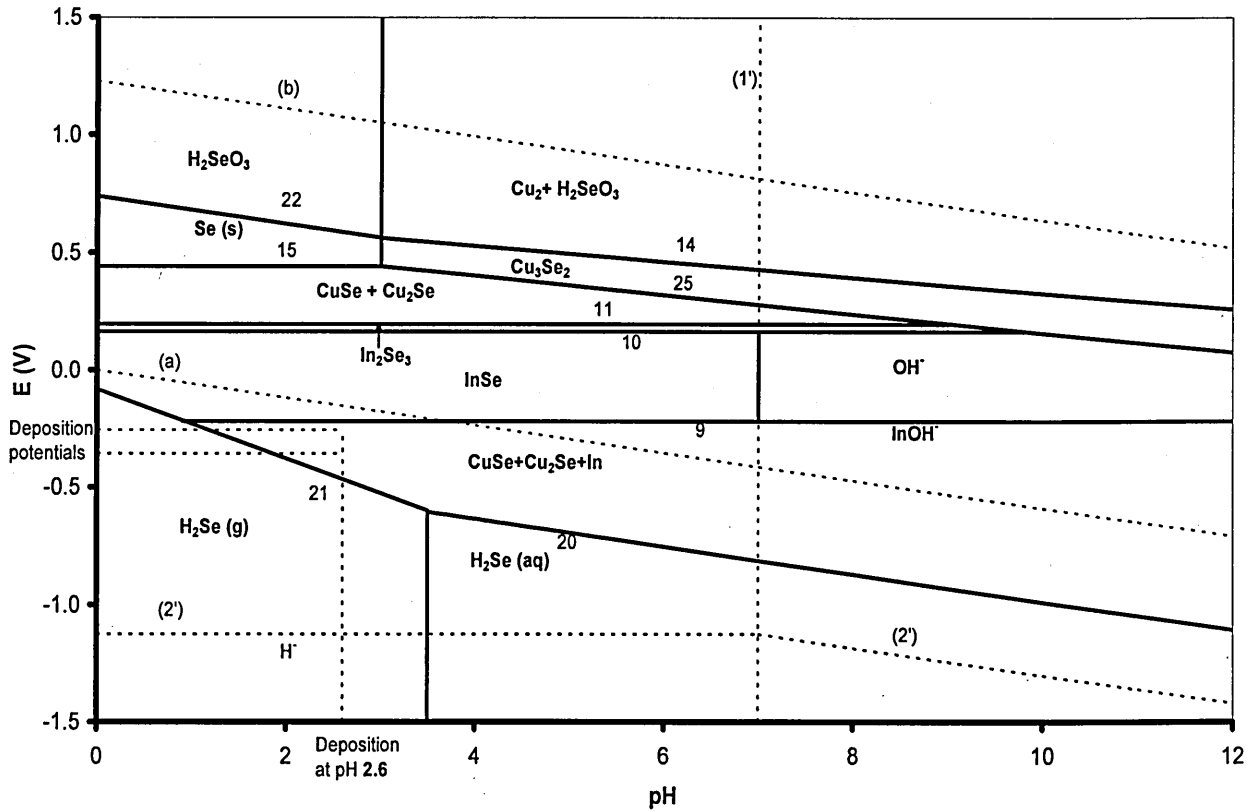
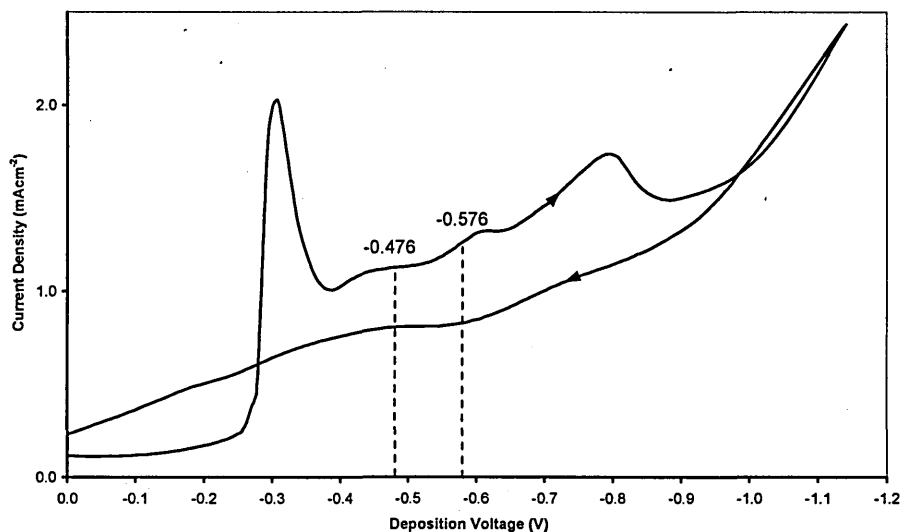


Figure 3.1. Pourbaix diagram for CuInSe<sub>2</sub> system.

### 3.3.2 Cyclic Voltamogram

A cyclic voltamogram is another useful tool for determining the onset of a reaction and indicates where and what materials are being deposited. The potential is measured between the reference electrode and the working electrode and the current is measured between the working electrode and counter electrode. The data is then plotted with current versus potential, see figure 3.2 for a typical CIS voltamogram. The current will rise when the potential reaches the reduction potential of the particular reaction. Especially when read in conjunction with a Pourbaix diagram, it is possible then to work out which compounds form at a particular deposition voltage. Chapter 8 has a detailed explanation of the CIS voltamogram.



**Figure 3.2.** Cyclic voltamogram of  $\text{CuInSe}_2$  deposited at room temperature, using an acidic aqueous bath with concentrations; 2.6 mM  $\text{CuCl}_2$ , 9.6 mM  $\text{InCl}_3$ , 5.5 mM  $\text{H}_2\text{SeO}_3$  and 240 mM  $\text{LiCl}$ . The two potentials marked on the graph indicate where the film was deposited.

A problem of concern is the evolution of hydrogen, which typically occurs at cathodic potentials above 1 V, although hydrogen may form at any potential depending on which individual reaction is taking place. The evolution of hydrogen due to the splitting of water molecules must be avoided, as this will deteriorate the quality of the film being deposited and cause the film to peel away completely. In figure 3.2 this can be seen

where there is a steep rise in current at  $\sim -0.90$  V. As mentioned in chapter 1.3.2.2 if the evolution of hydrogen is not vigorous, it can be advantageous due to hydrogen passivation. The steep rise in current could also be due to the deposition of copper and indium.

### **3.4 Double layer**

Although the Nernst equation gives the theoretical value for the electrode potential, in practice the potential is always greater (i.e. more negative at the cathode and more positive at the anode). This is because a charged surface at the electrode/electrolyte interface needs to be overcome, which according to Stern [110] can be divided into two parts.

1. A compact double layer known as the Helmholtz double layer.
2. A diffuse layer known as the Gouy-Chapman layer.

#### **3.4.1 Helmholtz layer**

The Helmholtz double layer is a dense layer of ions and water dipoles formed at the surface of the electrode. In this region the potential decreases linearly with distance away from the electrode. This layer can be divided further into the inner and outer Helmholtz layers. The inner plane (IHP) is adjacent to the electrode surface and consists of completely orientated water dipoles and contact adsorbed ions. The outer plane (OHP) consists of partially ionised water dipole layers. The whole of the Helmholtz layer is immobile [112].

#### **3.4.2 Gouy-Chapman layer**

In contrast the Gouy-Chapman layer consists of mobile ions which are non-uniformly distributed in the vicinity of the electrode. Their concentration is largest nearest to the electrode surface, decreasing exponentially into the bulk of the electrolyte.

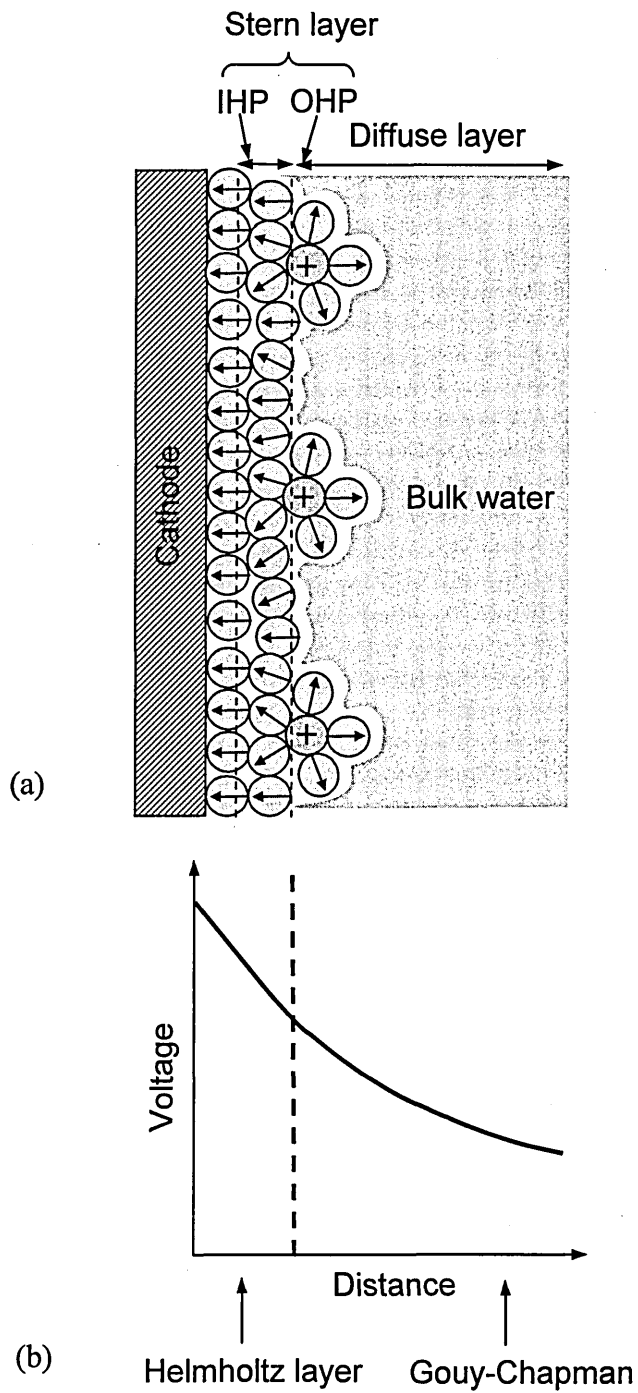


**Figure 3.3.** (a) structure of the double layer, (b) potential distribution across the interface.

### 3.5 Three electrode cell

During the deposition process there are variations in the cathodic potential of the cell due to changes in ionic concentration in the cell, and as the material deposits onto the substrate the conductivity will change. These changes will cause the quality of the deposited layer to deteriorate and at certain potentials it will peel off completely. To overcome these problems a three electrode cell is used (figure 3.4), which consists of a working electrode (the substrate), a counter electrode and a reference electrode. A Ag/AgCl reference electrode was used for all the work presented in this thesis.

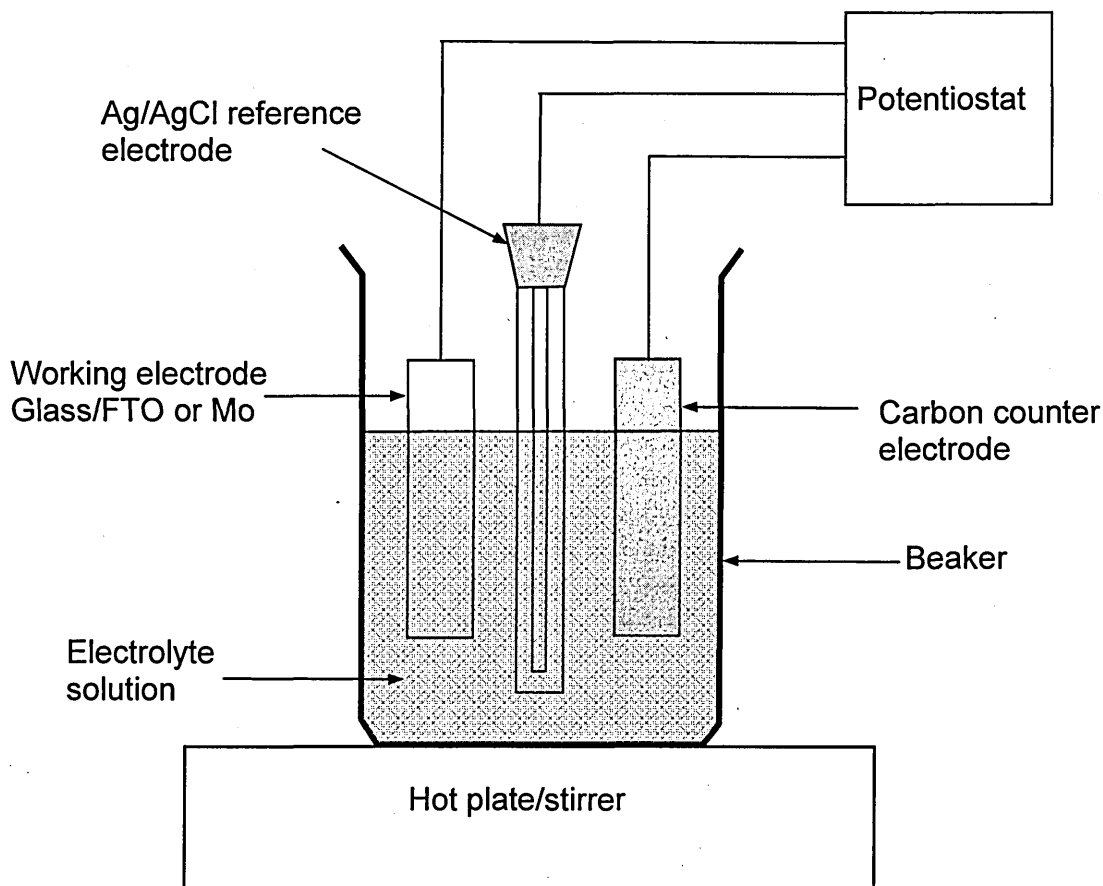


**Figure 3.4.** Schematic diagram of a three electrode cell.

The purpose of the reference electrode is to provide a stable well known potential, on which to reference the redox reaction occurring at the working electrode. In addition the potentiostat uses the voltage output from the reference electrode to stabilise the drop in

current and resistance (IR drop) and polarisation effects on the surface of the working electrode, which would occur if only two electrodes were used. [110]

The three electrode cell is the most common cell used for the electrodeposition of CIGS and the deposition is generally carried out at room temperature, with a pH in the range of 1.5 - 2.5 and without stirring [58,113].

### **3.6 Electrodeposition of CuInSe<sub>2</sub>**

As outlined in chapter 2.2 CIGS layers can be deposited by many techniques, but to achieve low cost CIGS thin film solar cells, the expensive one step co-evaporation technique needs to be replaced with low cost methods, electrodeposition for example. However the problem with this method is that the as-deposited layers do not produce photovoltaic quality films and a post deposition heat treatment step is required.

In the first step a precursor layer is deposited. This can either be elemental layers of copper, indium, selenium etc producing a stacked layer structure, a bi-layer structure, copper/indium, indium/selenide etc or a CIS precursor layer deposited by using a single bath containing all three elements, as devised by Bhattacharya (114). This is the most researched method and in principle most simple. It is known as one step electrodeposition and is the method used in this research.

Whichever of the above precursor methods is adopted, they all require a second step to produce electronic quality materials; this is thermal annealing which requires careful control of temperature, atmosphere and duration. The as-deposited films do show weak XRD patterns with very wide peaks showing poor crystallinity and peak positions can be assigned to many different phases. A vast improvement in sharpness and intensity is observed after annealing. Many groups including the SHU group have found that the films need to be annealed at 550°C under the presence of selenium and flowing H<sub>2</sub>/Ar gas for 30 minutes. [58,113].

## Chapter 4: Characterisation techniques

### 4.1 Material characterisation

#### 4.1.1 Introduction

The semiconducting layers were characterised by the following techniques;

- X-Ray Diffraction (XRD), to study the bulk structure of the layers.
- X-Ray Fluorescence (XRF), to determine elemental composition.
- Scanning Electron Microscopy (SEM), for surface morphology.
- Optical absorption, to determine the bandgap.
- Photoelectro Chemical Cell (PEC), to determine the electrical conductivity type of the layer.

#### 4.1.2 X-ray Diffraction (XRD)

XRD is a technique used to investigate the structure and chemical composition of crystalline materials. It relies on the fact that crystals are composed of regular spaced atoms, which act as scattering centres for X-rays. If the wavelength of the X-ray is comparable to the atomic spacing of the crystal, diffraction will then occur and under certain conditions a large number of scattered rays mutually reinforce each other, resulting in a diffracted beam [115].

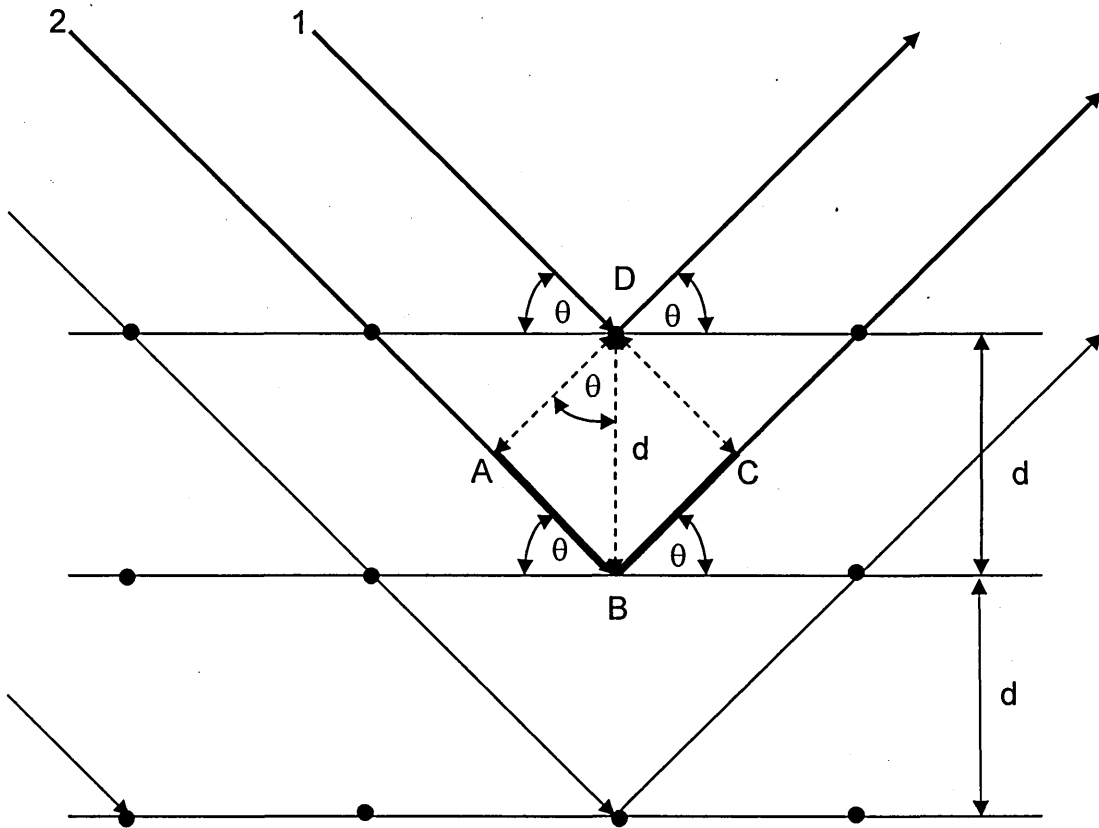


**Figure 4.1.** Schematic diagram of the principle of X-ray diffraction by a crystal lattice.

Atoms scatter incident X-rays in all directions, but at certain conditions some of these scattered beams will be completely in phase giving rise to constructive interference. In figure 4.1, the rays 1 and 2 are scattered by the atoms at D and B and the path difference is ABC.

$$AB = BC = DB \sin \theta$$

For constructive interference, path difference should be equal to integral multiples of the wavelength.

ie.  $2 DB \sin \theta = n\lambda$

Now  $DB = d$

Therefore  $\underline{2d \sin \theta = n\lambda}$  (4.1)

This is Bragg's law and  $\theta =$  the Bragg angle

Therefore for fixed values of  $\lambda$  and 'd' diffraction will occur when the angle of incidence  $\theta_1, \theta_2$  etc corresponds to  $n = 1, 2$  etc. i.e. a whole number of wavelengths.

The rays scattered by all of the atoms in all of the planes are therefore in phase and interfere constructively, to form a strong diffracted beam.

If the scattering atoms were not arranged in a regular periodic manner, the scattered rays would have random phase relationships and constructive interference would not occur. Therefore X-Ray diffraction is a good technique for determining the crystallinity of a structure.

#### **4.1.2.1 Glancing angle X-ray diffraction**

Diffraction only occurs when Bragg's law is satisfied ( $2d \sin \theta = n\lambda$ ), therefore this can be achieved by continuously varying  $\lambda$  or  $\theta$ .

The method used for this thesis was glancing angle X-Ray diffraction. This involves performing a detector scan at fixed low angles of incidence. This limits the penetration of the X-rays thus reducing the contribution of diffracted rays from the substrates, making this a good technique for the analysis of thin films.

The sample is fixed at a small incident angle ( $0.5^\circ$  in this case) and only the X-ray detector is rotated. Due to the small incident angle, X-rays do not penetrate deeply into the sample and diffraction only occurs near the surface from the grains that satisfy Bragg's law.

The data from an XRD measurement are presented as a series of peaks; with the number of X-ray counts plotted against the diffraction angle  $2\theta$ . The position and intensity of the peaks are characteristics of the unit cells of each phase present in the material. By comparing peak positions with standard data files the material can be identified. From analysis of the full width at half maximum (FWHM) of a peak, the grain size, strain and lattice parameters can be calculated.

The grain size is calculated using the Scherrer equation [115];

$$t_{hkl} = 0.89 \frac{\lambda}{\beta(2\theta) \cos \theta} \quad (4.2)$$

Where  $t_{hkl}$  is the grain size in the plane normal to the diffracting plane,  $\lambda$  is the wavelength of X-rays,  $\beta(2\theta)$  is the FWHM of the peak in radians and  $\theta$  is the Bragg angle in radians.

The strain ( $\epsilon$ ) can be calculated by plotting a graph of  $\beta \cos \theta$  versus  $\sin \theta$ , which is derived from the Hull equation [115].

$$\beta \cos \theta = \epsilon \sin \theta + \frac{\lambda}{t} \quad (4.3)$$

The lattice parameters can be calculated from the equation below.

$$\frac{1}{d^2} = \frac{h^2 + k^2}{a^2} + \frac{l^2}{c^2} \quad (4.4)$$

- X - X ray source
- LFF - long fine focus
- SS - soller slits
- DS - divergency slit
- S - substrate
- C - collimator
- M - monochromator
- D - detector

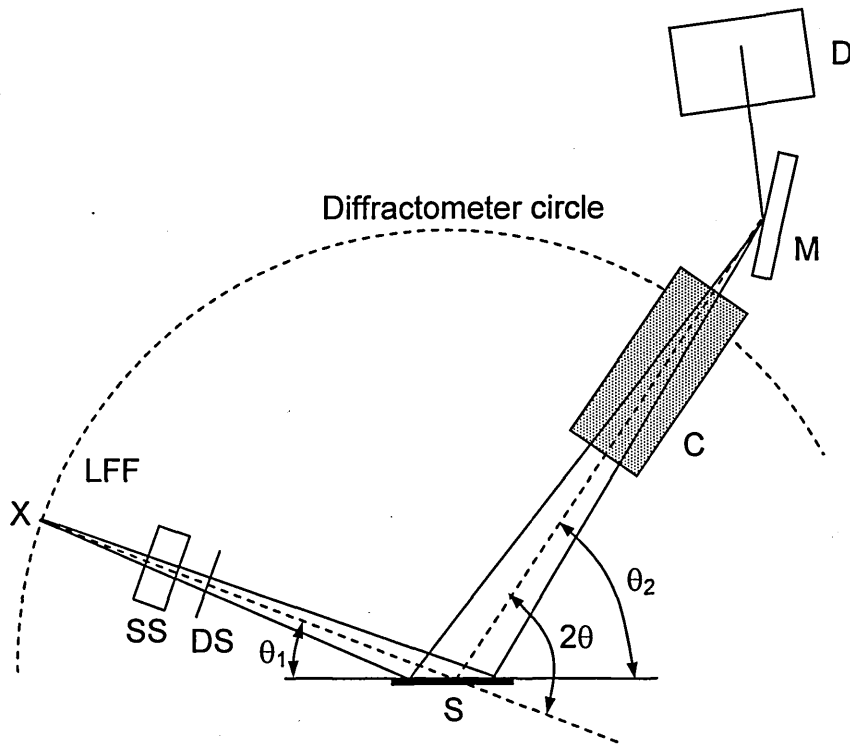
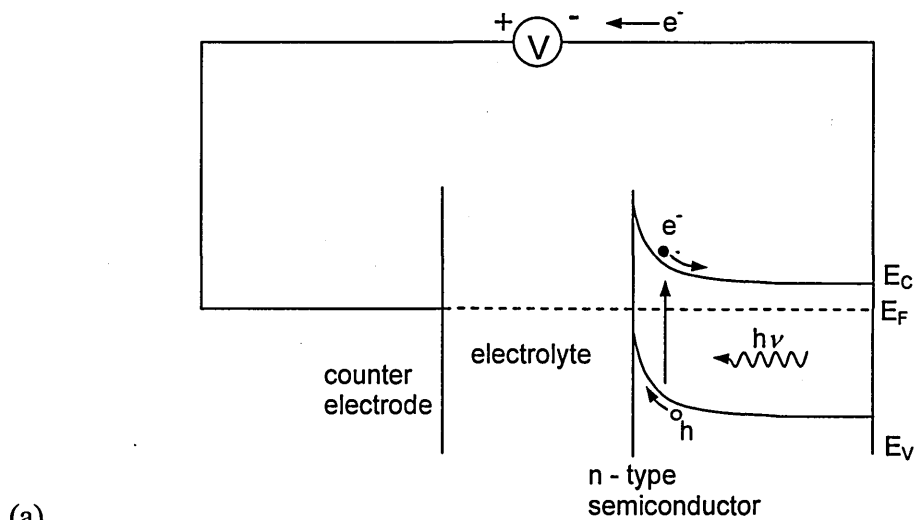


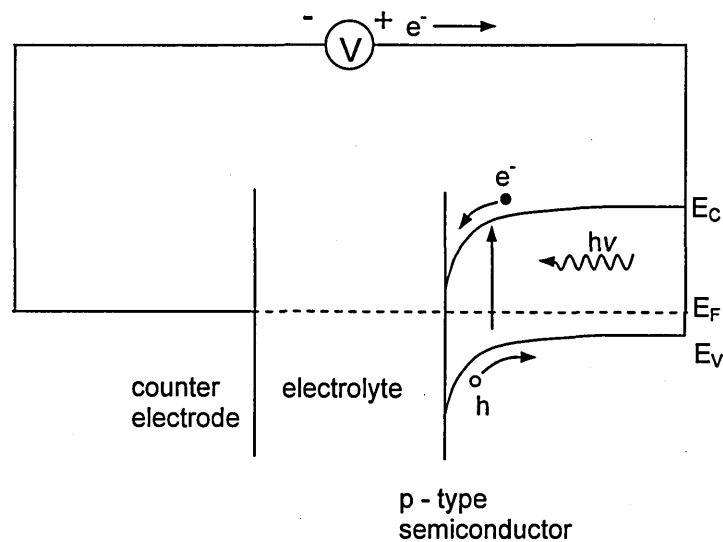
**Figure 4.2.** Configuration of glancing angle diffractometer [115].

### 4.1.3 The Photoelectrochemical Cell (PEC)

The PEC cell is essentially a liquid/solid junction solar cell, which can be used as a characterisation tool for the determination of the electrical conductivity type of the semiconductor. When the semiconducting electrode is immersed in a suitable electrolyte, the Fermi level (or chemical potential) must be identical if no external potential is applied. As in a p-n junction the conduction and valence bands bend to accommodate this, as described in chapter 1.3.1.



(a)



(b)

**Figure 4.3.** Band diagrams of (a) n-type semiconductor/liquid junction and (b) p-type semiconductor/liquid junction.

When illuminated electron hole pairs are created within the depletion zone, and the built-in electric field will separate the photo generated electron and hole pairs. If the semiconductor is n-type the holes move towards the surface of the semiconductor and the electrons move into the bulk of the material (see figure 4.3a). If an external circuit is made with a counter electrode immersed in the solution, the electrons will flow from the semiconductor to the counter electrode to reduce cations in the solution. For a p-type semiconductor, electron flow is in the opposite direction, electrons leave the surface of the semiconductor to reduce cations of the solution (see figure 4.3b). Therefore from the direction of the current or the polarity of the voltage measured in the external circuit the electrical conductivity type of the semiconductor can be established.

#### 4.1.4 Scanning Electron Microscopy (SEM)

SEM is a non-destructive technique which can be used to study the morphology of the samples [116].

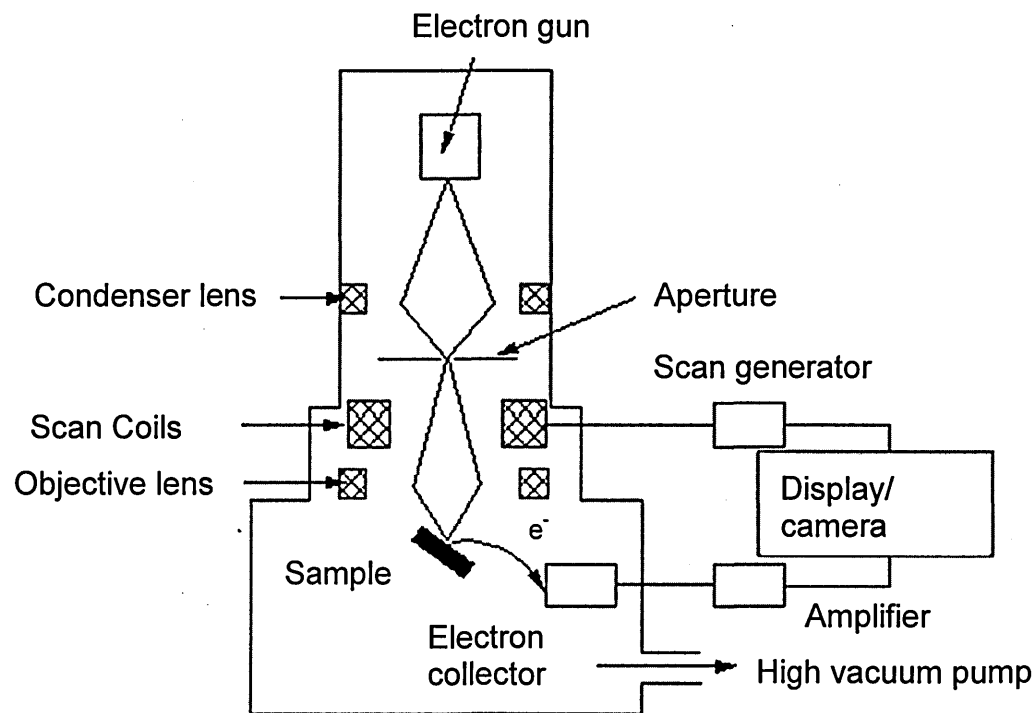


**Figure 4.4.** Schematic diagram of key components of SEM (note only one condenser lens shown for clarity).

An electron beam is generated by an electron gun which is located at the top of the column. The beam is then condensed by the first condenser lens, in conjunction with the condenser aperture to eliminate some high angle electrons (coarse focus). A second condenser lens focuses the beam into a thin, coherent beam (fine focus). Then a set of coils scan the beam into a grid pattern. The final lens (objective) then focuses the scanned beam onto the desired area of the sample. To avoid absorption and scattering of electrons the process is carried out in a vacuum. When the beam strikes the sample several interactions take place and can be detected by an appropriate detector.

For this work only the surface morphology is investigated, where the creation of secondary electrons are utilised. Secondary electrons are caused by an incident electron passing "near" an atom in the specimen, near enough to impart some of its energy to an electron within the atom. This causes a slight energy loss and path change in the incident electron and the ionization of the electron in the specimen atom. This ionized electron then leaves the atom with a very small kinetic energy (5 eV). Because of their low energy, only electrons near the surface of the sample can exit the sample and therefore detected, giving a picture of the surface of the sample.

Two other interactions that are often utilised from an SEM are back scattered electrons (BSE), which gives the atomic number from the part of sample, from where they originate and if an energy dispersive X-ray (EDX) spectrometer is fitted, the atomic composition of the sample can be obtained.

#### **4.1.5 Atomic Force Microscopy (AFM)**

##### **4.1.5.1 Introduction**

AFM is a relatively new technique, developed in 1986 [117], it has the advantage over conventional optical and electron microscopes, in that it is able to resolve images down to single atoms. It also provides a vertical view, and therefore the image is three dimensional and the resulting image is a true topographic view of the sample. Another advantage is that AFM's do not need a vacuum and they can work in ambient or liquid

environments without requiring special sample preparation. A schematic diagram showing the major parts of an AFM is shown in figure 4.5.

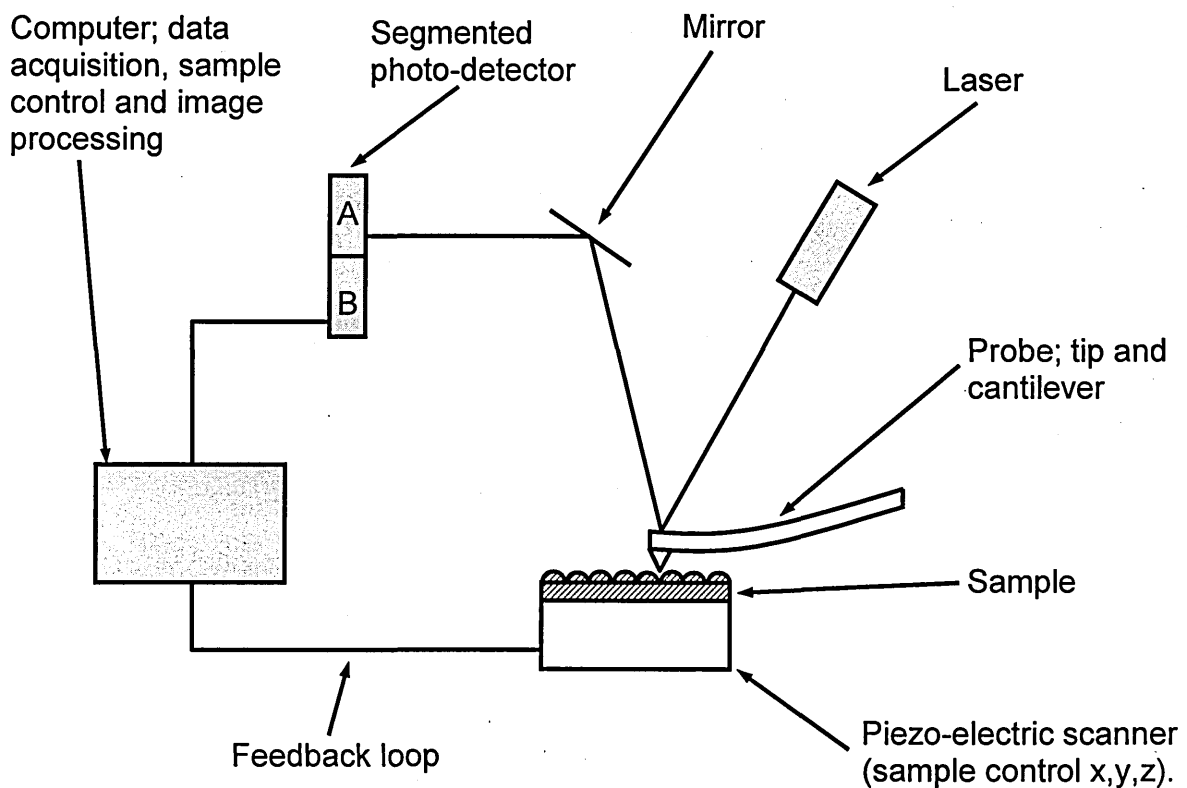


**Figure 4.5.** Schematic diagram showing the major parts of an AFM.

#### 4.1.5.2 Principle of AFM

In the most basic mode, the contact mode, AFM uses a probe to move across the samples surface to identify its features. The probe is a sharp tip usually made from silicon or silicon nitride, extending down from the end of a reflective cantilever. The tip doesn't actually touch the surface, it is held by repulsive forces a few angstroms above its surface. A laser beam is directed onto the cantilever, and as the tip scans the surface of the sample following the contours, the beam is deflected accordingly onto the dual element photo-detector. In practice the tip is stationary and the sample is moved very precisely by the piezo-electric scanner, which is under control, with a constant feedback loop from the computer which keeps the height of the sample constant, in order to keep a relatively constant deflection on the cantilever. The segmented photo-detector

measures the difference in light intensity between its upper and lower detectors, this is then converted into a voltage, which is processed in the computer where the three dimensional image is constructed.

#### 4.1.6 X-Ray Fluorescence (XRF)

XRF is a qualitative and quantitative non-destructive technique and was used to identify and determine the concentrations of the elements present in thin film samples [118]. When atoms within the sample are excited by high energy primary x-ray irradiation, electrons from the inner orbital are ejected in the form of photo-electrons leaving vacancies. These vacancies create an unstable ion, for energy to be conserved electrons from outer orbitals fill the inner shell vacancies, returning the atom to a more stable state. This transition will produce a secondary x-ray photon, whose wavelength is characteristic to a given element. This phenomenon is known as fluorescence. By detecting the specific wavelengths of the secondary x-rays that are emitted from the excited sample, the element can be identified, as the wavelength is related to the atomic number  $Z$  and the intensity of the emission (number of emitted photons) is proportional to the concentration of the particular element in the sample.

#### 4.1.7 Optical absorption

An optical spectrometer is an instrument to measure the properties of materials over a specific portion of the electromagnetic spectrum [22]. It is often used in astronomy and chemistry to identify elements, but this technique is also well suited to determine the bandgap of a semiconductor, from its optical absorption spectrum, which is defined from equation 4.5.

$$(\alpha h\nu) = C(h\nu - E_g)^{\frac{1}{2}} \quad (4.5)$$

Where  $\alpha$  is the absorption coefficient,  $C$  is a constant depending on the refractive index of the sample,  $h\nu$  is the energy of the absorbed photon and  $E_g$  is the bandgap of the semiconductor. This equation is only applicable to direct bandgap semiconductors [22].

The basic set up to measure the absorption/transmission of light through a sample is shown in figure 4.6.

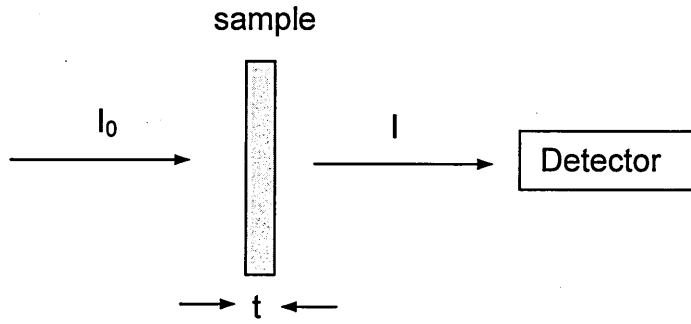


**Figure 4.6.** Schematic diagram of basic principle of absorption measurement, where  $I_0$  = Intensity of light incident on sample,  $I$  = Intensity after passing through the sample and  $t$  = thickness of sample.

$$\text{Transmission (T)} = \frac{I_0}{I} \quad (4.6)$$

Optical absorbance ( $A$ ) which is the value given by the spectrometer has the relationship;

$$A = -\log_{10} T \quad (4.7)$$

In equation 4.5,  $\alpha$  is the absorption coefficient, but since  $A$  is a function of  $\alpha$  which has the following relationship.

$$I = I_0 e^{-\alpha t} \rightarrow \alpha = \frac{2.303 A}{t} \text{ (cm}^{-1}\text{)} \quad (4.8)$$

And since  $t$  is constant for a given sample, a plot of  $(Ah\nu)^2$  versus  $h\nu$ , will yield the same information as  $(\alpha h\nu)^2$  versus  $h\nu$ . When  $(Ah\nu)^2 = 0$ ,  $h\nu = E_g$  and therefore by extrapolating the curve to intersect the x-axis, the bandgap ( $E_g$ ) can be determined. For the work presented in this thesis, the extrapolation of the linear part of the optical absorption curves was carried out by hand and therefore some slight error will be introduced, this was calculated to be +/- 0.01 eV.

UV-visible spectroscopy was used to measure the bandgap of CdS and FTO, as these are wide bandgap semiconductors. Low bandgap semiconductors like CIS need to be studied by infrared spectroscopy.

#### 4.4.7.1 UV-visible spectroscopy

A schematic diagram of a UV-visible spectrometer is shown in figure 4.6.

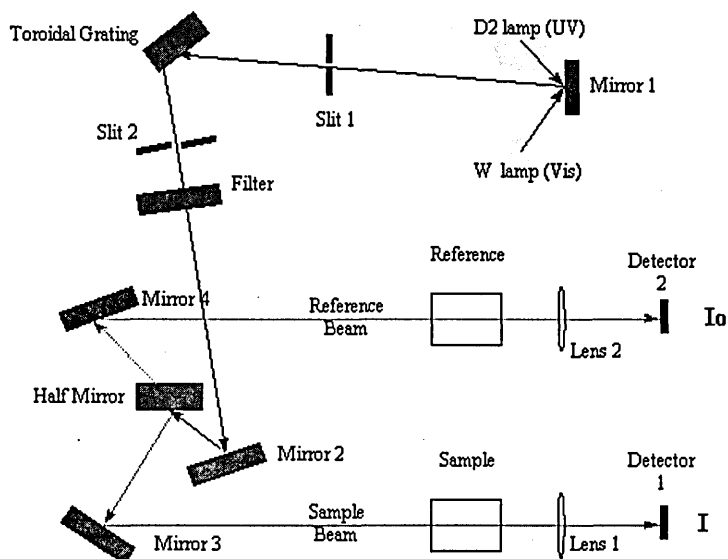


**Figure 4.6.** Schematic diagram of a UV-visible spectrometer [120].

The spectrometer used for all measurements was an ATI-Unicam UV-Vis2, which is a dual beam spectrometer. Dual beam spectrometers have the advantage that the spectra from both the sample and the reference are obtained simultaneously and any time dependant variations in the intensity of the light can be compensated for, thus making the technique more sensitive.

The UV lamp is a deuterium ( $D_2$ ) lamp, and the visible lamp is a tungsten filament lamp, and the monochromator (diffraction grating) disperses the light into the complete spectrum. The beam is split by a beam splitter, where it passes through both the sample and the reference. A detector compares the difference in energy passing through the sample and the reference and thereby the absorption can be calculated. The data is normally represented as a plot of absorption versus wavelength.

## 4.2 Device characterisation

### 4.2.1 Introduction

Three techniques were used to characterise the solar cell devices, current voltages (I-V), capacitance voltage (C-V) and quantum efficiency (QE).

### 4.2.2 Current Voltage measurements (I-V)

This is the most important technique for solar cell assessment, where the open circuit voltage ( $V_{oc}$ ), short circuit current ( $I_{sc}$ ), fill factor (FF) and overall efficiency ( $\eta$ ) can be found, by simply measuring the I-V characteristics. A typical I-V curve, both in the dark and under illumination is shown in figure 4.8.

The equivalent circuit of a 'real' solar cell is shown in figure 4.7, which can be considered as a diode in parallel with a shunt resistance ( $R_{sh}$ ), in conjunction with another resistance ( $R_s$ ) in series. The  $R_{sh}$  is caused by defect levels/recombination centres within the cell and can cause an alternate path for the current to flow (leakage current), ideally all the current should flow through the diode, i.e.  $R_{sh}$  should be infinite.  $R_{sh}$  can be evaluated from the gradient of the reverse part of the I-V curve. The  $R_s$  is caused by the resistance of the bulk of the semiconductor, metal contacts and other interfaces, ideally this should be zero and can be evaluated from gradient of the high forward part of the I-V curve. The current source ( $I_{gen}$ ) represents the photogenerated current in the solar cell.

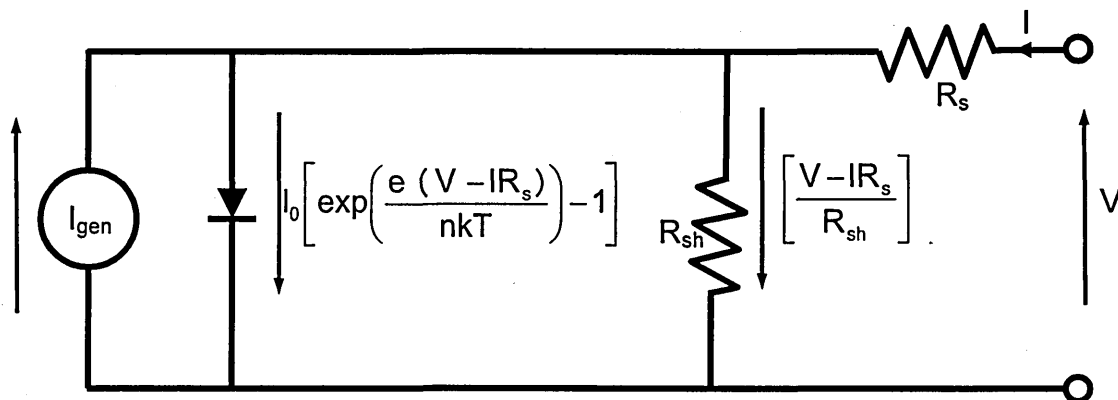
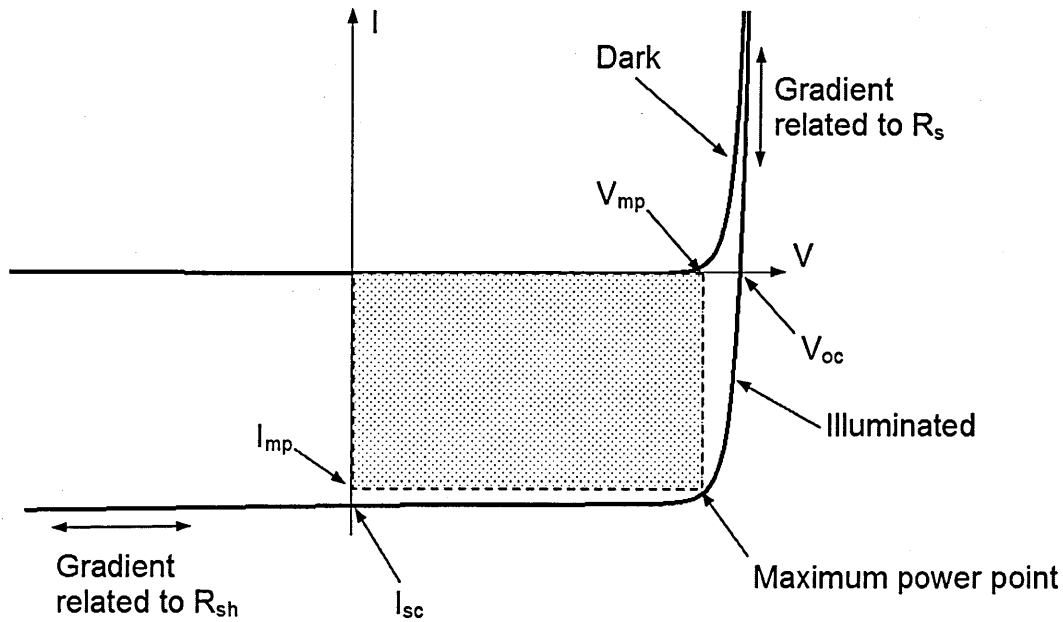


Figure 4.7. Equivalent circuit of an illuminated solar cell [119].



**Figure 4.8.** I-V characteristics of a solar cell under dark and illuminated conditions, showing important parameters.

Under dark conditions, a solar cell is a simple diode and the current voltage relationship is given by the ideal diode equation [22].

$$I = SA^*T^2 \exp\left(\frac{-e\phi_b}{kT}\right) \left[ \exp\left(\frac{eV}{nkT}\right) - 1 \right] \quad (4.9)$$

where

- S = Area of the contact
- A\* = Effective Richardson constant
- $\phi_b$  = Potential barrier height
- e = Electron charge
- k = Boltzmann constant
- T = Temperature
- n = Diode quality factor

Or it can be simplified to;

$$I = I_0 \left[ \exp\left(\frac{eV}{nkT}\right) - 1 \right] \quad (4.10)$$

Where  $I_0$  = the saturation current of the diode.

When this is applied to a practical solar cell under illumination as shown in figure 4.7, the current voltage relationship is given by;

$$I = I_0 \left[ \exp\left(\frac{e(V - IR_s)}{nkT}\right) - 1 \right] + \left[ \frac{V - IR_s}{R_{sh}} \right] - I_{sc} \quad (4.11)$$

This can then be reduced, if  $V > \frac{3kT}{e}$  ( $\sim 75$  mV),  $R_s = 0$  and  $R_{sh} = \infty$

$$I = I_0 \exp\left(\frac{eV}{nkT}\right) - I_{sc} \quad (4.12)$$

The three parameters used to characterise a solar cell are; short circuit current ( $I_{sc}$ ), open circuit voltage ( $V_{oc}$ ) and fill factor (FF), which can be obtained from the I-V curve. The overall efficiency ( $\eta$ ) can then be calculated from their relationships.

$I_{sc}$  is found where the curve intersects the y-axis, which is the same as the photogenerated current. This can also be found by setting  $V = 0$  in equation 4.12.

$V_{oc}$  is found where the curve intersects with the x-axis, when the current equals zero. Again this can be found from equation 4.12, by setting  $I = 0$  when  $V = V_{oc}$  and solving for  $V_{oc}$ , which gives;

$$V_{oc} = \frac{nkT}{e} \ln\left(\frac{I_{sc}}{I_0}\right) \quad (4.13)$$

Fill factor (FF) is a parameter which in conjunction with  $V_{oc}$  and  $I_{sc}$  determines the maximum power that can be delivered from the solar cell. FF is defined as the ratio of the product of maximum power ( $V_{mp} \times I_{mp}$ ) and the product of the maximum current and voltage ( $V_{oc} \times I_{sc}$ ). FF is practically the measure of 'squareness' of the I-V curve, see figure 4.8.

$$FF = \frac{V_{mp} \times I_{mp}}{V_{oc} \times I_{sc}} \quad (4.14)$$

The overall efficiency ( $\eta$ ) of the solar cell is a function of all the above parameters,  $V_{oc}$ ,  $I_{sc}$  and FF, where;

$$\eta = \frac{\text{Output power}}{\text{Input power}} = \frac{V_{oc} I_{sc} FF}{P_{in}} \quad (4.15)$$

Where  $P_{in}$  is the power of the incident light, and is set to  $1000 \text{ Wm}^{-2}$  for AM 1.5 conditions.

By rearranging equation 4.12, other useful information can be gained from the dark I-V characteristics;

$$\text{Log}_{10}I = \left( \frac{e}{2.303nkT} \right) V + \text{log}_{10}(I_0) \quad (4.16)$$

A plot of  $\text{log}_{10}(I)$  versus (V) yields a straight line and from this the diode quality factor (n) and the barrier height ( $\phi_b$ ) can be calculated.

The diode quality factor can be evaluated from the gradient of the curve;

$$\text{Gradient} = \left( \frac{e}{2.303nkT} \right) \quad (4.17)$$

For pure thermionic emission of electrons over the barrier  $n = 1.00$  and for pure recombination and generation  $n = 2.00$  [22].

The barrier height can be calculated from the intercept of the straight line on the y-axis, this gives a value for  $I_0$  and therefore from the relation given in equation 4.9,  $\phi_b$  can be evaluated. The value of  $\phi_b$  is only valid for ideal diodes, i.e. n values close to 1.00, if recombination and generation occur, the value for  $I_0$  will increase and therefore the value for the barrier height will be under estimated.

### 4.2.3 Quantum Efficiency (QE)

Quantum Efficiency (QE) is a ratio the number of electrons delivered to the external circuit to the number of photons of a given energy incident on the solar cell [23]. It gives a very good measure of how the cell is performing at each particular wavelength. In an ideal solar cell, if all the incident photons with energy  $E > E_g$  promote exactly one electron to the conduction band and is collected in the external circuit, the QE will be equal to unity. This would produce a rectangular QE curve with  $QE=1$ , as shown in figure 4.9a. In practical solar cells losses due to recombination, reflection and low diffusion length takes place, a typical QE curve is shown in figure 4.9b.

There are two types of quantum efficiency which are used in solar cell measurement:

- (i) External QE, this includes the effects of optical losses such as transmission through the cell and reflection from the surface.
- (ii) Internal QE, this refers to the efficiency with which photons that are not reflected or transmitted from the cell can generate collectable charge carriers. Internal QE is also referred to as IPCE (Incident Photon to Charge carrier Efficiency), this is the method used to measure the cells presented in this thesis.

The photogenerated current density is related to the quantum efficiency by equation:

$$J_{sc} = e \int_0^{\infty} QE(E)b_s(E)dE \quad (4.19)$$

Where  $b_s$  is equal to the spectral photon flux and  $QE(E)$  is the probability that an incident photon of energy  $E$  will deliver an electron to the external circuit.

As mentioned in the introductory chapter 1.2.2, under certain circumstances the quantum efficiency can be greater than unity.

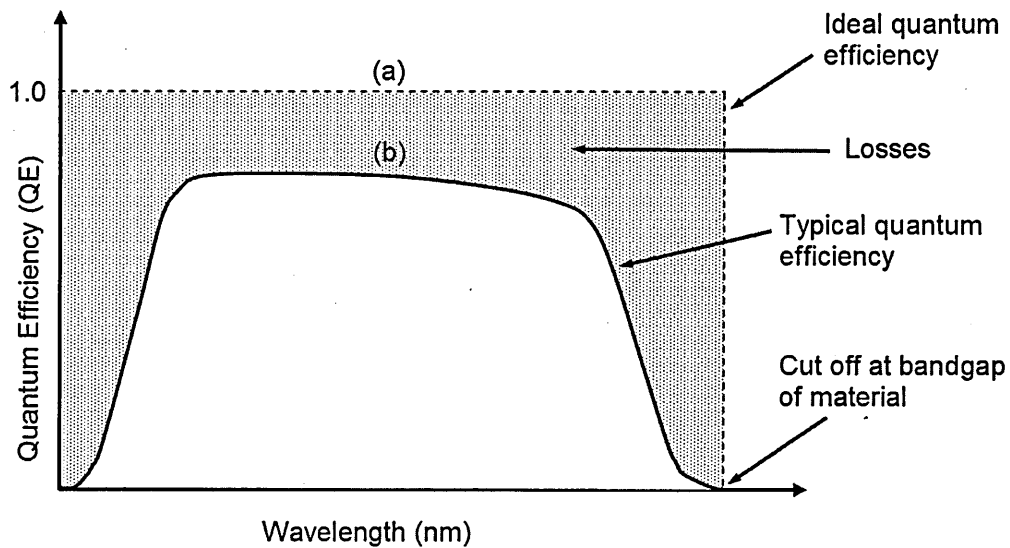


**Figure 4.9.** Diagram of Quantum Efficiency curves, curve (a) shows an ‘ideal’ solar cell with QE equal to unity and curve (b) shows a ‘real solar cell’.

#### 4.2.4 Capacitance voltage measurements (C-V)

From the measurement of the junction capacitance, the depletion width  $w$ , the doping concentration  $N_d$  or  $N_a$  and the barrier height  $\phi_b$  can be calculated. The principles of differential CV measurements, is a high frequency AC signal (usually 1 MHz), is super imposed with a DC bias voltage. The AC signal is used to ‘probe’ the junction, containing charges on both sides of the junction associated with the depletion regions. From the relationship given in equation 4.20, the doping concentration can be found, from a plot of  $1/C^2$  versus  $V$ . If the material is uniformly doped the plot will be a straight line, whose gradient is inversely proportional to the doping concentration [120].

$$\frac{1}{C^2} = \left( \frac{2}{\epsilon_s A^2 e N_d} \right) (V + V_{bi}) \quad (4.20)$$

If  $N_A \gg N_D$

Where:

$V_{bi}$  = The built in potential, which can be found from the intercept on the x-axis.

$\epsilon_s$  = Permittivity of the semiconductor

The rest of the symbols have their usual meaning.

The barrier height can be determined from equation 4.21 and is dependent on the built in potential  $V_{bi}$ .

$$\phi_b = V_{bi} + \xi \quad (4.21)$$

Where  $\xi$  is the energy difference between Fermi level and the conduction band for an n-type semiconductor and valence band for a p-type, (approximately taken as 0.1 eV for a moderately doped semiconductor).

The depletion width can be determined from equation 4.22:

$$W = \sqrt{\frac{2\epsilon_0\epsilon_s}{eN_d}(V + V_{bi})} \quad (4.22)$$

## **Chapter 5: Development of AlGaAs devices with p-type window material**

### **5.1 Introduction**

Global photovoltaic research is currently focussed on the production of low-cost and high-efficiency solar cells. Several different systems are being researched and developed with some successfully commercialised already. All-solid and inorganic PV solar cells are based on crystalline, polycrystalline and amorphous silicon, III-V compounds and polycrystalline CdTe and CuInGaSe<sub>2</sub> (CIGS) thin films. The three main materials used at present are silicon, CdTe and CIGS, but there are various issues with each of these three types, in terms of reproducibility, variations in performance, stability and lifetime. In order to address these issues, new device designs have been proposed [20] based on p-type window materials instead using the conventional n-type window material, such as CdS.

These new designs have been experimentally tested with the well researched GaAs and Al<sub>x</sub>Ga<sub>(1-x)</sub>As alloy system based on the 'new model' proposed by Dharmadasa et al [20]. This chapter presents the background to the development of the new model, the progress of these multi-layer graded bandgap solar cells and how defects affect the reproducibility and performance of thin-film solar cells.

### **5.2 Background to the development of the 'new model'**

The basic CdTe thin film solar cell consists of two semiconducting layers, a wide band gap n-type CdS layer ( $E_g=2.42$  eV) and a CdTe p-type layer ( $E_g=1.45$  eV). The device structure is then a simple n-p hetero-junction with an ohmic contact at the p-CdTe/metal interface.

In 1984 Basol [121] successfully fabricated such a device using electrodeposited CdTe which achieved efficiencies of ~10%. The photovoltaic effect was explained by

assuming that there is an n-type to p-type conversion of the CdTe layer during the 20 minute, 400°C post growth annealing process.

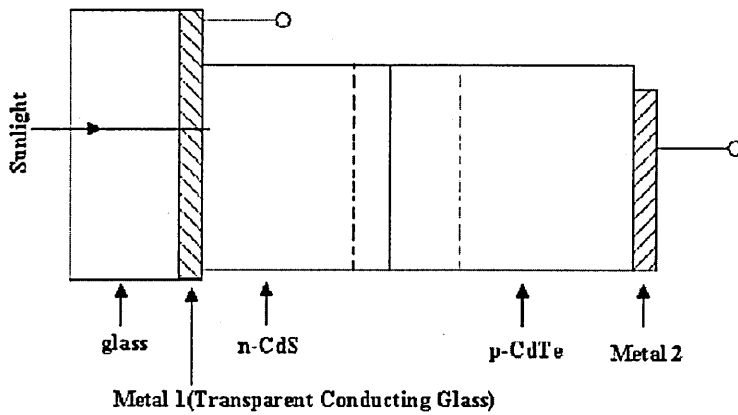


**Figure 5.1.** Schematic diagram of the CdS/CdTe device structure fabricated by Basol [122].

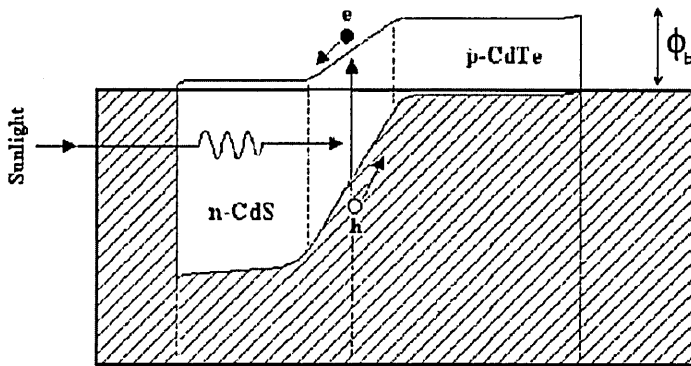


**Figure 5.2.** Band diagram according to Basol model for CdS/CdTe solar cell [122].

Although the Basol model gave a good scientific explanation of the PV action of the device at the time it was developed, this model has been accepted without further testing or confirmation over the last 25 years. Most of the research has been based on this model, which may have slowed down development of this device. The efficiency of the device slowly increased to a maximum so far of 16.5% , achieved in 2004 [123].

### 5.2.1 The new model (~2002)

From work carried out over the past 20 years on metal/CdTe interfaces, Dharmadasa et al have proposed a new model based on a peculiar property of metal/CdTe interfaces,

first reported in a review article in 1998 [124]. It was demonstrated that the barrier height for a metal/n-CdTe interface is, in fact, independent of the metal work function, and depends on the Fermi level pinning at one of the 5 experimentally observed defect levels.

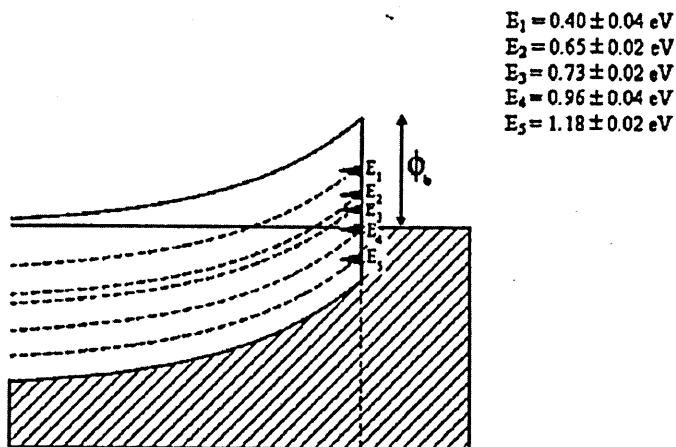


**Figure 5.3.** Defect levels at metal/n-CdTe interface, experimentally identified by photoluminescence, DLTS and BEEM [122].

According to this model, the bulk of the CdTe remains n-type and the outermost layer contains high concentrations of defects responsible for Fermi level pinning at one of the five experimentally observed discrete levels, forming a Schottky barrier. The device structure is now an n-CdS/n-CdTe hetero-junction together with a large Schottky barrier at the back metal contact (see figure 5.4) [122].

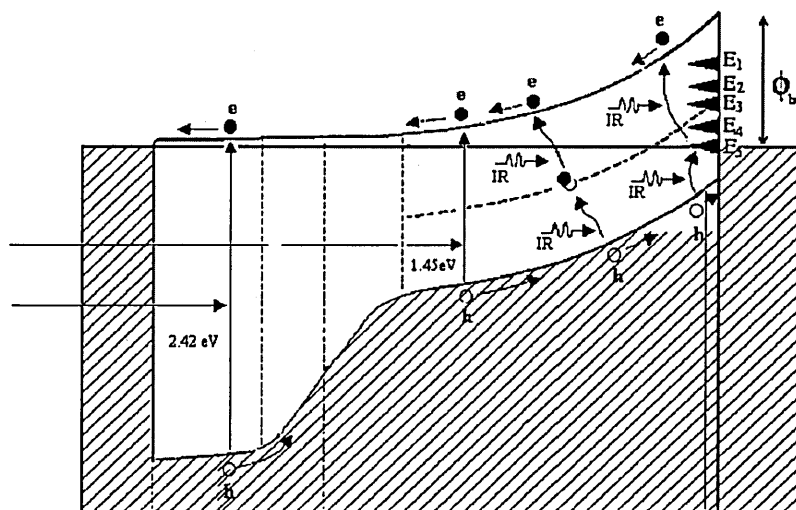


**Figure 5.4.** Energy band diagram of an n-CdS/n-CdTe hetero-junction, together with a large Schottky barrier at the back metal contact, based on the new model [122].

The new model has enabled the interpretation of previously unexplained results observed by Dharmadasa et al in the mid 1980s [66], in particular the effects of changes in current-voltage characteristics on certain properties of metal/CdTe interfaces.

The model demonstrates that in order to produce a stable and efficient solar cell, the defects need to be identified, with defect levels  $E_1$ - $E_4$  being removed or passivated. This leaves the Fermi level pinning at  $E_5$ , producing the largest Schottky barrier height, which is the most important for an efficient solar cell, see figure 5.4.

Recent work on electrical contacts to p-type CIGSS shows that this material also exhibits the existence of similar defect structures and therefore are expected to behave the same way as CdTe solar Cells. The Fermi level pinning positions at metal/p-CIGS interface are shown in figure 5.5. [125].

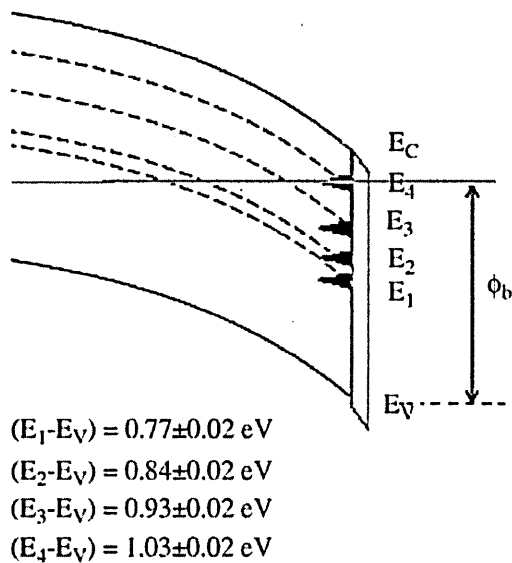


**Figure 5.5.** Fermi level pinning positions at metal/p-CIGS interface [125].

This work has led to the development of CIGS graded bandgap multilayer thin film solar cells, which is discussed in chapter 7 of this thesis. This incorporates two important features for multilayer thin film solar cells: i) band gap variation from large to small and ii) electrical conduction type variation from n- to p-type. This can be extended to multilayer devices with both n-type and p-type window layers as shown in figure 5.6.

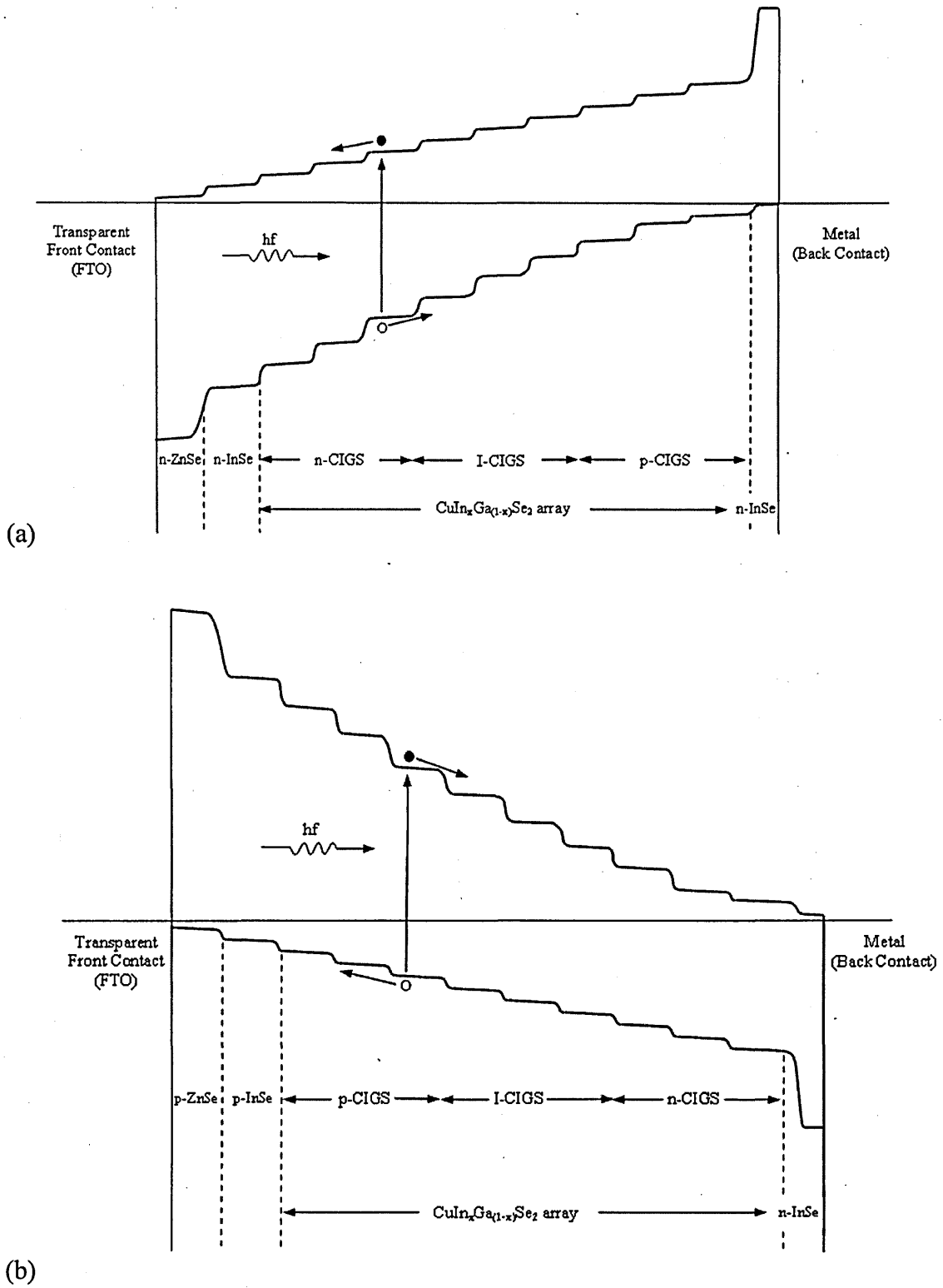


**Figure 5.6.** Graded bandgap multilayer structures with both n-type window (a) and p-type window (b) materials.

## 5.3 Experimental

Well researched GaAs and  $\text{Al}_x\text{Ga}_{(1-x)}\text{As}$  materials grown using MOCVD were chosen to experimentally test the recently proposed device structures, which have a graded bandgap structure and a p-type window. The device structures were grown on n-type GaAs substrates, the bandgap of the semiconducting layers was gradually increased, whilst the electrical conductivity type was changed from n-type to p-type.

### 5.3.1 Details of MOCVD growth

The solar cell structures were deposited using atmospheric pressure MOCVD, at a temperature of  $736^\circ\text{C}$ , using conventional reagents, trimethylgallium (TMG), trimethylaluminium (TMA) and arsine ( $\text{AsH}_3$ ). Starting from the back of the cell, the n-GaAs wafer, Al was gradually added to increase the bandgap of the cell. Simultaneously Si was added as an n-type dopant, decreasing linearly, until an i-type layer was formed in the middle of the cell. Then as the Al content was increased, the residual carbon p-type dopant from the TMA also gradually increased. The maximum doping concentrations for the n-type and p-type dopants were  $5 \times 10^{17} \text{ cm}^{-3}$  and  $\sim 1 \times 10^{17} \text{ cm}^{-3}$  respectively. The change in composition ranged from essentially GaAs to  $\text{Al}_{0.4}\text{Ga}_{0.6}\text{As}$ , resulting in a PIN cell structure. Finally a 4.5 nm thick  $2 \times 10^{18} \text{ cm}^{-3}$  p-doped  $\text{Al}_{0.8}\text{Ga}_{0.2}\text{As}$  window layer was deposited on the  $\text{Al}_{0.4}\text{Ga}_{0.6}\text{As}$ , followed by a 200 nm p-GaAs capping layer. This capping layer was introduced to prevent oxidation of aluminium in the  $\text{Al}_x\text{Ga}_{(1-x)}\text{As}$  layers. The detailed growth and full processing details are described in a previously published paper [20] and the approximate band diagram of the device structure is shown in Figure 5.7.

Three types of devices were processed with solar cell areas of  $0.002 \text{ cm}^2$  (0.5 mm diameter dots),  $0.090 \text{ cm}^2$  ( $3 \times 3 \text{ mm}^2$  cells) and  $0.250 \text{ cm}^2$  ( $5 \times 5 \text{ mm}^2$  cells) respectively. These devices were then assessed using I-V (current voltage), QE (quantum efficiency) and C-V (current voltage) techniques and were sent to several laboratories for ratification of results. These laboratories are Imperial College London and South Bank University in the UK, Zürich and Lausanne laboratories in Switzerland and NREL in the United States.

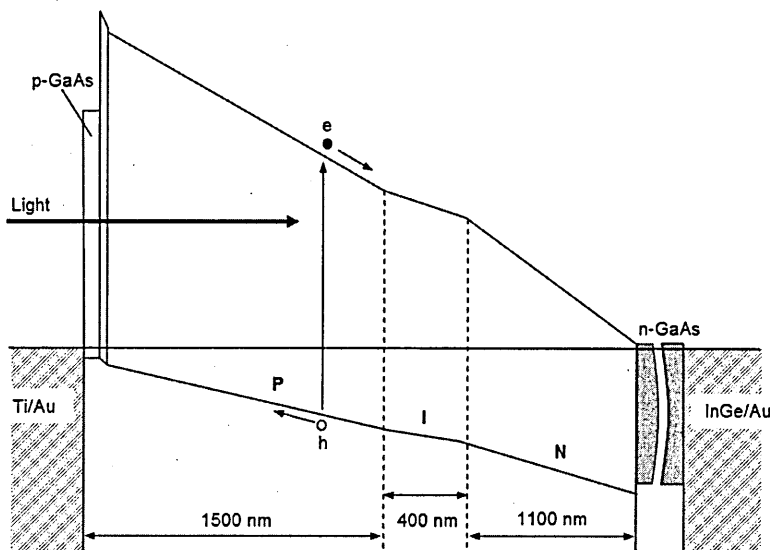


**Figure 5.7.** Sketch of the energy band diagram for the  $\text{Al}_x\text{Ga}_{(1-x)}\text{As}/\text{GaAs}$  solar cell studied in this section.

## 5.4 I-V and QE results

### 5.4.1 First batch ( $0.002 \text{ cm}^2$ ) 0.5 mm diameter solar cells

The first batch fabricated were 0.5 mm diameter dots, and contained the  $0.2 \mu\text{m}$  thick n-type GaAs capping layer. Two sets of samples were tested, one with the full capping layer and one with the capping layer partially removed. It is evident from the results shown in Table 5.1 that the capping layer is detrimental to the device performance. Table 5.2 summarises the best device parameters, with  $V_{oc}$  (1070-1110 mV), FF (0.80-0.83) and  $J_{sc}$  ( $12.3\text{-}13.0 \text{ mA cm}^{-2}$ ).

**Table 5.1.** Device parameters with and without capping layer.

Device		$J_{sc}$ ( $\text{mA cm}^{-2}$ )	$V_{oc}$ (mV)	FF
With capping layer	1	12.7	1110	0.83
	2	12.6	1070	0.78
	3	12.5	1075	0.82
With capping layer partially removed	1	6.2	1060	0.83
	2	6.7	1060	0.81
	3	5.6	1050	0.81

**Table 5.2.** Summary of best device parameters observed for 0.5 mm diameter devices, without the capping layer, as measured in four different solar energy research laboratories.

Device	$V_{oc}$ (mV)	FF	$J_{sc}$ (mA cm <sup>-2</sup> )	$\eta\%$	Place of Assessment
1	1110	0.83	12.7	11.7	SHU Labs
2	1075	0.82	12.5	11.0	(Dharmadasa et al)
3	1081	0.82	12.3	11.0	Zürich Labs
4	1077	0.82	12.3	10.8	(A. N. Tiwari et al)
5	1090	0.81	13.3	12.1	SBU Labs
6	1090	0.81	12.9	11.6	(Hari Reehal et al)
7	1070	0.80	13.0	11.1	EPFL Labs (Michael Grätzel et al)

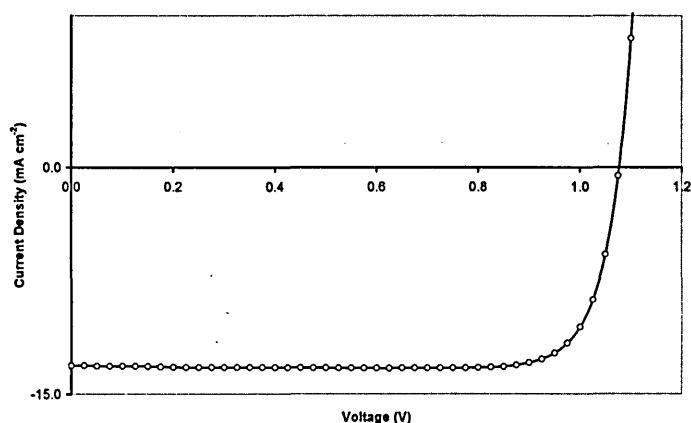


**Figure 5.8.** Typical I-V curve for 0.5 mm diameter solar cell, with  $V_{oc} = 1081$  mV,  $FF = 0.82$  and  $J_{sc} = 12.3$  mA cm<sup>-2</sup>.

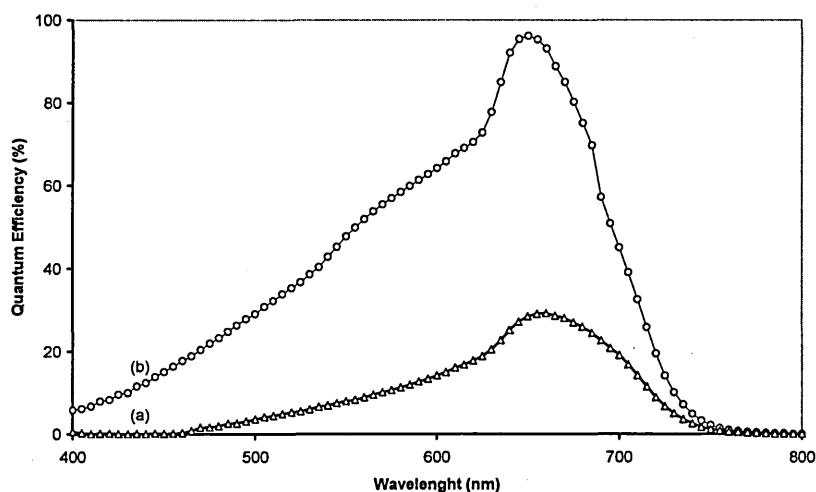


**Figure 5.9.** QE response for 0.5 mm diameter solar cell; (a) with cap and (b) with cap partially removed (measured at Imperial College, London).

Table 5.1 and figure 5.9, show that the capping layer is detrimental to the device performance, with the current density reducing from 12-13 mA cm<sup>-2</sup> to 5-7 mA cm<sup>-2</sup> and the reduction in spectral response.

The QE curves show that these devices have considerable losses in both the blue and red regions of the spectrum. These losses are thought to be caused by the remains of the GaAs capping layer, which effectively absorbs both the high energy photons and

photons with energy approximately equal to that of the GaAs band gap. The photo-generated electrons and holes recombine at the front contact, and do not contribute to the current in the external circuit.

For this reason the QE response is missing near the GaAs cut-off wavelength at ~855 nm (~1.45 eV).

The maximum observed from the QE curve of 650 nm corresponds to the maximum photon intensity of the solar spectrum, which shows the transmission of photons through the remains of the GaAs capping layer at the front of the device. The comparison of current between diodes with and without partial removal of p-GaAs layer confirmed this explanation.

#### **5.4.2 Second batch (0.090 cm<sup>2</sup>) 3×3 mm<sup>2</sup> solar cells**

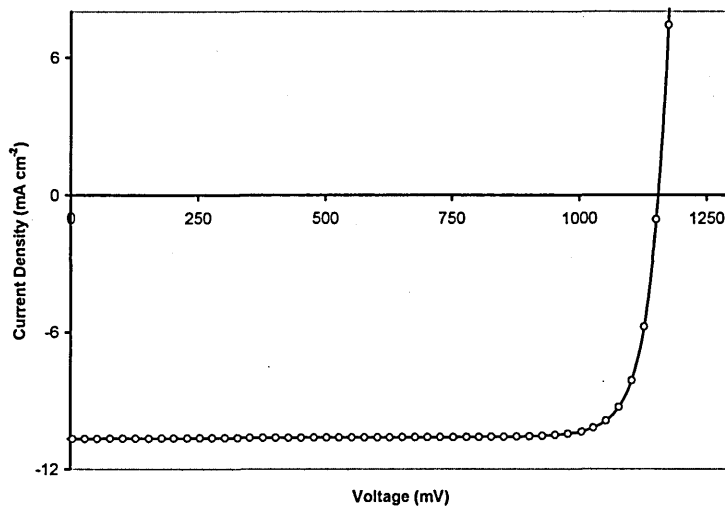
In order to improve the devices, various alterations were made: i) attempts were made to remove more GaAs and ii) a 120 nm thick MgF<sub>2</sub> anti-reflection coating was introduced. The device size was increased to 0.090 cm<sup>2</sup> (3×3 mm<sup>2</sup>) in order to test the effect of scaling up and to calculate more accurate J<sub>sc</sub> and efficiency values.

**Table 5.3.** Summary of best device parameters observed for ( $3\times 3\text{ mm}^2$ ) devices, as measured in five different solar energy research laboratories.

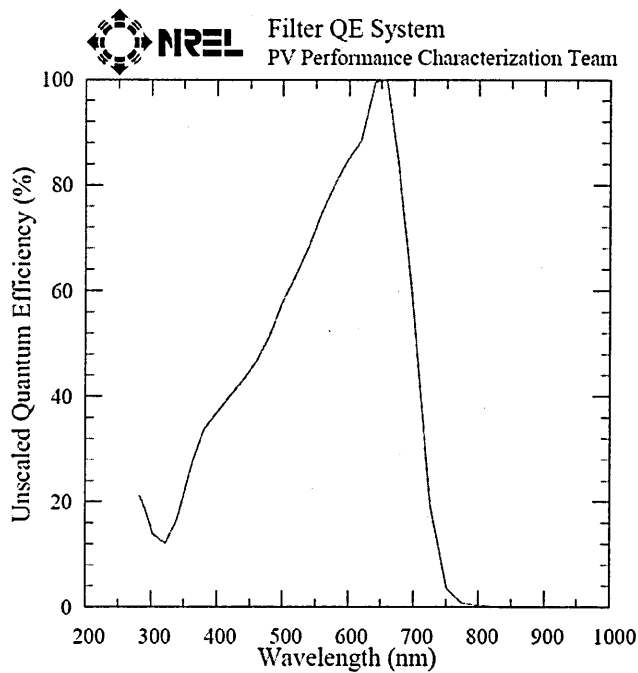
Device	$V_{oc}$ (mV)	FF	$J_{sc}$ ( $\text{mA cm}^{-2}$ )	$\eta\%$	Place of Assessment
1	1175	0.87	10.7	10.9	SHU Labs
2	1160	0.86	11.5	11.5	
3	1148	0.86	10.7	10.6	Zürich Labs
4	1141	0.86	10.3	10.1	
5	1169	0.85	11.5	11.4	SBU Labs
6	1149	0.86	10.0	9.9	
7	1150	0.85	12.1	11.8	EPFL Labs
8	1159	0.85	12.3	12.1	NREL - USA
9	1156	0.85	11.9	11.7	

Figure 5.10 shows a typical I-V curve for a ( $3\times 3\text{ mm}^2$ ) solar cell and Table 5.3 a summary of device performance. The main observation is the improvement in  $V_{oc}$  (1141-1175 mV) and FF (0.85-0.87), but a slight reduction in  $J_{sc}$  ( $10.3\text{-}12.3\text{ mA cm}^{-2}$ ).

This is because the  $J_{sc}$  values were calculated using the total area of  $0.09\text{ mm}^2$ , neglecting the effect of shading due to the front contacts. The area of the contacts was measured, which was found to reduce the effective area by 10%, and when this value was used to calculate  $J_{sc}$ , they were in the same range as the  $0.5\text{ mm}$  diameter cells, i.e.  $12\text{-}14\text{ mA cm}^{-2}$ . The improvement in FF and  $V_{oc}$  is primarily due to the removal of more of the capping layer.



**Figure 5.10.** Typical I-V curve for ( $3\times 3\text{ mm}^2$ ) diameter solar cell, measured at Zürich laboratory.



**Figure 5.11.** QE response for 3×3 mm<sup>2</sup> solar cells as measured at NREL, USA.

QE measurements carried out at NREL as shown in Figure 5.11, again show losses at both the blue and red ends of the spectrum, which suggest that a substantial part of the GaAs capping still remains.

#### 5.4.3 Third batch (0.250 cm<sup>2</sup>) 5×5 mm<sup>2</sup> solar cells

The third batch increased the size further to 0.25 cm<sup>2</sup> devices (again the removal of the GaAs capping layer was attempted, by selective etching). A typical I-V curve is shown in figure 5.12 and a summary of measured parameters at different labs is shown in table 5.4. The results confirm the reproducibility of high  $V_{oc}$ 's in the range (1120 - 1150) mV and FF's mainly in the range (0.82 – 0.86). The current density has reduced to (7.5 - 9.4) mA cm<sup>-2</sup>, again this was calculated using a total area of (0.25 cm<sup>2</sup>), neglecting the effect of shading from the front contacts, which cover 25% of the device. Figure 5.13 shows the QE results for these cells and again show the same losses as the 0.5mm and 3×3 mm<sup>2</sup> cells, suggesting that the GaAs cap is still present, or indicates a different reason is responsible for these losses.

**Table 5.4.** Summary of device parameters observed for  $5 \times 5 \text{ mm}^2$  solar cells, as measured in five different solar energy research laboratories.

Device	$V_{oc}$ (mV)	FF	$J_{sc}$ ( $\text{mA cm}^{-2}$ )	$\eta\%$	Place of assessment
S1	1137	0.85	7.10	6.9	SHU Labs
S2	1137	0.85	7.16	6.9	
3	1137	0.86	7.48	7.3	
4	1132	0.82	7.62	7.1	
S1	1140	0.83	8.76	8.3	SBU Labs.
S2	1150	0.83	8.79	8.4	
3	1140	0.83	9.41	8.9	
4	1120	0.78	9.02	7.9	
S1	1130	0.84	7.47	7.1	EPFL Labs
3	1120	0.84	7.98	7.5	
S2	1123	0.77	8.11	7.0	Zürich Labs
4	1127	0.85	7.96	7.6	

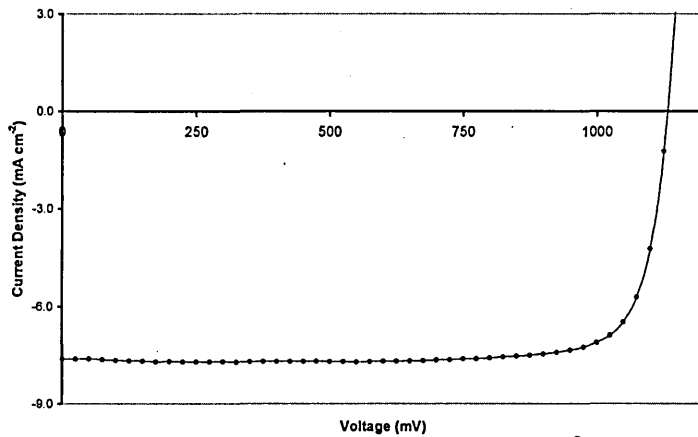


**Figure 5.12.** Typical I-V curve for  $5 \times 5 \text{ mm}^2$  solar cells, measured at SHU laboratory.

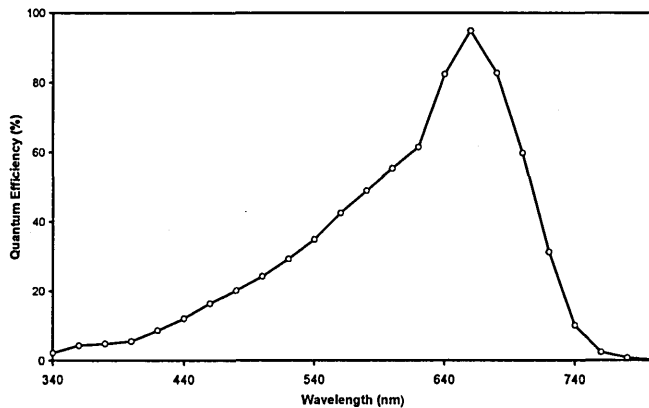


**Figure 5.13.** QE response for  $5 \times 5 \text{ mm}^2$  solar cells, measured at Imperial College, London.

#### 5.4.4 Calculation of other parameters from I-V data

The barrier height ( $\phi_b$ ), the diode quality factor ( $n$ ) and rectification factor were calculated, for a number of 0.5 mm diameter devices, they all gave similar values. A typical semi-log I-V curve is shown in figure 5.14, the barrier height was calculated to be 1.38 eV, with a diode quality factor of 1.65 and a rectification factor (RF) of 5 orders of magnitude at 1.0V. Note figure 5.14 is showing a  $V_{oc}$ , therefore this device was not measured in total darkness and therefore there must be some background light during the measurement.

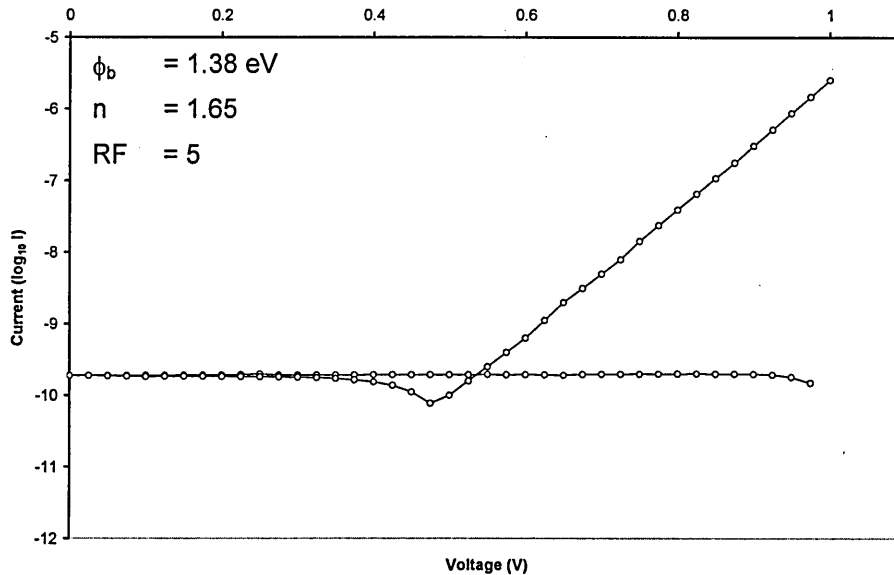


**Figure 5.14.** Semi-log I-V curve for a typical 0.5 mm diameter device.

#### 5.5 Capacitance voltage measurements (C-V)

The capacitance-voltage has been investigated using a frequency of 1 MHz, in order to calculate the doping concentration, the depletion width and the barrier height. The barrier height was estimated for comparison with the value obtained from the I-V characteristics. A typical Schottky-Mott plot for a 0.5 mm device is shown in figure 5.15, the graph shows a good straight line in reverse bias, indicating uniform doping and gives a doping concentration of  $4 \times 10^{17} \text{ cm}^{-3}$ . The depletion width was calculated to be  $0.34 \mu\text{m}$  and a barrier height of 1.80 eV was estimated using the diffusion voltage. This method usually over estimates the barrier height, due to the effect of defects in the device structure [23].

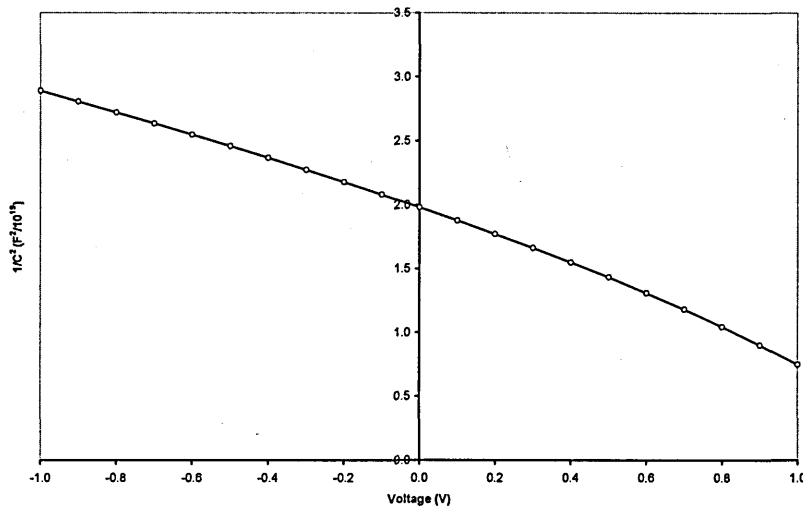


**Figure 5.15.** A typical Schottky-Mott plot for a 0.5 mm diameter device studied at 1 MHz, as a function of DC bias voltage.

## 5.6 Discussion of results

Throughout the scaling up process the  $J_{sc}$  has appeared to reduce steadily from  $\sim 13$  mA (0.5 mm diameter dots) to  $\sim 9$  mA ( $5 \times 5$  mm<sup>2</sup> devices), however the shading effect from the front contacts is considerable for the larger devices. Figure 5.17 shows a top view photograph of three devices having different dimensions. It was found that the front contacts cover  $\sim 25\%$  of the area for the  $5 \times 5$  mm<sup>2</sup> devices and  $\sim 10\%$  for the  $3 \times 3$  mm<sup>2</sup> devices. Table 5.5 shows the corrected  $J_{sc}$  values for the three sizes of device, by considering the area covered by the contacts, which show that the  $J_{sc}$  values have remained approximately constant throughout the scaling up process.

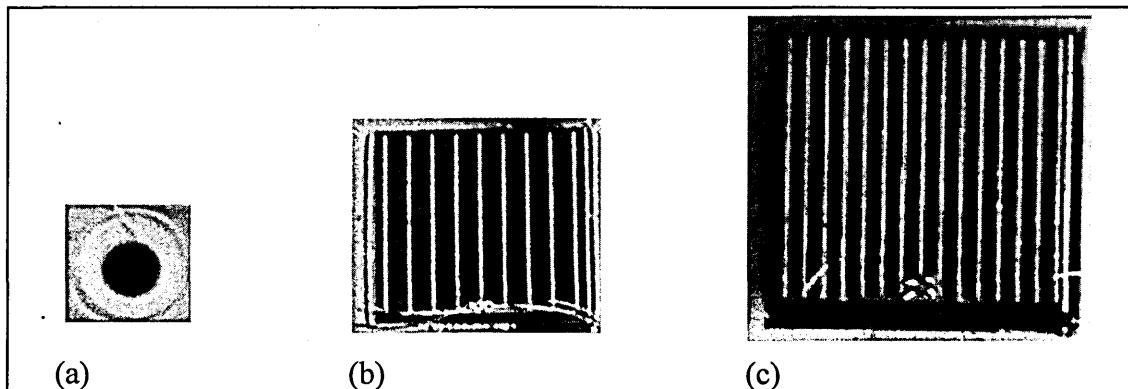


**Figure 5.17.** Photograph of cells (not to scale) showing scaling up process; (a) 0.5 mm diameter, (b)  $3 \times 3$  mm<sup>2</sup> and (c)  $5 \times 5$  mm<sup>2</sup>.

**Table 5.5.** Corrected area of the cells and calculated accurate  $J_{sc}$  values and efficiencies.

0.5 mm dia. solar cells (Effective area = 0.002 cm <sup>2</sup> )		3×3 mm <sup>2</sup> solar cells (Effective area = 0.081 cm <sup>2</sup> )		5×5 mm <sup>2</sup> solar cells (Effective area = 0.186 cm <sup>2</sup> )	
$J_{sc}$ (mA cm <sup>-2</sup> )	$\eta\%$	$J_{sc}$ (mA cm <sup>-2</sup> )	$\eta\%$	$J_{sc}$ (mA cm <sup>-2</sup> )	$\eta\%$
12.3	11.0	11.9	11.7	11.7	11.1
12.3	10.8	11.4	11.2	11.7	11.2
13.3	12.1	12.8	12.7	12.5	11.8
12.9	11.6	11.1	13.9	12.0	10.5
13.0	11.1	13.4	13.1	---	---

Since the loss of current density is probably due to the GaAs capping layer, the most plausible way to increase  $J_{sc}$  is to use another more suitable material for the capping layer; a wide bandgap, p-type semiconductor, for example GaAlP, which was the

material used for a new set of cells. The results for these devices are given in the next section.

### 5.7 Second growth of $Al_xGa_{(1-x)}As/GaAs$ devices.

A new set of devices was made again at the III-V semiconductor centre at the University of Sheffield, using a GaAlP cap instead of GaAs; two different size devices were processed (3×3 and 5×5 mm<sup>2</sup>). Both sizes of devices gave similar values, figure 5.18 and figure 5.19 show typical I-V and QE curves respectively for a 5×5 mm<sup>2</sup> device.  $V_{oc}$  and FF have remained the same, but there has been an increase in current density, from ~ 12 mA cm<sup>-2</sup> to 14 mA cm<sup>-2</sup> this is due to the GaAlP cap. It can be seen from the QE curve that there are now fewer losses in the blue part of the spectrum, as would be expected.

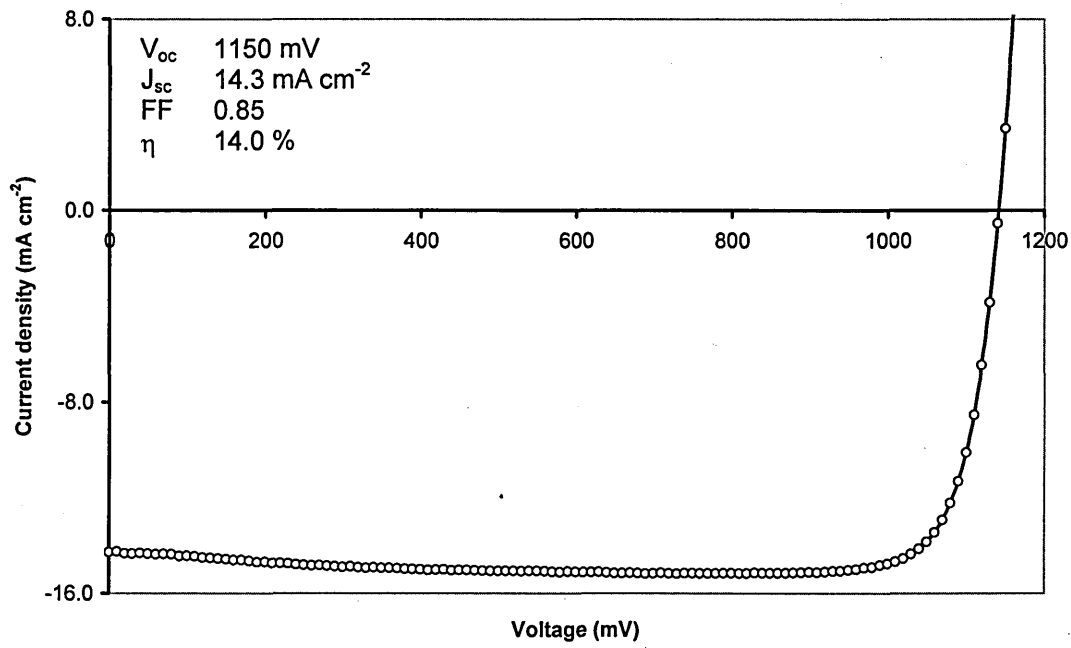


**Figure 5.18.** Typical I-V curve for (3×3 mm<sup>2</sup>) diameter solar cell, note improvement in  $J_{sc}$ .

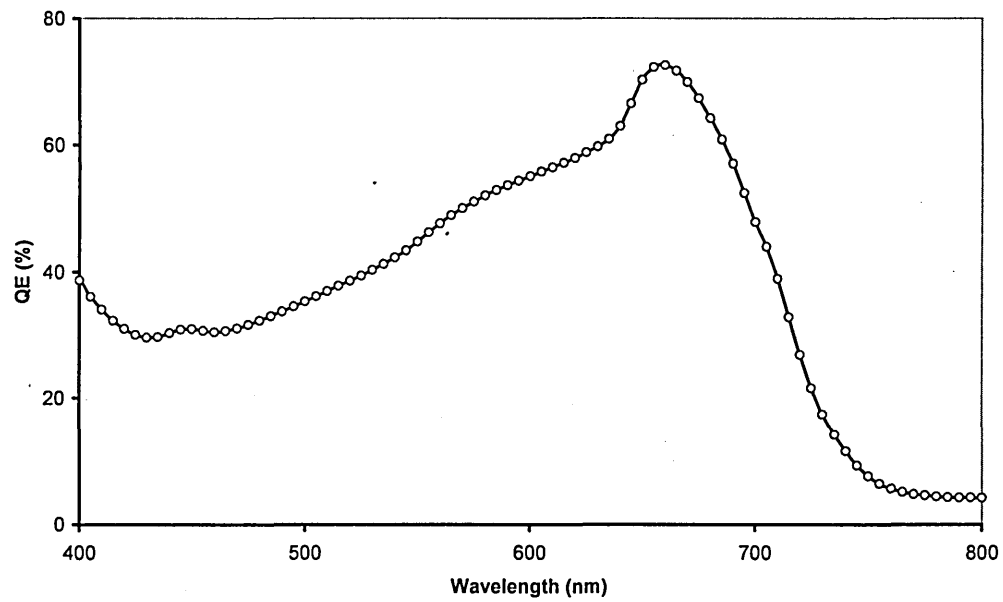


**Figure 5.19.** Typical QE curve for (3×3 mm<sup>2</sup>) diameter solar cell, note improvement in collection at blue end of spectrum.

## 5.8 Summary

This systematic set of results, gradually scaling up the size of device, show that the new device structures produce large open circuit voltages, exceeding highest values to date reported in the literature, 1022 mV [4] and 1047 mV [126], for the  $\text{Al}_x\text{Ga}_{(1-x)}\text{As}/\text{GaAs}$  system. The low current density was attributed to the presence of the GaAs capping layer, which acts as a filter at the front of the device. Attempts were made to remove the cap, which did increase the current density by a small amount. To improve the devices further a second set of devices were made, replacing the GaAs with a wider band gap GaAlP cap. This improved the photo response and hence the current density as expected, however there seems to be another reason for low current densities. Further work is necessary to explore this device structure and improve  $J_{sc}$  to the highest possible values.

## Chapter 6: Characterisation of FTO and CdS

### 6.1 Fluorine doped Tin Oxide (FTO)

Thin film solar cells require a transparent conducting layer to make a front contact to the device. Tin Oxide ( $\text{SnO}_2$ ) is a widely used contact and the one used in this work.  $\text{SnO}_2$  is a wide bandgap (3.5 eV), n-type semiconductor and is often doped with fluorine (FTO) to increase the conductivity, as the resistance of the layer contributes to the series resistance of the solar cell. Other than high transparency and high electrical conduction, other advantages of FTO are high chemical stability even at high temperatures and they also serve as an anti-reflective coating [127].

In this work two different types of FTO's are studied, both supplied by Pilkington Glass Plc; TEC-7 and TEC-15, the number refers to the sheet resistance of the layer measured in  $\Omega/\square$ . Ideally TEC-7 should produce a better device, as the electrical conductivity is higher. The thickness of each layer was also supplied by Pilkington as 518 nm for TEC-7 and 393 nm for TEC-15.

#### 6.1.1 XRD analysis of FTO

Figures 6.1 and 6.2 show that TEC-7 and TEC-15 have very similar X-ray diffraction patterns, both showing a polycrystalline structure. TEC-7 has slightly sharper profile, with greater intensity peaks, showing that its grains are larger and more crystalline, plus it is not as phase ordered as TEC-15. Table 6.1 and 6.2 show the respective positions, FWHM, relative intensities, atomic planes and grain size of TEC-7 and TEC-15 respectively.

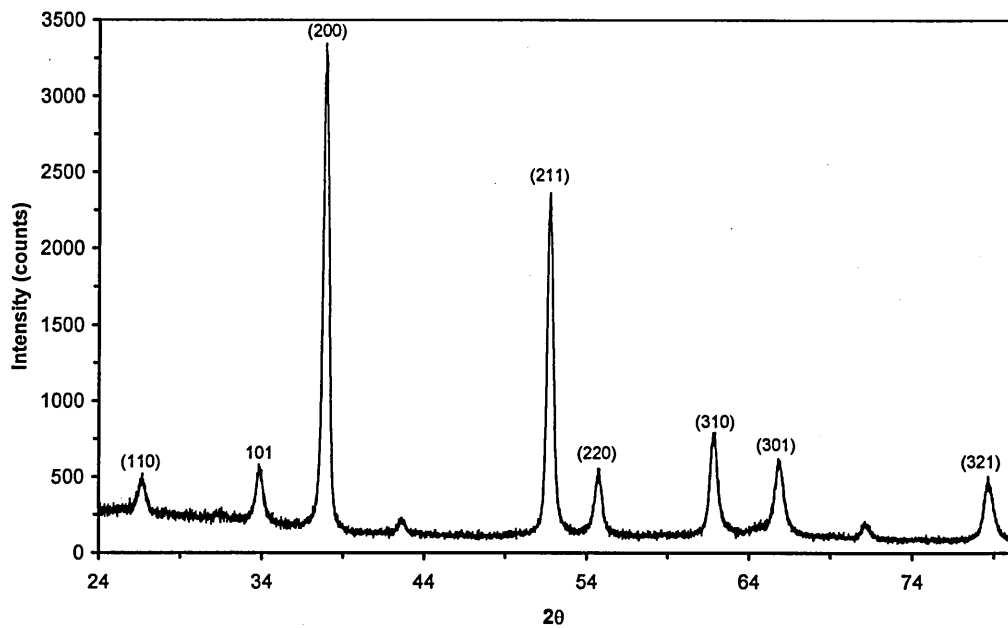


**Figure 6.1.** XRD spectra of TEC-15 FTO (393 nm thickness).

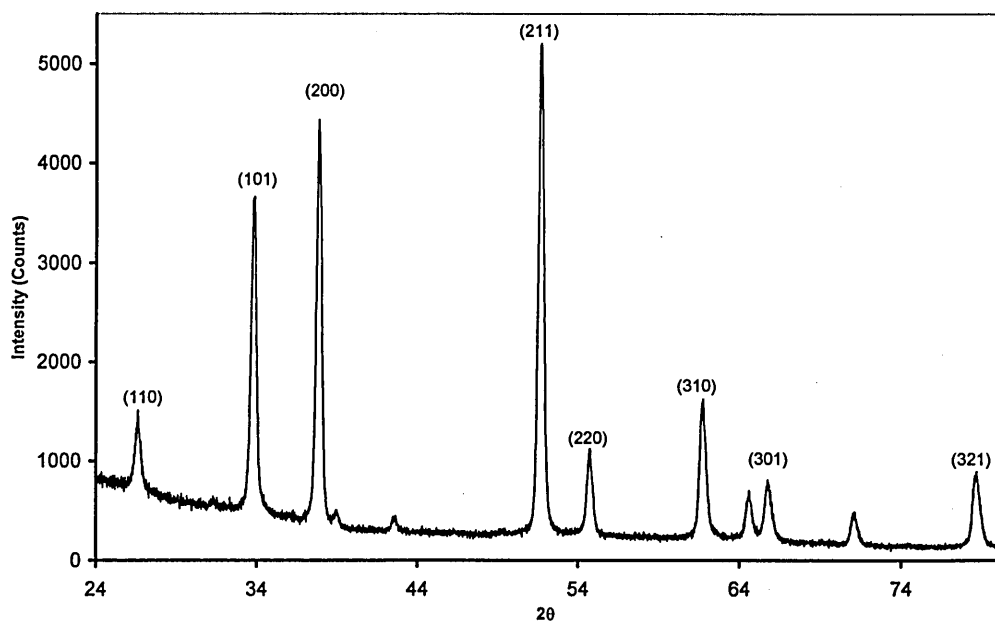


**Figure 6.2.** XRD spectra of TEC-7 FTO (518 nm thickness).

**Table 6.1.** Respective positions, relative intensities and associated atomic planes of XRD peaks observed for TEC-7 FTO.

$2\theta$ ( $^\circ$ )	d-spacing ( $\text{\AA}$ )	FWHM	Relative Intensity (%)	(hkl)	Grain size (nm)
26.62	3.35		25.4	(110)	
33.81	2.65		69.6	(101)	
37.85	2.38	0.21	84.2	(200)	42.8
51.63	1.77	0.20	100.0	(211)	44.2
54.70	1.68		18.7	(220)	
61.71	1.50		28.5	(310)	
65.83	1.42		12.4	(301)	
74.41	1.27		16.8	(321)	

**Table 6.2.** Respective positions, relative intensities and associated atomic planes of XRD peaks observed for TEC-15 FTO.

$2\theta$ ( $^\circ$ )	d-spacing ( $\text{\AA}$ )	FWHM	Relative Intensity	(hkl)	Grain Size (nm)
26.71	3.34		6.4	(110)	
33.81	2.65		10.2	(101)	
37.97	2.37	0.22	100.0	(200)	37.8
51.75	1.77	0.23	68.8	(211)	38.4
54.74	1.68		12.6	(220)	
61.72	1.50		18.4	(310)	
65.94	1.42		13.0	(301)	
74.00	1.33		2.9	(321)	

Using the Scherrer equation to calculate the grain size and taking the average calculated from the (211) and (200) peaks, TEC-7 has a grain size of 43.5 nm and TEC-15 has a grain size of 38.1 nm.

### 6.1.2 SEM of TEC-7

The SEM picture of TEC-7, figure 6.3, shows that the surface morphology of the FTO is dense, compact and nanocrystalline. The SEM of TEC-15 was very similar.

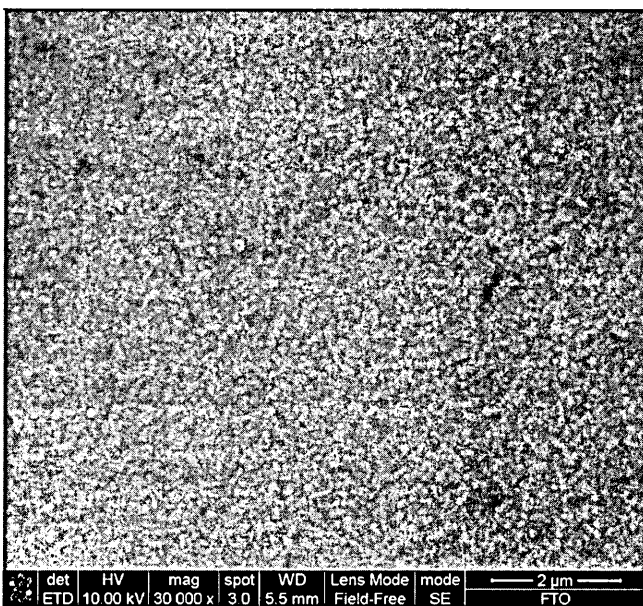


**Figure 6.3.** SEM picture of TEC-7, showing surface morphology to be nanocrystalline.

### 6.1.3 AFM of TEC-7 and 15

It was difficult to reveal any morphological differences using SEM, therefore AFM analysis was also carried out. Figure 6.4 shows 3-dimensional AFM pictures of the two types of FTO, both show typical nanocrystalline grain morphology, with uniform void free growth. The difference between TEC-7 and 15 is that the TEC-15 layers are formed of very small sharp grains with an approximate size of 100 nm with a mean surface roughness of 8.1 nm. The grains of TEC-7 layers are larger and not as sharp, having an approximate size of 200 nm with a mean surface roughness of 20.5 nm.

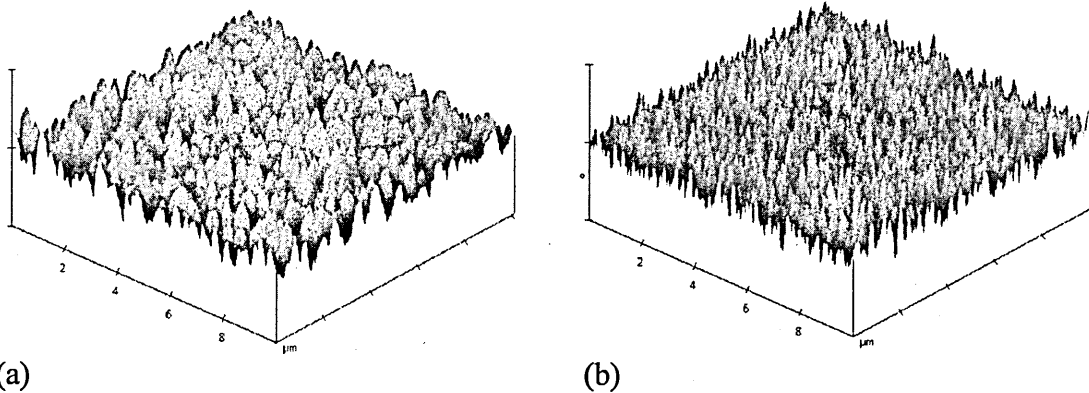


**Figure 6.4.** 3-dimensional AFM pictures of FTO: (a) TEC-7 and (b) TEC-15.

### 6.1.3 Optical absorption

In order to determine the bandgap of the FTO, optical absorption studies were carried out using a Ati-Unicam UV-Vis2 spectrometer. Figure 6.5a and 6.5b show the absorption curves for TEC-7 and 15 respectively. From these the bandgap of both TEC-7 and TEC-15 was found to be 3.75 eV.

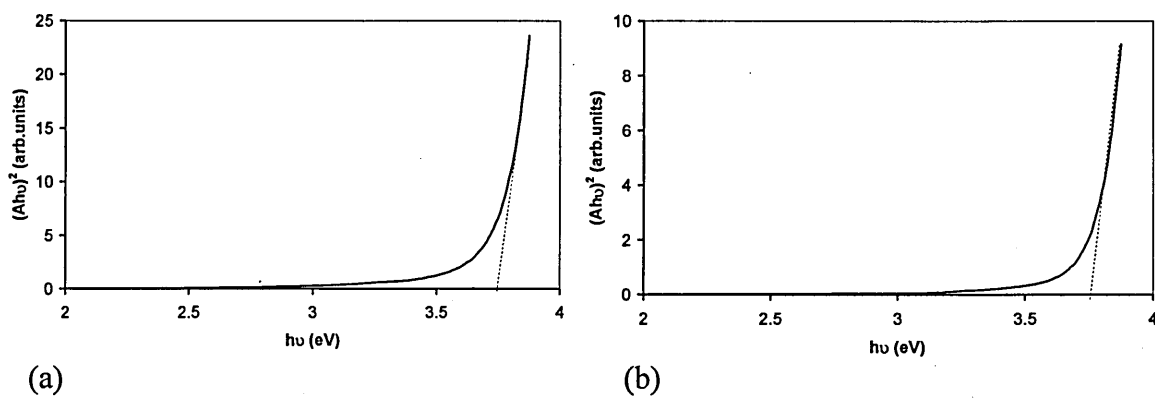


**Figure 6.5.** Optical absorption curves for (a) TEC-7 and (b) TEC-15, FTO layers.

### 6.1.4 Four point probe measurements

Four point probe measurements were carried out on the TEC-7 & 15 samples to confirm the sheet resistance values. From figure 6.6 sheet resistance of TEC-7 =  $7.1 \Omega/\square$  and TEC-15 =  $13.7 \Omega/\square$ .

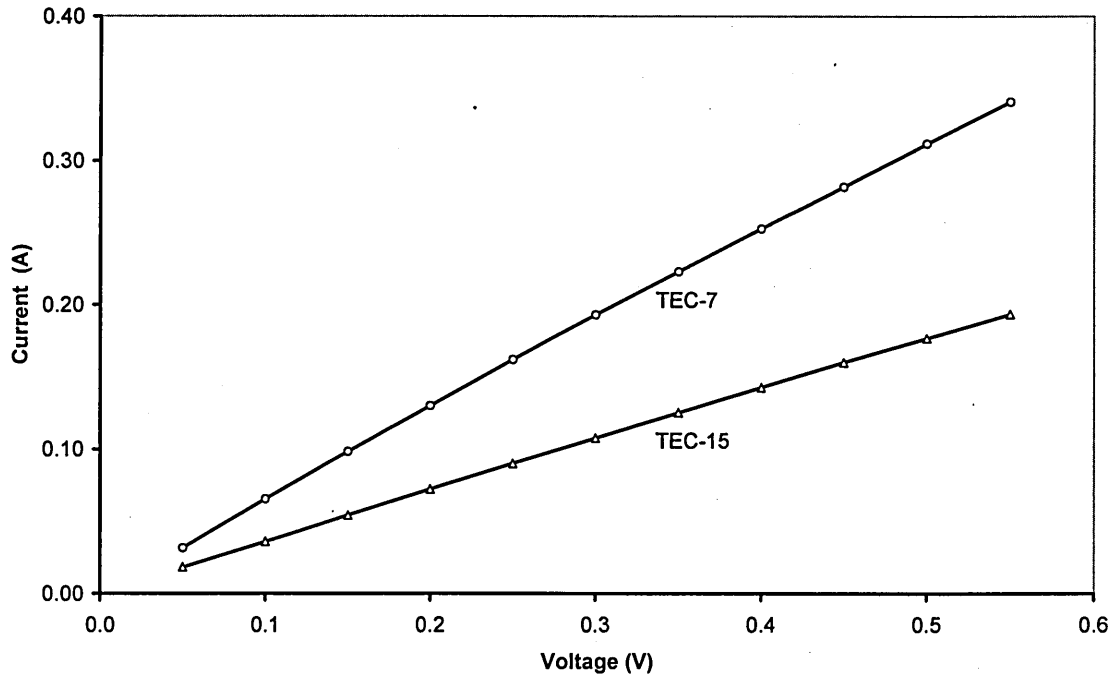


Figure 6.6. Four point probe measurements for TEC-7 and TEC-15.

## 6.2 Cadmium Sulphide (CdS) growth and characterisation

### 6.2.1 Introduction

The deposition of CdS was carried out by chemical bath deposition (CBD) [68], which as outlined in chapter 2.4.1 and has many advantages over other deposition techniques. The bath contained 0.015 M cadmium sulphate ( $\text{CdSO}_4$ ), 1.5 M thiourea  $\text{CS}(\text{NH}_2)_2$  and 1.5 M ammonium hydroxide. All chemicals were at least 5N purity, supplied by Aldrich and were used as received. CdS films are deposited by the decomposition of the thiourea (the sulphur source) in an alkaline solution (ammonium hydroxide) of cadmium salts (the Cd source).

### 6.2.2 Experimental

A bath containing de-ionised  $\text{H}_2\text{O}$  and the dissolved  $\text{CdSO}_4$  was heated to  $\sim 60^\circ\text{C}$ , with constant stirring. At this point the substrate (FTO or FTO/CIS), thiourea and the ammonium hydroxide were added, after the addition of these the pH was  $\sim 11$ . The bath was then heated to  $75^\circ\text{C}$ , at which point the reaction starts to take place (nucleation). The film was grown for 8 minutes or stopped when colloids started to form. Colloid formation needs to be avoided as they disrupt the surface of the layer. The films were then washed in de-ionised water and dried with flowing  $\text{N}_2$  gas, before annealing in air at  $450^\circ\text{C}$  for 20 minutes. To check for uniformity during the deposition process CdS was also deposited on large area ( $10 \times 10 \text{ cm}^2$ ) substrates.

From the large plate, 1 cm wide strips were cut off to study the film uniformity, with its position in the bath. The samples were numbered from 1 to 10, 1 being the top of the plate and 10 being the bottom.

### 6.2.3 XRD analysis of CdS

XRD of as-deposited and annealed CdS was carried out at four equal distance positions along the length of the plate, all samples showed similar patterns, indicating the material is uniform and there is little difference in intensity between the as-deposited and

annealed samples, the CdS has a cubic structure, which is as expected for CBD CdS. Figure 6.7 shows XRD spectra of a CdS sample taken at 5 cm along the plate, both as-deposited and annealed are very similar. The spectrum is dominated by a sharp intense peak at  $2\theta = 26.60^\circ$  which relates to the diffraction plane (111). There are also 2 smaller peaks relating to the (220) and (222) planes. The small peaks to the left of the (111) peak is probably due to elemental sulphur and the small peak to right has been identified as CdO. Table 6.3 shows the respective positions, atomic spacing, relative intensities and atomic planes of cubic CdS. The crystallite size for the annealed sample was calculated to be 25.1 nm, using the Scherrer equation.

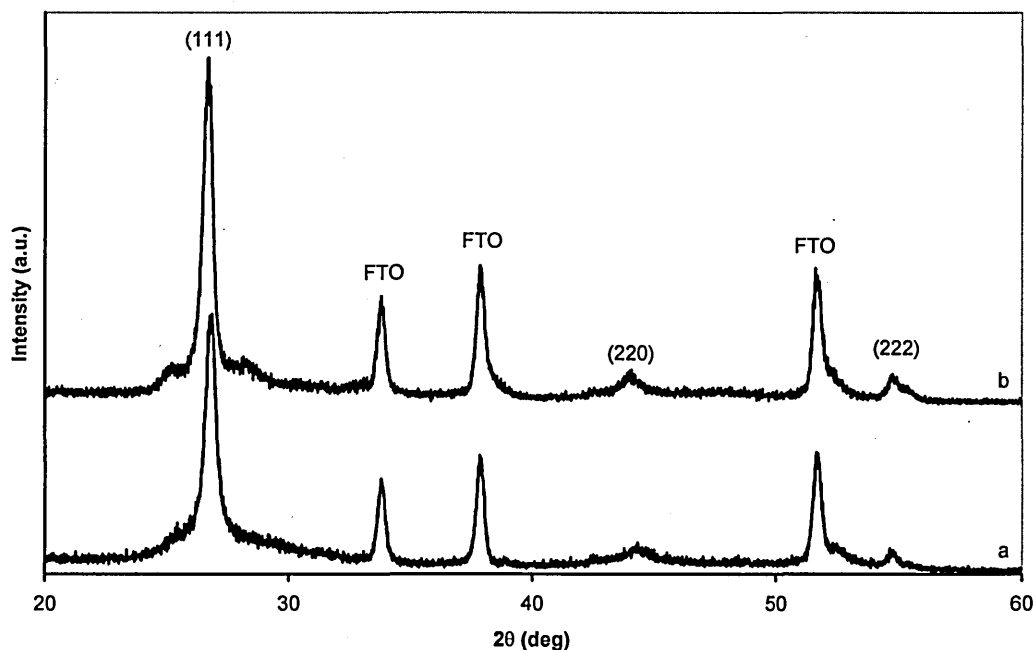


**Figure 6.7.** XRD spectra of CBD CdS; (a) as-deposited and (b) annealed at 450°C for 20 minutes in air.

**Table 6.3.** Respective positions, atomic spacing, relative intensities and atomic planes of cubic CdS.

$2\theta$ ( $^\circ$ )	d-spacing ( $\text{\AA}$ )	Relative Intensity (%)	(hkl)
26.50	3.36	100.0	(111)
30.70	2.91	23.2	(200)
43.97	2.06	52.0	(220)
52.07	1.75	39.0	(311)
54.58	1.68	5.4	(222)
63.93	1.46	7.2	(400)

#### 6.2.4 Thickness measurements

The thicknesses of the annealed CdS layers were measured using a Talyor Hobson Talysurf. Figure 6.8 shows the variation in thickness along the length of the plate. As can be seen from the plots the thickness is very uniform at ~45 nm, with a slight thinning off near to the bottom of the plate. This is due to the layer being disturbed during deposition by the magnetic stirrer.

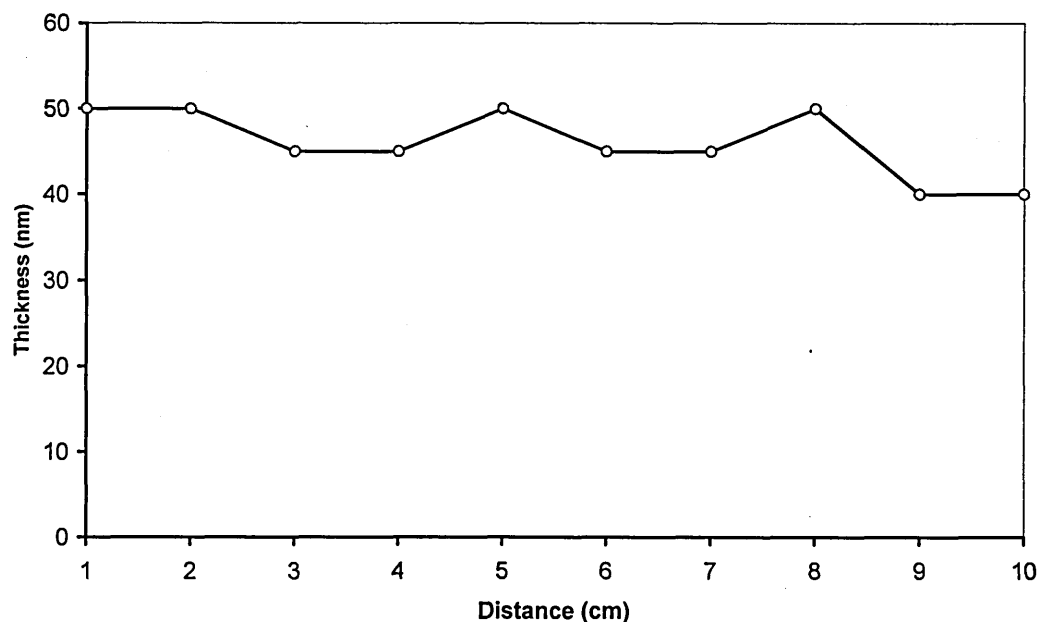
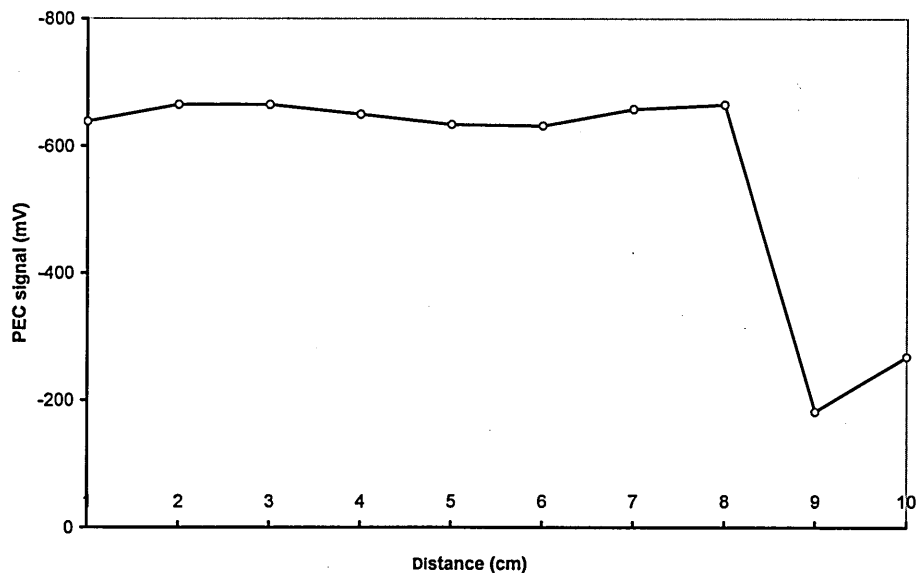


Figure 6.8. Graph of CdS thickness over length of plate.

#### 6.2.5 Photoelectrochemical measurements (PEC)

Photoelectrochemical measurements were carried out to determine the electrical conductivity type of the annealed CdS layer. The electrolyte used was a 0.1 M KCl aqueous solution. PEC measurements were taken on samples cut at every 1 cm along the length of the ( $10 \times 10 \text{ cm}^2$ ) CdS plate, figure 6.9 shows all samples have a negative PEC voltage indicating the material is n-type.



**Figure 6.9.** Graph showing PEC signals along the length of the CdS plate.

As with the thickness, figure 6.9 shows that the PEC signal is very constant over the majority of the length and decreases near to the bottom of the sample, again this is also probably due to the layer being disturbed during deposition by the magnetic stirrer.

### 6.2.6 Optical absorption

In order to determine the bandgap of the as-deposited and annealed CdS layers optical absorption studies were carried out using a UV-visible spectrometer. Figure 6.10 shows typical absorption curves for CdS, (a) as-deposited and (b) annealed.

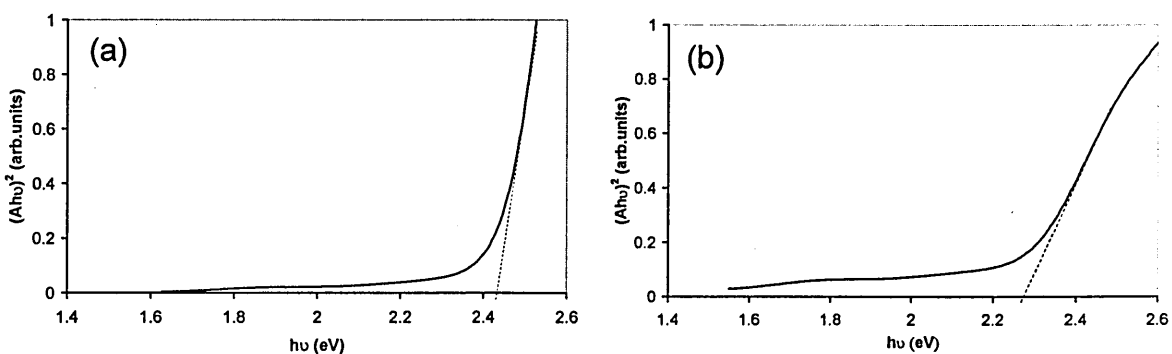


**Figure 6.10.** Absorption curves of typical CdS samples, (a) as-deposited giving a bandgap of 2.42 eV and (b) annealed giving a bandgap of 2.28 eV.

Figure 6.10(a) shows the bandgap of as-deposited CdS to be 2.42 eV, this is in agreement to the reported value which is the same [68]. After annealing in air at 450°C for 20 minutes, the bandgap reduces to 2.28 eV, this reduction in bandgap after heat treatment has been reported by numerous groups. Soubane et al [128] explain this reduction by the formation of a thin layer of CdO on the surface. This result also concurs with visible evidence; the as-deposited films are yellow in colour, whereas after annealing the colour changes to dark orange, which is closer to the colour of CdO [129].

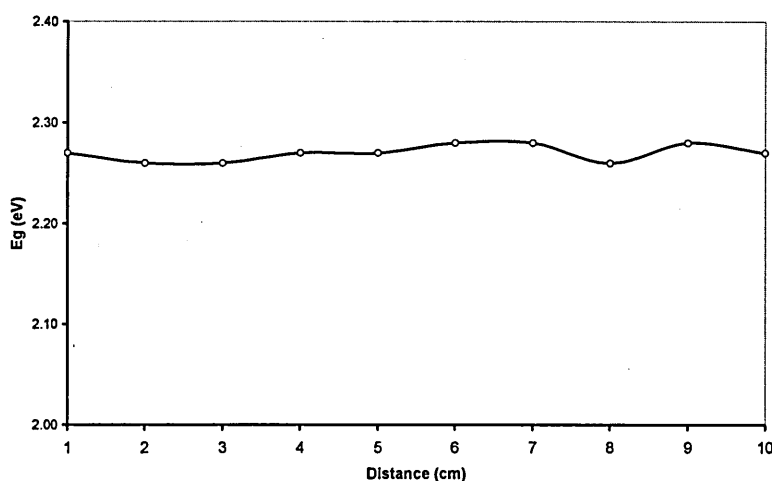


**Figure 6.11.** Graph of bandgap for annealed CdS along the length of the plate.

The bandgap for annealed CdS is very similar along the length of the plate, as shown in figure 6.11, which gives an average bandgap of 2.28 eV.

### 6.2.7 SEM analysis

The surface morphology of the CdS films was studied by SEM, figure 6.12 (a) and (b) shows SEM pictures of both as-deposited and annealed samples. The as-deposited sample has grain sizes ~250 nm and the annealed sample ~400 nm, these values are much larger than those estimated from the XRD spectra using the Scherrer equation. This is probably because the SEM hasn't resolved the image clearly and is not showing the individual grains, but agglomerates of crystallites.

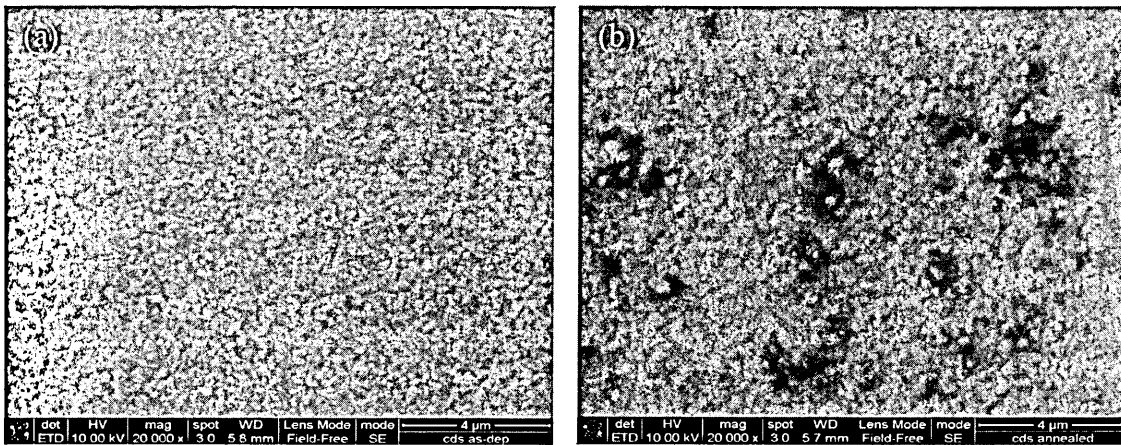


**Figure 6.12.** SEM of CdS layers: (a) as-deposited and (b) annealed at 450°C for 20 minutes in air.

### 6.3 Summary

In this chapter it was shown that both types of transparent conducting oxide layers TEC-7 and TEC-15 have a polycrystalline structure, and both have a bandgap equal to 3.75 eV. The electrical conductivity of the TEC-7 material is higher, which was to be expected, as the number refers to the sheet resistance of the layer. Both materials act as good substrates, suitable for the electrodeposition of CIGS layers.

It was also shown that CBD CdS, produced good quality, uniform layers. The crystalline structure of both the as-deposited and annealed layers were similar, with the XRD spectra being dominated by a large peak, relating to the (111) atomic plane of the cubic structure. The thickness of the CdS layer was very uniform, for many samples taken from the length of large plate, equal to ~50 nm. The electrical conductivity was n-type, with a band gap of 2.28 eV.

## Chapter 7: Development of CuInGaSe<sub>2</sub> superstrate devices

### 7.0 Introduction

The device structure usually consists of glass/Mo/CIGS/CdS/i-ZnO/Al-ZnO/metal-grid, and the photovoltaic junction is considered to form between the n-CdS and p-CIGS layers. The above structure is usually fabricated starting from the back metal contact, which is molybdenum, and utilising three or four different growth techniques such as magnetron sputtering, electrodeposition, chemical bath deposition and vacuum sputtering. The combination of several growth techniques makes the industrial production process potentially expensive.

This research programme has attempted to address this issue using a superstrate configuration which Nakada et al have achieved efficiencies of 12.8% [49]. The growth techniques have been limited to low-cost chemical bath deposition (CBD) and electrodeposition (ED) methods. ED has been successfully used to grow chalcopyrite semiconductors by Lincot et al with efficiencies of 11.3% [44].

The CIGS material has been grown to produce layers with p<sup>+</sup>, p, i, n, and n<sup>+</sup> type electrical conduction [23,130]. Using new ideas emanating from the 'new model' proposed for CdS/CdTe solar cells [122], the Sheffield Hallam Group have designed new PV device structures based on CIGS, starting from the front electrical contact instead of the conventional method of fabricating from the back metal contact (Mo). This chapter looks at how the bath concentration and deposition voltage affects the resulting CIGS films and some initial results on n-n-i-p type glass/TCO/n-CdS/n-CIGS/i-CIGS/p-CIGS/metal solar cell structures as the first step towards development of graded bandgap multilayer thin film solar cells.

### 7.1 Electrodeposition of CuInGaSe<sub>2</sub>

Electrodeposition of the CIGS layers was carried out using the standard 3-electrode system. The anode was a high purity graphite plate, the reference electrode was Ag/AgCl and the cathode or the working electrode was a glass/FTO (TEC-7) for characterisation and glass/FTO /n-CdS for fabrication of devices. The n-CdS for use in

devices was deposited using the standard chemical bath technique, and heat treated in air at  $\sim 450^\circ\text{C}$  for  $\sim 20$  minutes as described in chapter 6.2.2. For the CIGS for comparison, three different electrolytic concentrations were used, all from an aqueous medium. All chemicals were at least 5N purity, supplied by Aldrich and were used as received.

**Table 7.1.** Concentrations used in 3 different electrolytes.

Bath	Concentration mM				
	CuSO <sub>4</sub>	In <sub>2</sub> (SO <sub>4</sub> ) <sub>3</sub>	Ga <sub>2</sub> (SO <sub>4</sub> ) <sub>3</sub>	H <sub>2</sub> SeO <sub>3</sub>	Buffer
A	2.00	4.00	8.00	4.00	NO
B	2.56	2.40	5.70	4.47	NO
C	2.56	2.40	5.70	4.47	YES

The buffer solution used was a pH 3 Hydrion buffer, a mixture of Potassium Hydrogen Phthalate and Sulphamic Acid [131,132]. The material layers were deposited at room temperature with pH $\sim$ 2.5 and without stirring. A series of about 30 small samples ( $5\times 10\text{ mm}^2$ ) were grown at different potentials in order to determine the electrical conduction type and stoichiometry using PEC and XRF respectively. For characterisation purposes films were grown for  $\sim 20$  minutes and for devices between 30 and 60 minutes, depending on the deposition voltage.

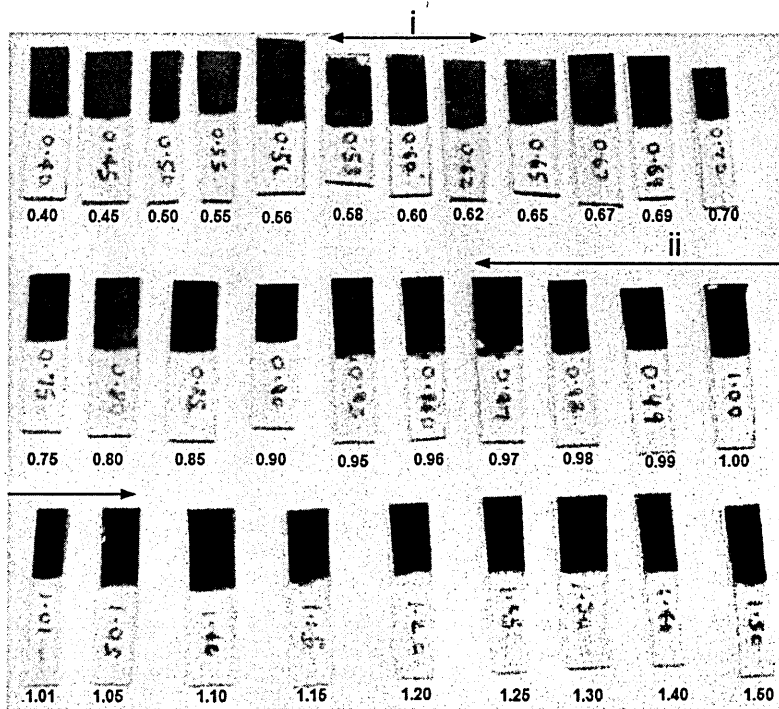


**Figure 7.1.** Typical set of samples grown from bath C, as a function of growth voltage.

Figure 7.1 shows a photograph of a typical sample set grown from bath C in this case; note the peeling in the voltage ranges -0.58 to -0.62 V (i) and -0.97 to -1.05 V (ii).

### 7.1.1 Linear sweep voltammetry (LSV) and PEC of bath C

The voltamogram shown in figure 7.2 indicates that the deposition of  $\text{Cu}_x\text{Se}$  starts at -0.10 V. A plateau current is reached at  $\sim -0.35$  V, this is related to the co-deposition of Cu, In and Se. The inset shows a small hump in the voltamogram with a peak at -0.70 V, this shows an increase in copper or selenium, or both. The increase in current at -0.85 V is an increase in indium. A rapid increase in current at  $\sim 1.0$  V is hydrogen evolution at the cathode. The shaded area shows the deposition range where the layer peels off. The dotted line of the PEC signal shows the projected PEC values if the layer had not peeled off and had remained intact.

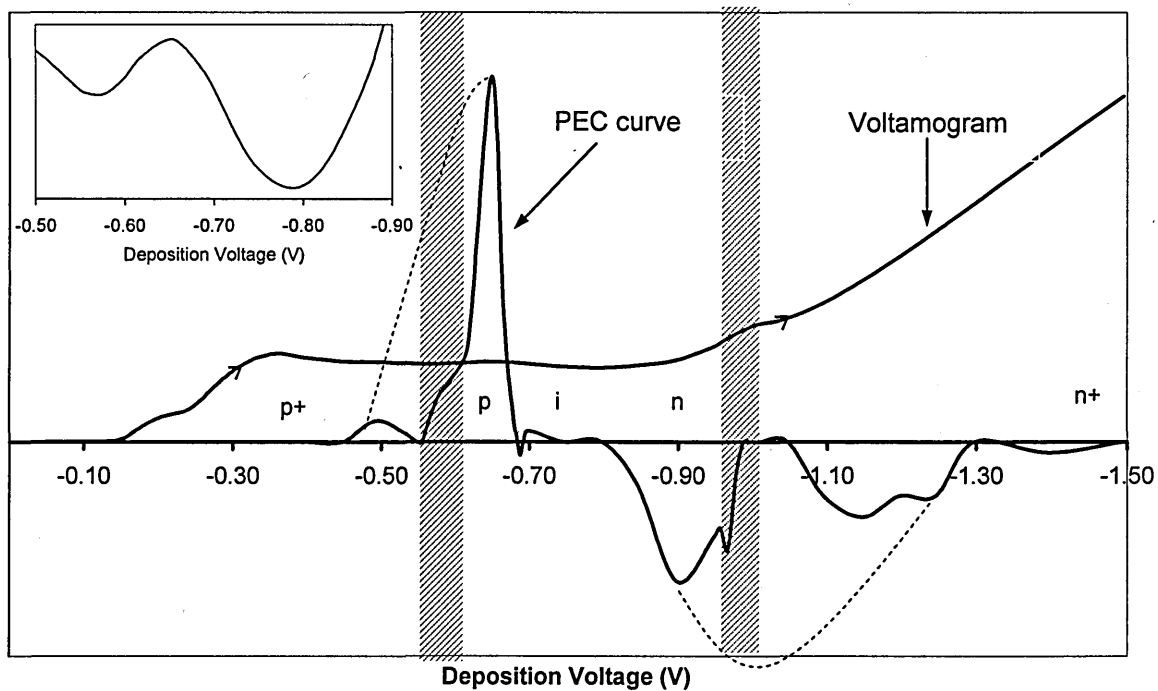


**Figure 7.2.** Voltamogram, PEC results and peeling off regions (shaded area) observed for bath C, inset; expansion of voltamogram from -0.50 to -0.90 V.

## 7.2 PEC (Photoelectrochemical cell) analysis

In order to establish conductivity type as a function of deposition voltage, PEC was carried out and to establish whether bath concentration changed the results, two different concentrations A and C are studied.

A typical set of values obtained for a series of samples grown from two baths (A and C) are shown in figure 7.3, both baths show similar trends, the shaded area is where the film peels off. This same trend was seen for numerous sets of sample. The samples were annealed in air at 350°C for 10 mins. The polarity of the PEC signal determines the electrical conductivity of the layer, and the magnitude of the signal indicates the suitability of doping concentration of the semiconducting layer for fabricating electronic devices.

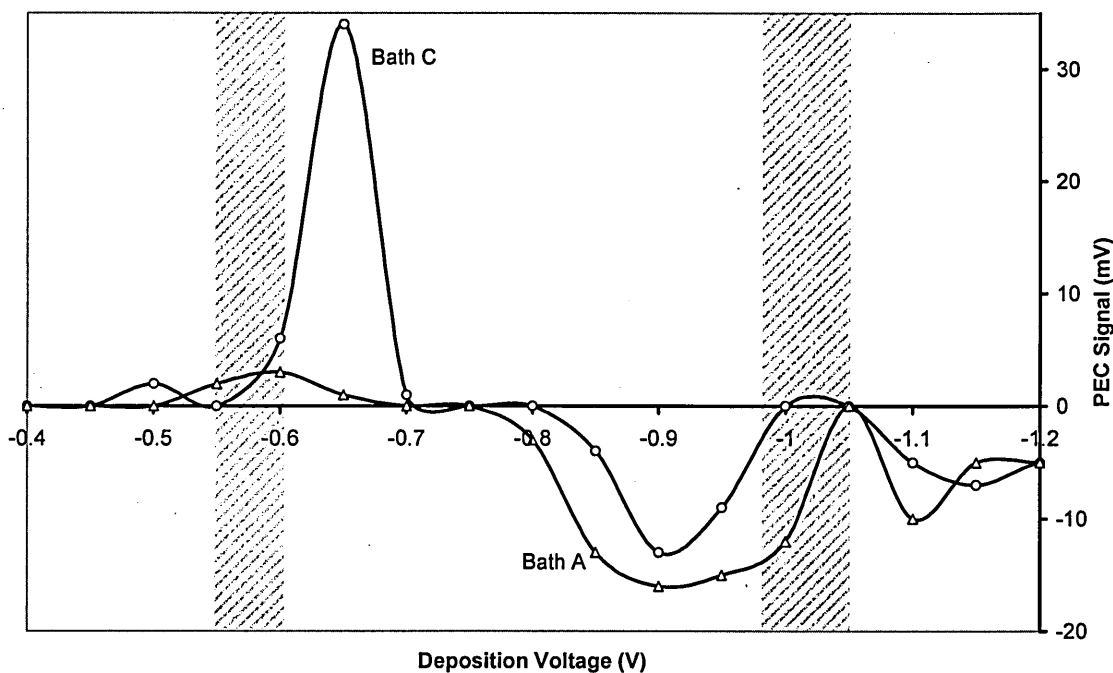


**Figure 7.3.** PEC results and peeling off regions observed for baths A & C.

According to the information presented in figure 7.3,  $p^+$ -CIGS is deposited at a cathodic potential more positive than -0.45 V; p-CIGS in the range  $\sim -0.45$  to  $\sim -0.70$  V (with a maximum at -0.60 V and -0.65 V for bath A and C respectively, which corresponds to an increase in current on the voltamogram figure 7.2 inset, at the same potential); intrinsic-CIGS between  $\sim -0.70$  to  $\sim -0.80$  V; n-CIGS between  $\sim -0.80$  to  $\sim -1.30$  V (with a

maximum at -0.90 V for both baths A and C, again this corresponds to an increase in current on the voltamogram at the same potential) and  $n^+$ -CIGS above -1.30 V. This trend is observed for both baths A and C.

Figure 7.4 shows how a typical PEC signal relates to possible examples of doping concentrations; the shaded areas indicate the areas where the doping concentration is ideal for a good PV active device.

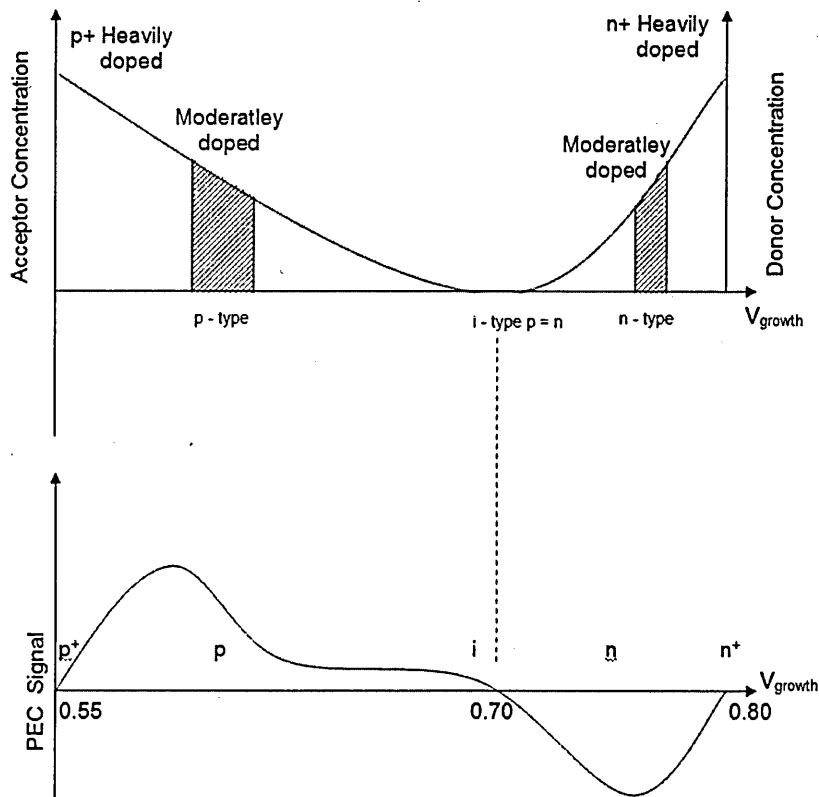


**Figure 7.4.** The relationship between PEC signal and possible doping concentration values.

Once these voltage values are established, any desirable semiconducting layer could be grown from this particular bath. In this preliminary work, n-i-p diodes were grown from bath C on glass/FTO/n-CdS substrates at -0.80, -0.75 and -0.65 V respectively avoiding peeling off voltages followed by chemical etching and metallisation.

This n-i-p trend has also been found by NASA [133], who found the material was p-type for deposition potentials 1.0 to 1.1 V (vs SCE electrode) and n-type for potentials 1.2 to 1.4 V. They also observed that the Cu/In ratio decreases as the deposition potential increases.

### 7.3 XRD analysis

XRD studies were carried out to identify the crystallinity, composition and phases of the deposited CIGS thin films. A Philips Expert X-ray diffraction system fitted with a  $\text{CuK}\alpha 1$  anode was used, operating with a glancing angle of  $0.5^\circ$ . Whatever the bath concentrations and whether the films were annealed or not, 3 diffraction peaks associated with the chalcopyrite phase are identified. Table 7.2 shows how the  $2\theta$  values increase with the addition of gallium. Table 7.2(a) shows the three main peaks for  $\text{CuInSe}_2$ , Table 7.2(b) for  $\text{CuGaSe}_2$  and Table 7.3(c) shows there is a gradual shift in the position of the (112) peak as the gallium content is increased in  $\text{CuInSe}_2$  to form  $\text{CuGaSe}_2$ . As gallium is added to  $\text{CuInSe}_2$ , the peak shifts to higher  $2\theta$  indicating a decreased 'd' spacing. This is to be expected as gallium is a smaller atom than indium.

**Table 7.2.** Summary of JCPDF data sheets showing effect of increasing gallium content, (a) main peaks for  $\text{CuInSe}_2$ , (b) main peaks for  $\text{CuGaSe}_2$  and (c) gradual increase in  $2\theta$  for (112) peak as gallium is increased.

(a)				(b)			
$\text{CuInSe}_2$				$\text{CuGaSe}_2$			
$2\theta(\text{deg})$	$d(\text{\AA})$	Int%	(hkl)	$2\theta(\text{deg})$	$d(\text{\AA})$	Int%	(hkl)
26.650	3.342	100	(112)	27.724	3.215	100	(112)
44.184	2.048	41	(204)	45.732	1.982	20	(220)
44.261	2.044	40	(220)	46.227	1.962	39	(204)
52.262	1.749	12	(116)	54.322	1.667	21	(312)
52.433	1.744	25	(312)	55.195	1.663	10	(116)

(c)		
Compound	$2\theta$ for (112)	$d(\text{\AA})$
$\text{CuInSe}_2$	26.650	3.342
$\text{CuGa}_{0.3}\text{In}_{0.7}\text{Se}_2$	26.919	3.312
$\text{CuGa}_{0.5}\text{In}_{0.5}\text{Se}_2$	27.195	3.279
$\text{CuGa}_{0.6}\text{In}_{0.4}\text{Se}_2$	27.237	3.274
$\text{CuGaSe}_2$	27.724	3.215

(Addition of sulphur has a similar effect  $\text{CuInS}_2$  (112)  $2\theta = 27.885$  and  $\text{CuGaS}_2$  (112)  $2\theta = 29.105$ ).

### 7.2.1 XRD as a function of bath concentration

Figure 7.5 shows XRD spectra for CIGS layers grown from all three baths deposited at -0.65 V. All spectra show chalcopyrite structure with major reflections from (112), (220/204) and (312/116) planes. Bath C (buffered bath) gives a better crystalline material. Material grown from baths A and B, show indium selenide phases, which can be expected from bath A since the indium concentration in the bath is nearly double that of B and C. Since the only difference in bath B and C is the buffer, bath B was not investigated in any detail.

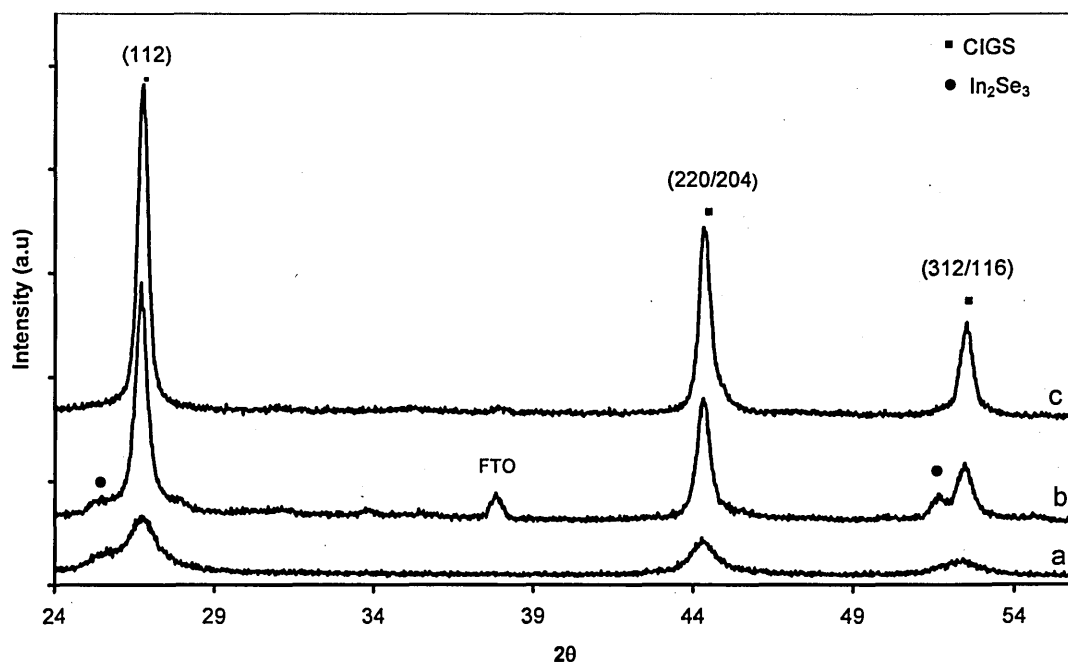
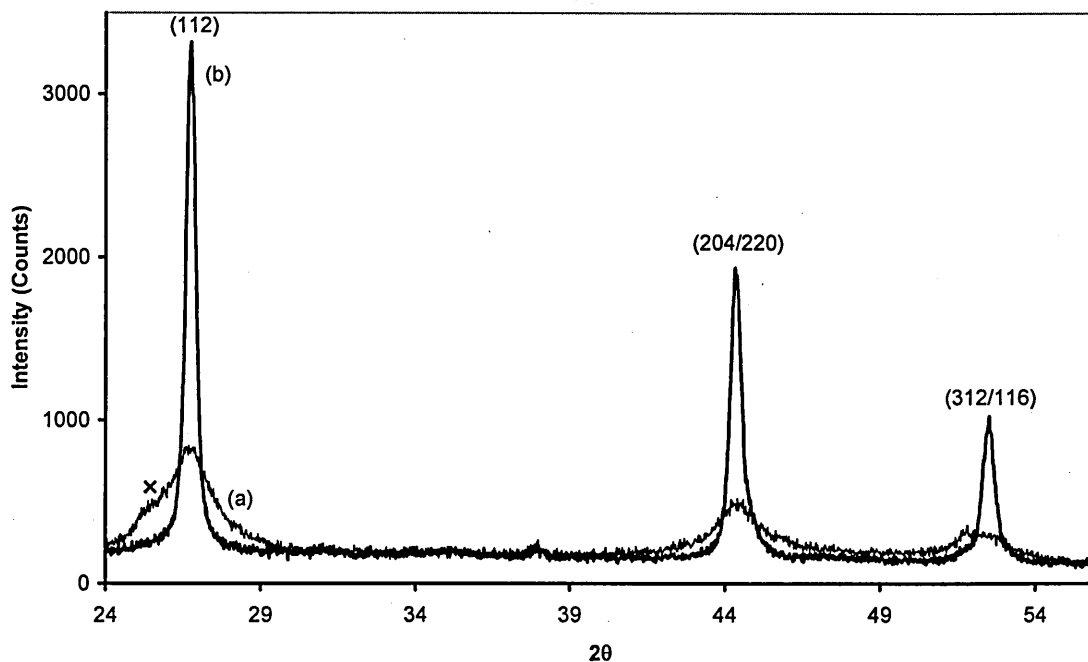


Figure 7.5. XRD spectra of CIGS grown using, (a) bath A, (b) bath B and (c) bath C.

### 7.2.2 XRD as a function of deposition voltage

Figure 7.6 shows XRD spectra for CIGS samples deposited from bath C, at -0.65 V, (a) as-deposited and (b) after annealing in air at 450°C for 20 minutes. As would be expected the peaks are much more intense and sharper after annealing, showing the material has re-crystallised.



**Figure 7.6.** XRD spectra of samples deposited from bath C, at -0.65 V; (a) as deposited and (b) annealed.

Figure 7.7 shows XRD spectra for annealed CIGS films deposited from bath C, at three different voltages; (a) -0.65 V (b) -0.75V and (c) -0.85 V, which correspond to p, i and n-type conduction from the PEC signals. All three peaks for all three samples are at the same  $2\theta$  positions; (112) at  $26.76^\circ$ , (204/220) at  $44.42^\circ$  and (116/312) at  $52.5^\circ$ . They are all just slightly greater than those of  $\text{CuInSe}_2$  (Table 7.2(a)). This suggests that no or very little gallium is being electrodeposited into the film, which is very likely as gallium has a very large negative electrode potential ( $E_0 = -0.73$  V vs Ag/AgCl reference electrode).

The small shoulder to the left of the (112)  $\text{CuInSe}_2$  peak on the as-deposited sample marked with an 'x', figure 7.6(a), has been identified as  $\text{In}_2\text{Se}_3$ . This disappears after annealing, which suggests the  $\text{In}_2\text{Se}_3$  reacts with the  $\text{CuInSe}_2$  during annealing. Also figure 7.7(b) and (c) shows that the same shoulder remains after annealing for samples deposited at voltages greater than -0.70 V, which suggests that these films are indium rich, confirming the results from the PEC signal.

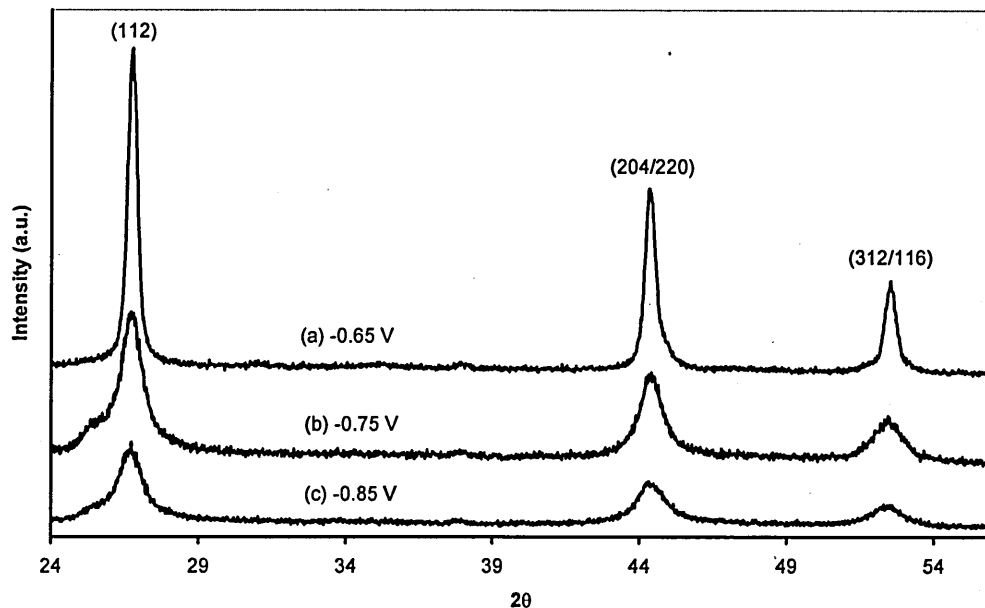


**Figure 7.7.** XRD spectra of annealed CIGS deposited at; (a) -0.65V, (b) -0.75 V and (c) -0.85 V.

Also as the deposition voltage increases, the intensity of XRD peaks decreases and peak widths broaden, this shows that the films are becoming less crystalline. This would explain why during the deposition process, the higher the voltage the more powdery and less adhered the films became. Films deposited around -0.60 V visually looked better and were well adhered with no powder. As mentioned in the previous paragraph, films deposited at more negative voltages contain more indium, and the literature reports that generally In-rich  $\text{CuInSe}_2$  is less crystalline than Cu-rich  $\text{CuInSe}_2$ , [134,131].

The crystallite sizes were calculated using the Scherrer equation, Table 7.3 shows how the crystallite size changes as a function of deposition potential, with the crystallinity decreases as the deposition voltage is increased. The strain was calculated for the -0.65 V sample using the Hull equation, figure 7.8 (this also confirms crystallite size), and shows that annealing improves crystallite size and reduces the strain in the layer.

**Table 7.3.** Grain size as a function of deposition voltage, calculated from (112) peak.

Deposition voltage (V)	Grain size (nm)	
	As-deposited	Annealed
-0.65	6.65	39.00
-0.75	4.94	15.50
-0.85	4.84	14.00

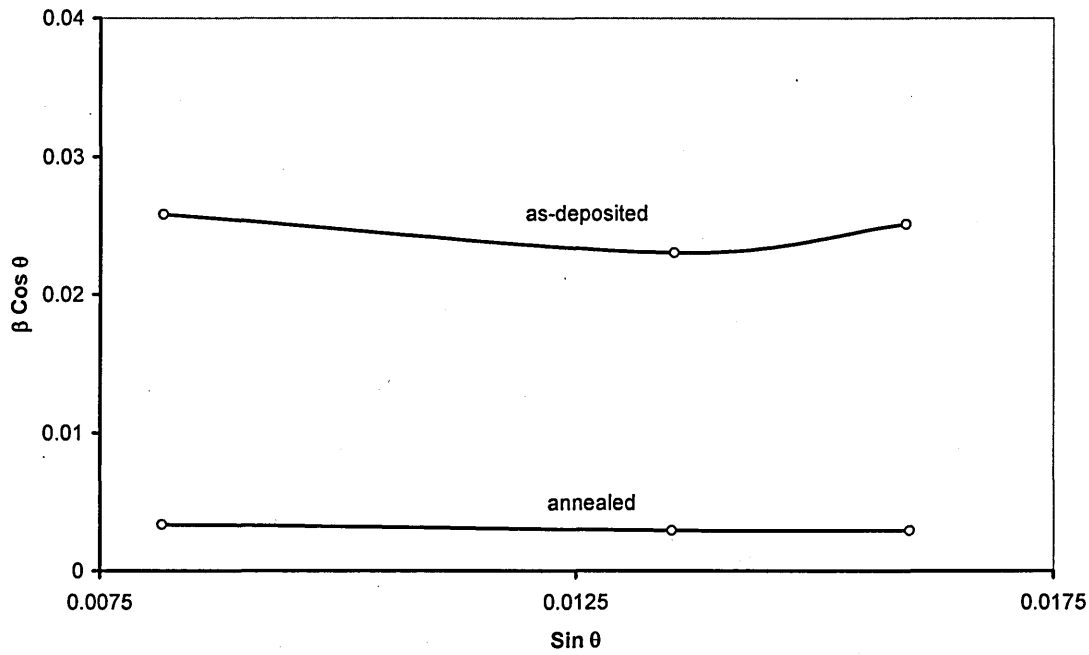


**Figure 7.8.** Graph of  $\beta \cos \theta$  vs  $\sin \theta$  for the 3 main peaks of -0.65 V sample.

From figure 7.8 the strain in the -0.65 V as-deposited sample was calculated to be  $160 \times 10^{-3}$  and the grain size 5.67 nm. The annealed sample gave a strain of  $137 \times 10^{-3}$  and a grain size of 40.5 nm. The grain size calculation concur with the ones calculated using the Scherrer equation and the strain 'relaxes' in the annealed sample, as would be expected, as any defects are 'annealed out'.

The lattice parameters were also calculated for the annealed -0.65 V sample, using the (112) and (312) peaks and equation 7.1 solving for  $a$  and  $c$  simultaneously.

$$\frac{1}{d^2} = \frac{h^2 + k^2}{a^2} + \frac{l^2}{c^2} \quad (7.1)$$

Calculated lattice parameters for the annealed -0.65 V sample;  $a = 0.5697$  nm and  $c = 1.0102$  nm. From standard data for  $\text{CuInSe}_2$ ;  $a = 0.5784$  nm and  $c = 1.0161$  nm. For  $\text{CuGaSe}_2$ ;  $a = 0.5347$  nm and  $c = 1.0474$  nm, [135]. This confirms the previous results as the lattice parameters are only very slightly less than those for  $\text{CuInSe}_2$ , showing very little gallium has been incorporated into the lattice. (Note. The lattice parameter for cubic CdS is 0.58 nm which is a very good match).

## 7.4 XRF investigation

It can be seen from figure 7.9(a) and (b) that the electrolyte composition and the deposition voltage influence the atomic percentage concentrations of Cu, In, Ga and Se deposited in the layers.

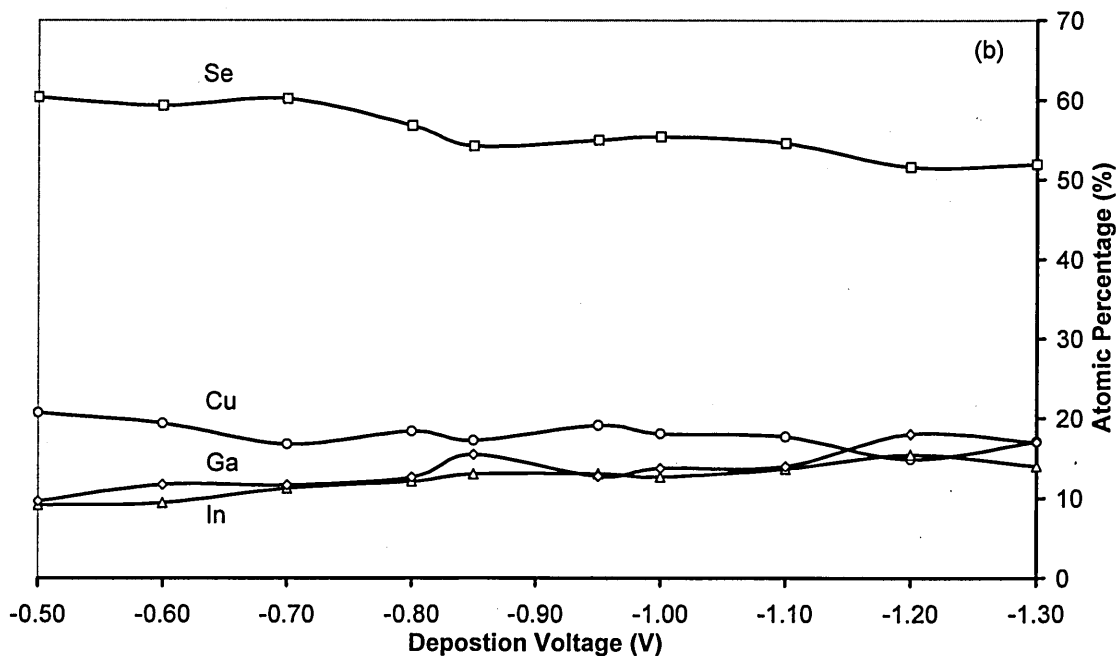
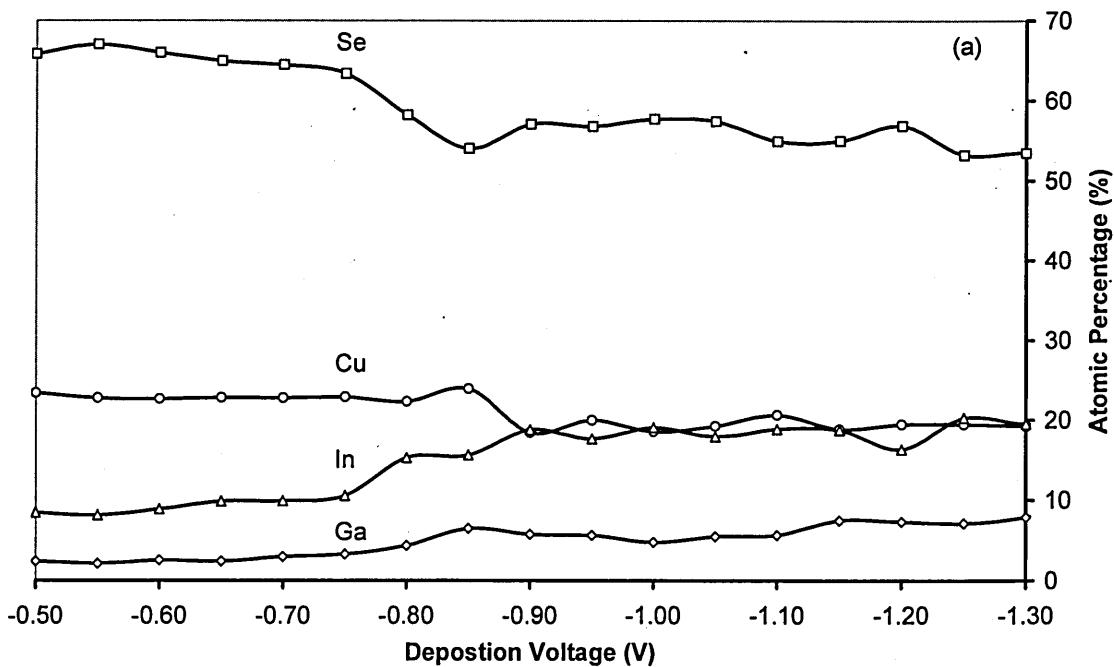


**Figure 7.9.** Atomic percentage of elements for; (a) bath A and (b) bath C, as determined by XRF as a function of deposition voltage.

#### 7.4.1 Influence of bath concentration

As would be expected, bath A which has a higher selenium concentration than that of bath C, shows that more selenium is deposited into the film, especially at low deposition voltages. According to Calixto et al, it is the ratio of copper to selenium which plays the most important factor in film quality. Films grown from baths with  $[\text{Se}^{4+}]/[\text{Cu}^{2+}] > 1.75$  were always Se rich and often exhibited cracking, a ratio equal to 1.75 produced the best quality films which is the ratio in bath C [131].

Buffering the bath to pH~2.5 stabilises the bath chemistry and produces more stoichiometric stable films, as shown in figure 7.9 (b). Over the voltage range more gallium 10-16%, is deposited for the buffered bath as compared to 2-6% for the non buffered bath. This observation is consistent with the reports by Bhattacharya [130] and Calixto [131].

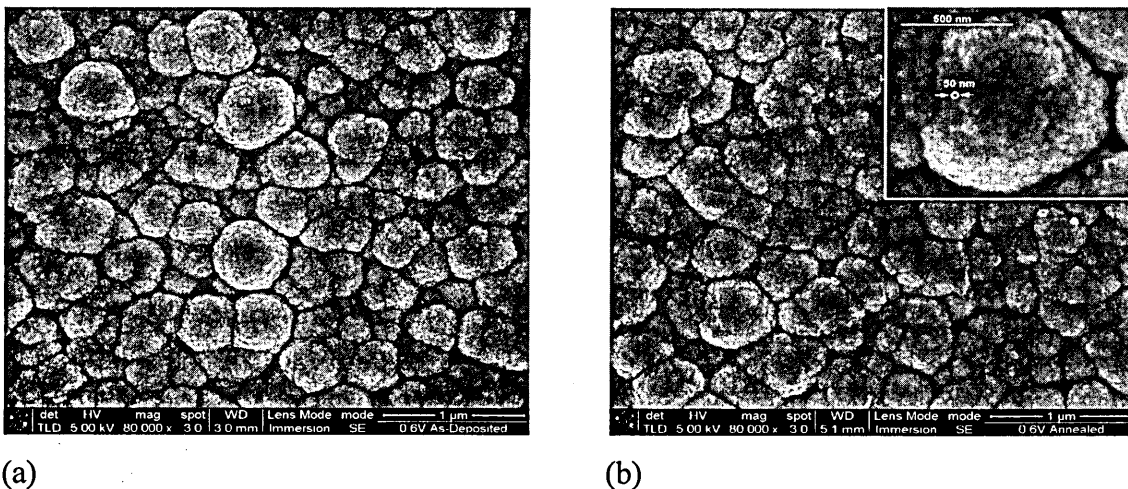
As shown by XRD very little gallium is being incorporated into the  $\text{CuInSe}_2$  lattice and therefore the gallium detected by the XRF must be in a different form. Calixto et al suggest the gallium may be in the form of gallium hydroxide. Gallium is incorporated into the films via the limited precipitation of the gallium hydroxide ions reacting with the  $\text{OH}^-(\text{aq})$  ions at the electrode surface and may not involve a redox step, which is consistent with the voltamogram. Therefore baths with a lower pH as in bath A would be expected to contain lower levels of Ga, as is observed.

#### 7.4.2 Influence of deposition voltage

Figure 7.9 shows XRF results of as-deposited samples from baths A and C. The trend is same in both baths. The percentage of selenium and copper decrease, indium and gallium increase as the deposition voltage increases. This increase in Ga and In is as expected since they both have significantly more negative deposition potentials than that of Cu and Se. This also confirms the PEC measurements, films deposited at less negative potentials are copper rich: p-type and at more negative potentials are In rich: n-type. Again this trend was observed by Calixto et al [131].

## 7.5 SEM analysis

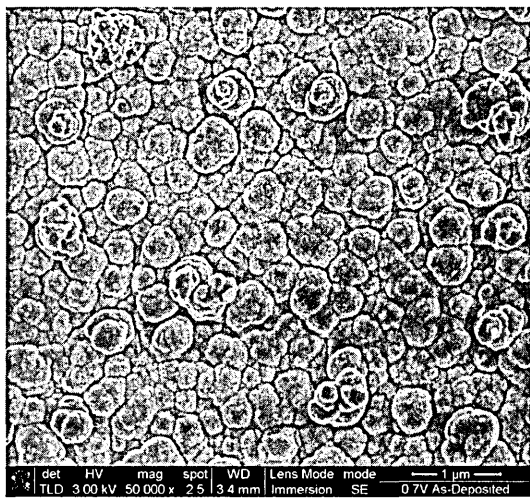
Figures 7.10 to 7.12 show that annealing the sample in air at 350°C for 20 mins, produces very little difference in the appearance of the surface morphology of the films, but we know from XRD that the grains become more crystalline after annealing, indicating the presence of polycrystalline CIGS.



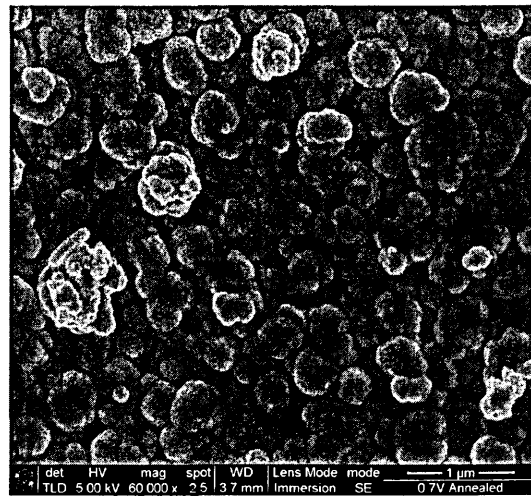
**Figure 7.10.** CIGS sample deposited at -0.60 V; (a) as-deposited and (b) annealed.

Figure 7.10(a) and (b) show SEM pictures for samples deposited at -0.60 V, which show small grains conglomerating to form clusters of 300-500 nm diameter. The inset shown in figure 7.10(b) shows an expansion of one of the clusters, and the individual crystallite can be identified to have a diameter of ~50 nm, which confirms the calculated size. These large ‘cauliflower like’ growths are typical of  $\text{Cu}_x\text{Se}_y$  phases and have also been observed by Calixto et al [131] and Olivera et al [136]. These results confirm the PEC and XRF results, that films grown at less negative potentials are copper and selenium rich.

Figure 7.11(a) and (b) show SEM pictures for samples deposited at -0.70 V, these are very similar in appearance to samples grown at -0.60 V, the only difference being that the grain clusters are slightly smaller.



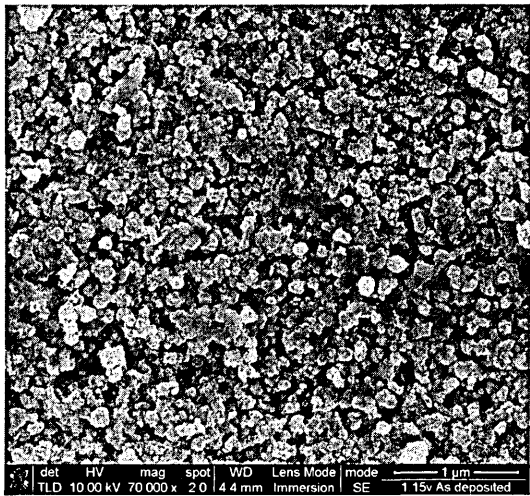
(a)



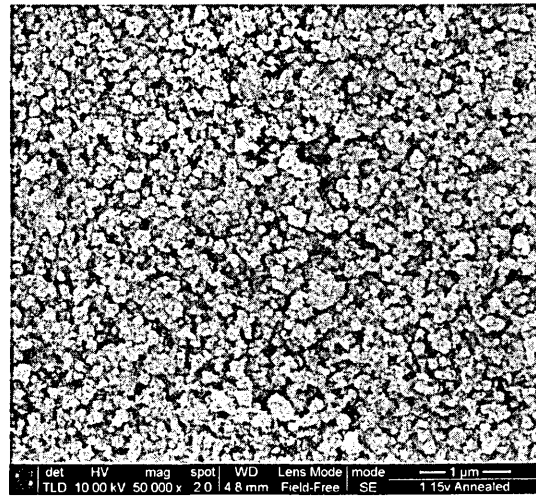
(b)

**Figure 7.11.** CIGS sample deposited at -0.70 V; (a) as-deposited and (b) annealed.

Figure 7.12(a) and (b) show SEM pictures for samples deposited at -1.15 V. These are significantly different, very small grains, not conglomerating into clusters. The grains appear not to well adhered to the surface (powdery), which was observed during the deposition process; again this is typical of indium rich films [133].

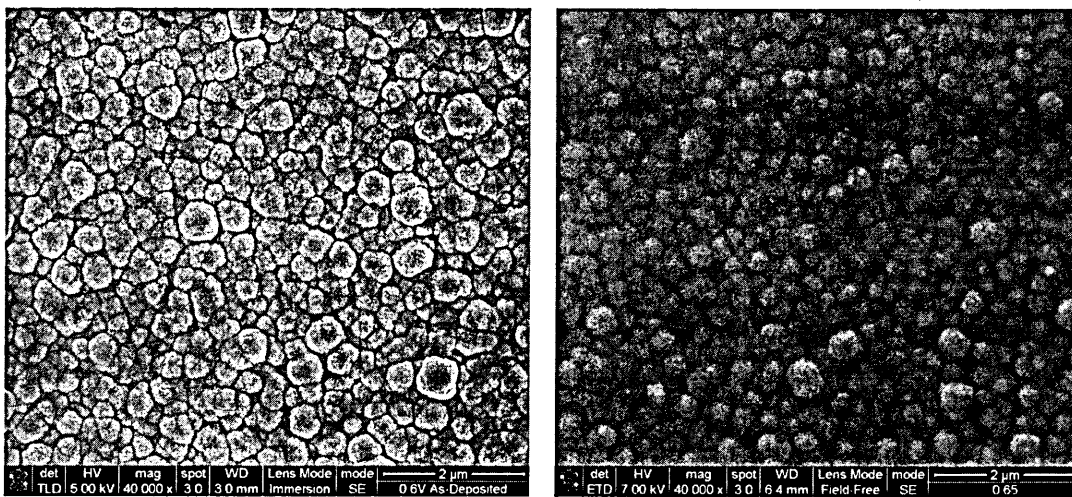


(a)



(b)

**Figure 7.12.** CIGS sample deposited at -1.15 V; (a) as-deposited and (b) annealed.



(a)

(b)

**Figure 7.13.** As-deposited CIGS sample deposited at -0.65 V; (a) bath A and (b) Bath C.

Figure 7.13 shows the morphology of as-deposited CIGS layers grown from baths A and C to be very similar, with the small grains conglomerating to form clusters with 300 - 500 nm diameter. Again as with the previous results, annealing did not cause the grains/clusters to become significantly larger.

## 7.6 Summary of main results for material characterisation.

PEC analysis show that the conductivity type of the material deposited changes from  $p^+$  to  $n^+$ , as the deposition potential is increased to higher negative potentials.

XRF shows that the concentrations of Cu and Se decrease, while the concentrations of In and Ga increase, as the deposition potential is increased to higher negative values.

XRD and SEM analysis show that the CIGS films deposited by electrodeposition are polycrystalline, with individual crystallite sizes in the range of 5 - 7 nm for as-deposited films and 14 - 39 nm for annealed films. Large numbers of these small crystallites form larger clusters with diameters of 300-500 nm and the size of these clusters does not significantly increase after annealing.

## 7.7 I-V characteristics of preliminary superstrate nnip devices.

A typical I-V characteristics of a preliminary n-n-i-p device is shown in figure 7.14, the device structure was glass/FTO/CdS/nip(CIGS)/Au, the deposition voltages were -0.75 V(n), -0.70 V(i) and -0.65(p) as determined by PEC results. The low FF may be due to high series resistance, created by the small grains and scattering centres therefore we need to anneal at higher temperatures to increase the grain size and reduce defects. All devices tested on the sample were photo active, and their  $J_{sc}$  and  $V_{oc}$  values are summarised in figure 7.15. The device highlighted gave the best overall efficiency, and its I-V curve is the one shown in figure 7.14.

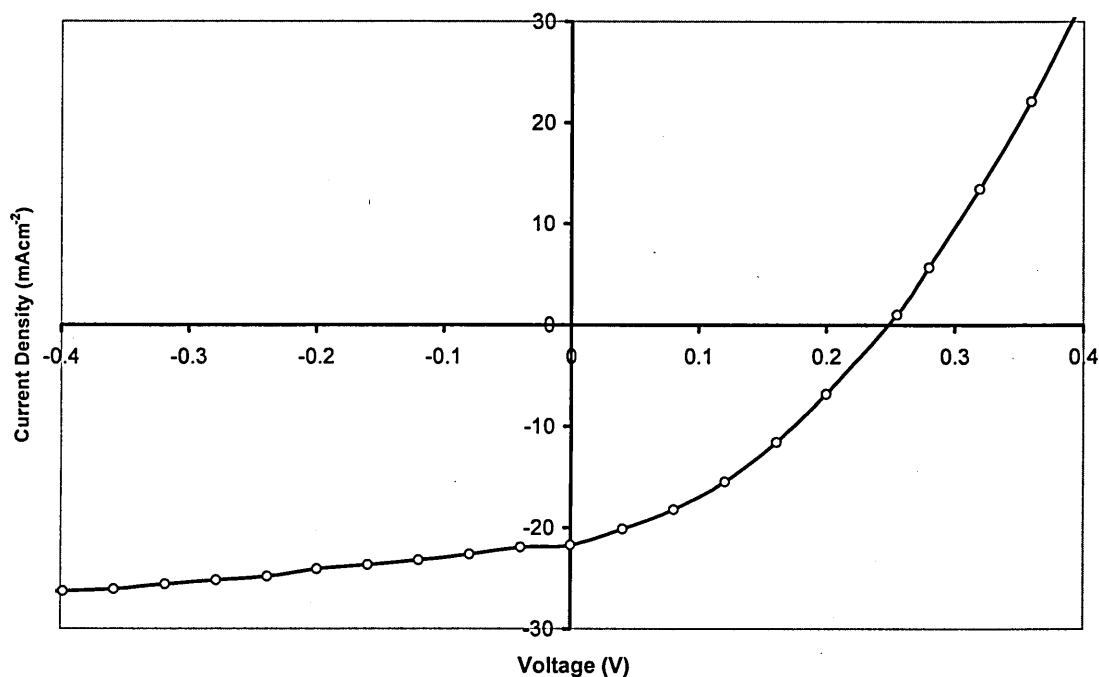


**Figure 7.14.** A typical I-V curve of initial devices under AM 1.5 illumination conditions ( $V_{oc}$ ~240 mV,  $J_{sc}$ ~22 mA cm<sup>-2</sup>, FF~0.38 and  $\eta$ ~2.0%), active area = 0.03 cm<sup>2</sup>.

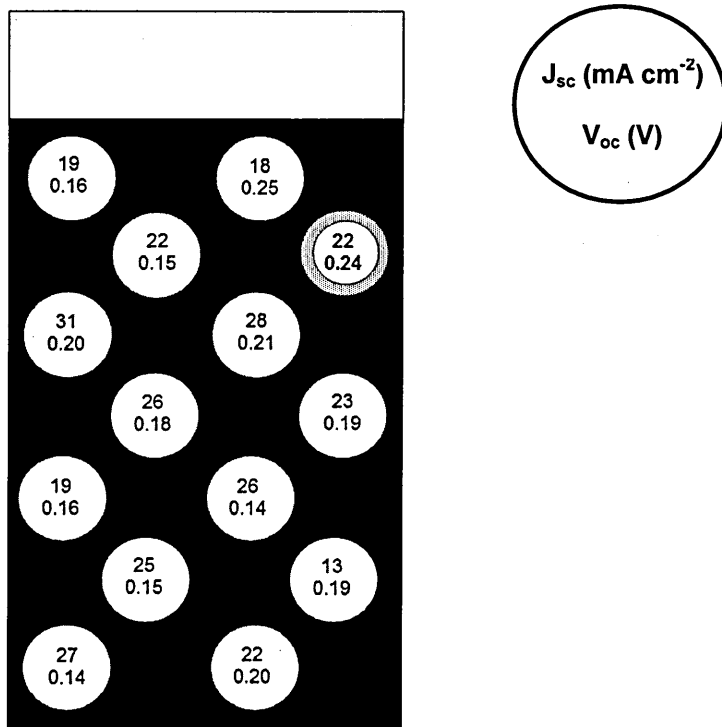


**Figure 7.15.** Diagram of all devices tested on sample, the cell highlighted gave the best device parameters and the I-V characteristics are shown in figure 7.14.

A possible reason for the low  $V_{oc}$ , is that gallium forms gallium hydroxide and is not forming CIGS [131]. This can be seen from the XRD, as the peak positions are very near to CIS and are shifted to the right by only a small amount. Annealing at higher temperatures the gallium should become incorporated into the CIS lattice, which should improve the device performance, as the bandgap will be increased and hence a higher  $V_{oc}$ , but this can deteriorate the quality of the CdS layer.

## 7.7 Discussion of results and conclusions

This work has shown that it is possible to grow predetermined CIGS layers with  $p^+$ , p, i, n and  $n^+$  type electrical conduction by electrodeposition from a single bath and previous published work has shown that the bandgap increases as the deposition voltage increases[137]. However, growing these layers in sequence on top of each other to produce a multi-layer graded bandgap solar cell has proved to be difficult and unpredictable. Some of these issues are described below.

Three different device structures were tested:

(i) Glass/FTO/n-CdS/n-CIGS/i-CIGS/p-CIGS/metal: in this structure the first CIGS layer is n-type, and is deposited on the CdS layer. As the results show, n-type layers are deposited at higher negative potentials, which produce a less crystalline, powdery film. This then acts as a poor substrate for the subsequent i and p-type layers, which when grown separately directly onto FTO has good morphological and structural properties.

(ii) Glass/FTO/n-CdS/p-CIGS/metal: to overcome this problem attempts were made to grow simple n-p diodes, depositing the p-type layer directly onto the CdS layer, but this always resulted in layers full of pin holes and never yielded any working devices, during the period of this project. This highlights the reproducibility issues related to this material.

The problem with both these device structures is that they can not be annealed at a high enough temperature to re-crystallise the CIGS layer (a) without the layer being destroyed and (b) without causing the CdS layer to deteriorate.

(iii) To try and address this problem; a third device structure, Glass/FTO/p-CIGS/CdS/metal was attempted. This is in effect the conventional 'substrate' device, where the Mo has been replaced by FTO; this was adopted because the p-CIGS layer was known to grow well directly on FTO and could be annealed at a higher temperature, prior to the deposition of the CdS layer. Again this never yielded any working devices, as the annealing step was not optimised, for this reason conventional substrate devices

were investigated, using Mo as the substrate and having a controlled annealing system. These results are presented in the next chapter.

Despite these problems the nnip device structure did deliver a working device, as reported in section 7.5; this worked because the range between the three deposition potentials was relatively small, with only 10 mV separation. The results show that these layers are in the p to i region and are very similar morphologically and structurally. Figure 7.16 shows the energy band diagram of the n-n-i-p solar cell structure tested in section 7.7, showing the deposition voltage of each layer. Note the decrease in band gap and the change from n to p type electrical conduction.

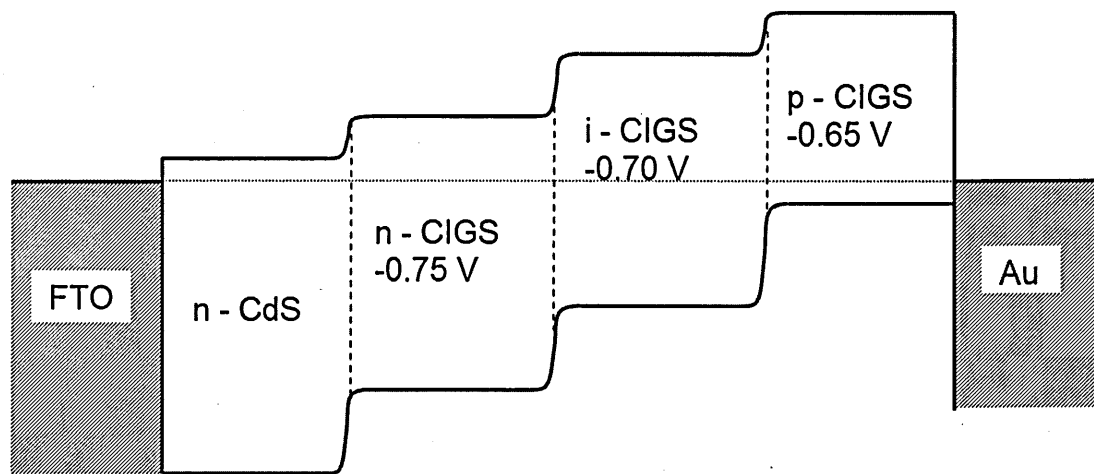


**Figure 7.16.** Energy band diagram of n-n-i-p solar cell structure.

However it should be noted that this device structure has produced good working devices in the past;  $V_{oc} \sim 570$  mV,  $J_{sc} \sim 36$  mAcm<sup>-2</sup>, FF  $\sim 0.40$  and a rectification factor with 6 orders of magnitude [129].

## Chapter 8: Development of CuInSe<sub>2</sub> substrate devices

### 8.1 Introduction

In this chapter, deposition, characterisation and development of substrate CuInSe<sub>2</sub> solar cells is discussed. Due to the difficulties outlined in chapter 7, especially the issue of annealing CdS superstrate devices at high temperature, devices were fabricated using the conventional device structure, glass/Mo/p-CuInSe<sub>2</sub>/CdS/i-ZnO/Al-ZnO/Al. Also gallium was omitted from the bath, again for reasons discussed in chapter 7.3.1.

### 8.2 Electrodeposition of CuInSe<sub>2</sub>

Electrodeposition of CuInSe<sub>2</sub> was carried out using an acidic aqueous bath with concentrations; 2.6 mM CuCl<sub>2</sub>, 9.6 mM InCl<sub>3</sub>, 5.5 mM H<sub>2</sub>SeO<sub>3</sub> and 240 mM LiCl, which was used as the supporting electrolyte. All chemicals were at least 5N purity, supplied by Aldrich and were used as received. A pH 3 Hydrion buffer was used which is a mixture of sulphamic acid and potassium biphthalate, this permits the absorption of free OH<sup>-</sup> and H<sup>+</sup> ions that are present in the deposition bath, thereby controlling the pH [130,138]. The films were deposited at room temperature, with a pH ~ 2.6 without stirring using a standard 3-electrode system. The anode was a high purity graphite plate, the reference electrode was Ag/AgCl and the cathode or the working electrode was a glass/Mo (supplied by Pilkington Group plc.). The best quality films were deposited when the Mo substrate was pre-treated by a 1 minute deposition at -0.476 V. The substrate was then removed from the bath, rinsed in de-ionised water and dried under flowing N<sub>2</sub> gas. The layer was then completed with a further deposition of 20 minutes at -0.476 V, followed by 50 minutes at -0.576 V. For full re-crystallisation of the CuInSe<sub>2</sub> layers, annealing was carried out in a tube furnace for 30 minutes at 550°C under flowing H<sub>2</sub>(5%)/Ar gas and a Se rich atmosphere. The layers were then etched in 0.1M KCN for 2 minutes prior to the deposition of CdS, using the standard chemical bath technique.

## 8.2.1 Cyclic Voltammetry (CV)

In order to understand the Cu + In + Se system, CV data was taken from different baths, the order in which the elements were added to the bath was investigated, to understand how the surface of the modified electrode by the previous deposit effects the mechanism of film growth. Table 8.1 summarises the CV experiments carried out.

**Table 8.1.** Order of elements added to bath and electrode condition.

Figure No.	Order of elements added to the bath	Condition of the electrode
Figure 8.1	Cu, Cu-Se, Cu-Se-In	New
Figure 8.2		Same
Figure 8.3	Cu, Cu-In, Cu-In-Se	New
Figure 8.4		Same

### 8.2.1.1 Cu-Se-In system

In figure 8.1 a new electrode was used for each CV taken. Curve (1) shows that -0.30 V is the onset of the deposition of copper, note the current is very low. At  $\sim -0.70$  V there is a steep rise in current, this is common in all the data, as is the onset of hydrogen evolution at the cathode.

Curve (2); when copper and selenium are in the bath, there is now a large steep increase in current peak (A) starting at -0.17 V. This is due to the favourable free energy of the selenium, which shifts the deposition potential of the copper to a less negative value, forming a copper selenide phase. Another copper selenide phase is present a -0.65 V, peak (B).

Curve (3); when indium is added to the bath, peak (A) now moves to -0.30 V, as indium which has a more negative deposition potential than that of Cu and Se, starts to deposit. Peak (B) is now reduced, which is the possible deposition of  $\text{CuInSe}_2$ .

In figure 8.2 the same electrode is used for each CV taken.

Curve (1) as expected is the same, as it is just copper on a new electrode.

Curve (2); this clearly shows how the surface of the electrode effects the deposition, Peak (A) is now not well defined and has reduced. Peak (B) is still in the same place, showing what ever copper selenide phase this is, it is the most favourable.

Curve (3); now with copper selenide as the substrate, peak (A) has disappeared

completely and peak (B) has become more dominant. However, the film here was not well adhered to the substrate and possessed a gel like appearance. The reason why the current is still high, is because this material is still depositing but it is in effect forming before it contacts the electrode, due to the surface modification of the electrode. Note, this non adhered film/peeling off has been observed many times in this work, see chapter 7, and it usually occurs at potentials between -0.52 and -0.58 V. Work carried out by Calixto et al [139] and Oliveira et al [140] observed similar results.

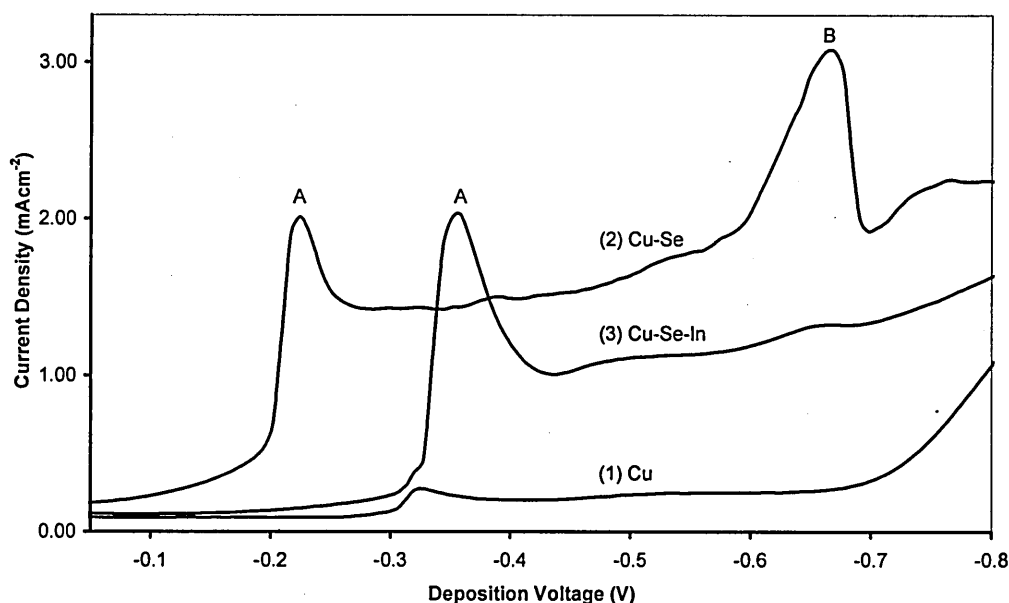


**Figure 8.1.** CV of Cu-Se-In system with a new electrode.

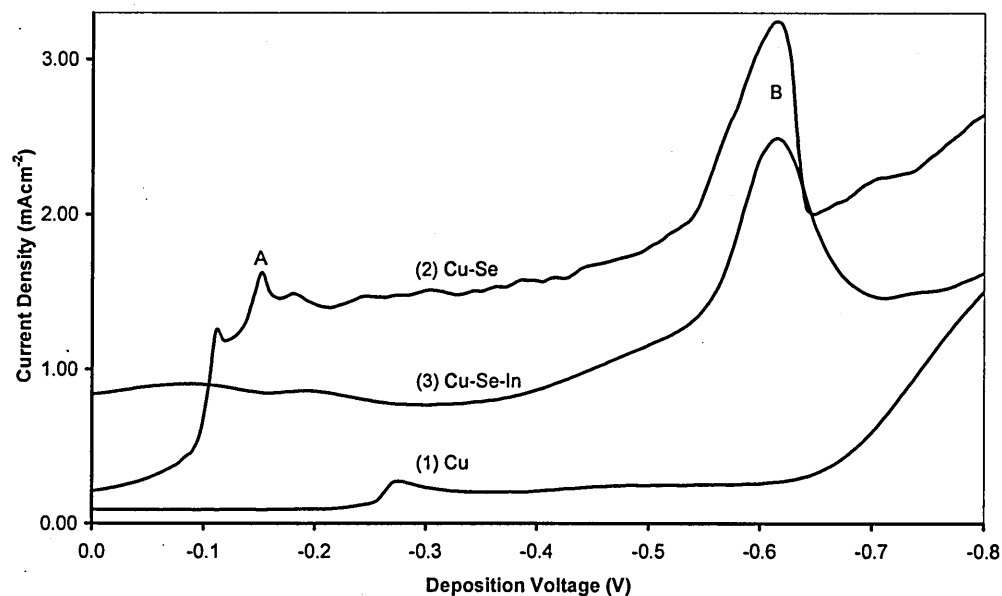


**Figure 8.2.** CV of Cu-Se-In system with the same electrode.

### 8.2.1.2 Cu-In-Se system

Figure 8.3: the same electrode is used for each CV taken;

Curve (1) as expected is the same, as it is just copper on a new electrode.

Curve (2) and (3); again this is a clear example of what happens when the surface of the electrode is modified, with indium now added to the system, an alloy of copper-indium forms. This is a very stable alloy, having no nucleation sites, which is why when the selenium is added, curve (3), the deposition of selenium is prevented.

Figure 8.4; a new electrode is used for each CV taken.

Curve (1) and (2); again copper-indium forms and prevents any further reactions from taking place. But now when the electrode is changed for a new one, curve (3) the 'blocking layer' is now absent and the Cu-In-Se system can now deposit normally.

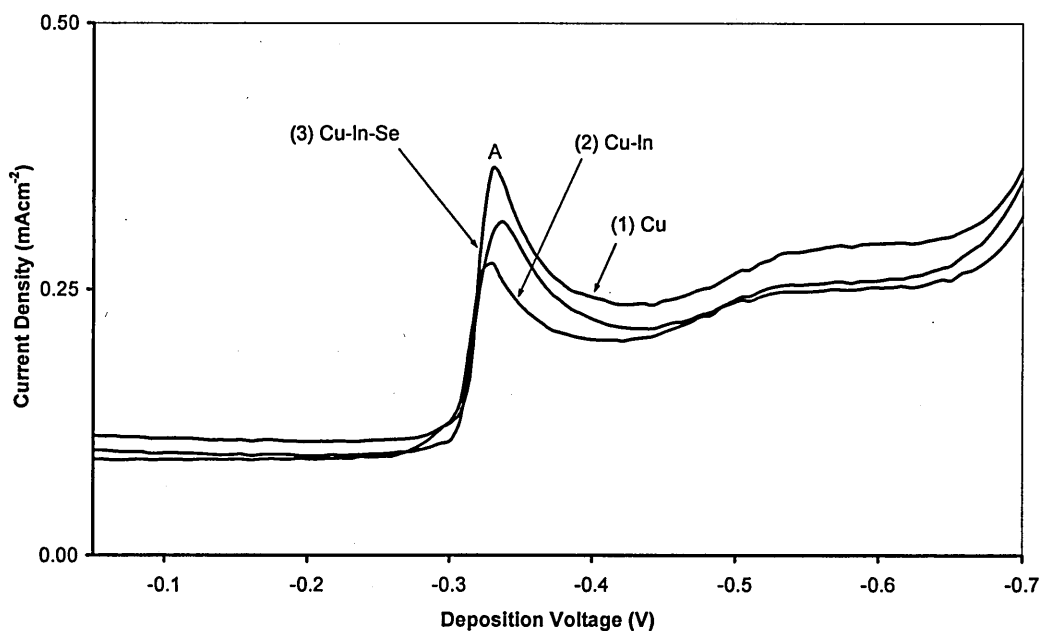
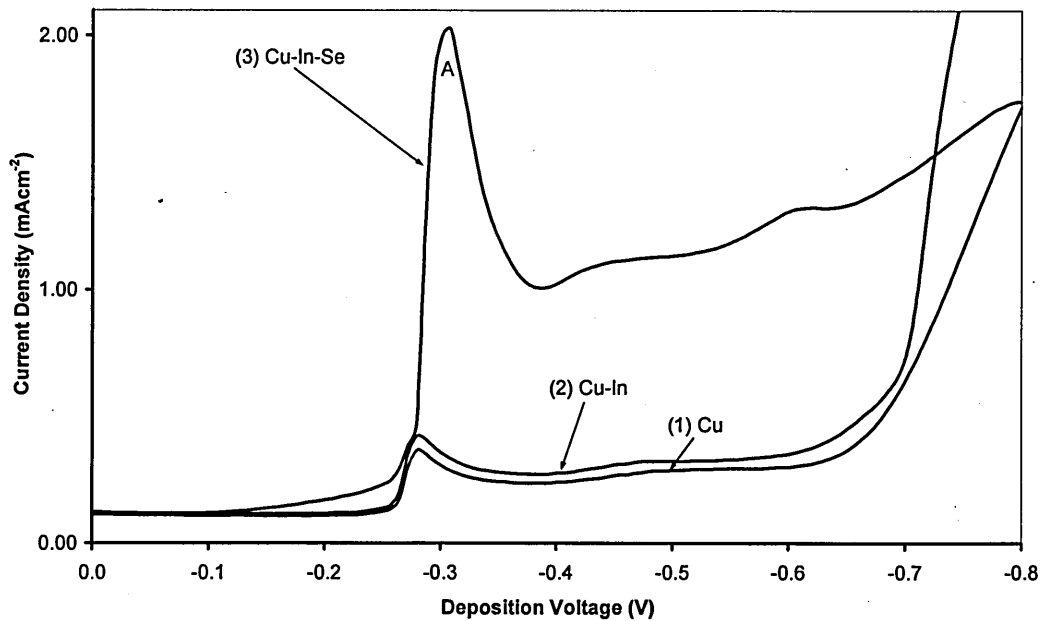


Figure 8.3. CV of Cu-In-Se system with the same electrode.



**Figure 8.4.** CV of Cu-In-Se system with a new electrode.

### 8.2.1.3 Mechanism of $\text{CuInSe}_2$ film growth

Because the Cu-In-Se system on a new electrode is the one that is used in a normal deposition process, this CV was studied in detail and a mechanism for the film growth is proposed.

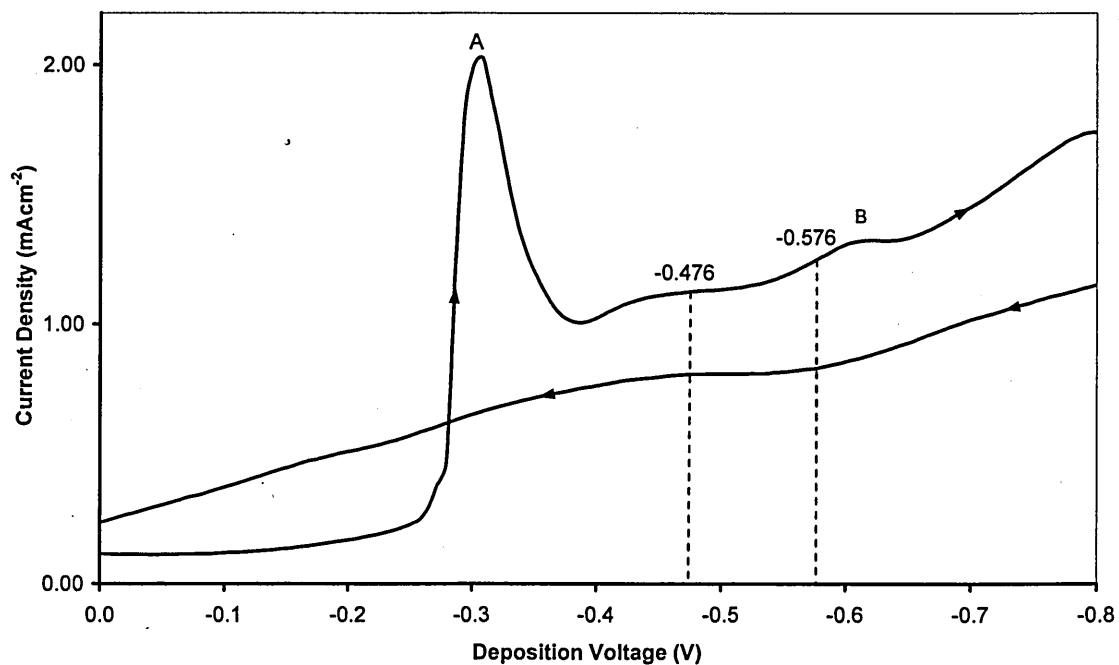


**Figure 8.5.** Typical voltammogram for  $\text{CuInSe}_2$  deposited on Mo, showing position of deposition potentials used to grow devices.

The reactions used to propose the mechanism of film growth, were selected from a comprehensive paper by Mishra and Rajeshwar [141], which covered a detailed voltammetric study of the electrodeposition chemistry of the Cu-In-Se system.

The initial current onset 0.00 to -0.27 V is due to the reduction of  $\text{H}_2\text{SeO}_3$  to Se (reaction 8.1), which has a standard reduction potential of 0.74 V.



The next small increase in current at -0.27 V is probably due to the formation of CuSe (reaction 8.2).



This then rapidly reduces to form  $\text{Cu}_3\text{Se}_2$  (reaction 8.3) and  $\text{Cu}_2\text{Se}$  (reaction 8.4) causing a rapid increase in current at peak (A).



This has also been observed by Calixto et al [113] and the thermodynamic process is explained by Kröger [142].

With a further increase in negative potential this causes the formation of indium selenides  $\text{In}_2\text{Se}_3$  (reaction 8.5) and  $\text{InSe}$  (reaction 8.6)



This under-deposition of indium is facilitated by the favourable free energy given by the reaction with selenium.

Another possible explanation is given by Calixto et al [138]; at these increased negative potentials and pH 2.6, H<sub>2</sub>Se is the likely phase of dissolved selenium. The liberated H<sub>2</sub>Se reacts with In<sup>3+</sup> forming In<sub>2</sub>Se<sub>3</sub> (reaction 8.7).



As the negative potential increase further there is a steady increase in current until another peak is reached starting at -0.53 V, peak (B). At this point reduction reactions are likely to occur between H<sub>2</sub>Se, CuSe and In<sub>2</sub>Se<sub>3</sub> (reactions 8.8 and 8.9). Also indium will now start to deposit as the standard reduction potential of In is reached (-0.339 V vs NHE) (reaction 8.10).



A rise in current beyond -0.65 V occurs due to the onset of hydrogen evolution (reaction 8.11).



### 8.3 XRF and XRD analysis of as-deposited samples

A series of 9 small samples were deposited on Mo substrates starting at 0.1 V and increasing in 0.1 V intervals, to identify the composition of the layers (XRF) and phases present (XRD).

Figure 8.6 shows XRF data for the series. Again the trend is similar to previous results, as the negative voltage increases, copper decreases and indium increase, the main difference here is that selenium seems to stay more or less constant. Note at deposition voltages of -0.10 and -0.20 V, virtually no indium is present in the layers, which

concur with the explanation of the voltamogram, and therefore the layer is just a copper selenide phase, which is also confirmed by XRD.

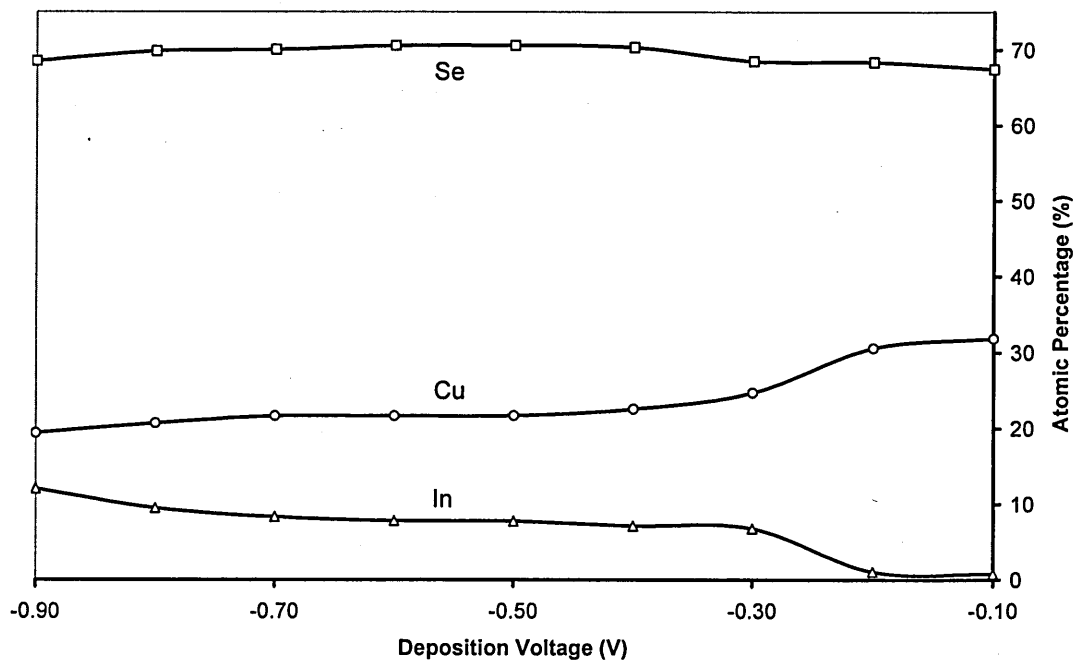


**Figure 8.6.** XRF of  $\text{CuInSe}_2$  deposited on Mo as a function of deposition voltage.

Figure 8.7 shows glancing angle XRD spectra of as-deposited samples, deposited at -0.20, -0.40, -0.60 and -0.80 V; curves (a), (b), (c) and (d) respectively. Figure 8.7(a) deposition at -0.20 V has been identified as  $\text{Cu}_2\text{Se}_3$ , the Mo peak at  $2\theta = 40.5^\circ$  has been cut off, as this was a very intense peak due to the thickness of the film. In the subsequent three spectra (b-d), there is a shift of  $\sim 1.0^\circ$  on all three major peaks, to the position of CIS related compounds. The copper selenide phase at  $\sim 2\theta = 25.2^\circ$  is present on (b) and (c), but has all but disappeared on (d), the film deposited at -0.80 V. This is expected as more indium and less copper is now present, as shown by XRF also.

Also note that the most intense and 'CIS' type spectra is shown by (c), even with these as-deposited samples, confirming what was found in chapter 7, that around -0.60 V produces the quality and type of layers needed.

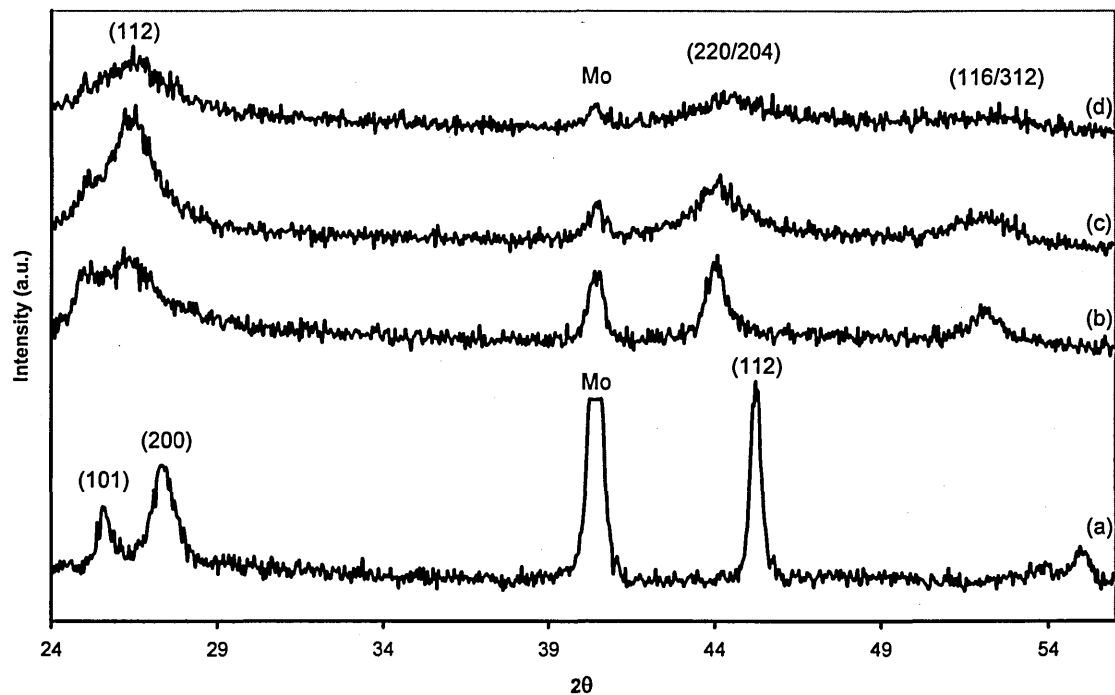


**Figure 8.7.** XRD spectra of as-deposited samples at; (a) -0.20 V ( $\text{Cu}_2\text{Se}_3$ ), (b) -0.40 V, (c) -0.60 V and (d) -0.80 V.

#### 8.4 Thickness measurements

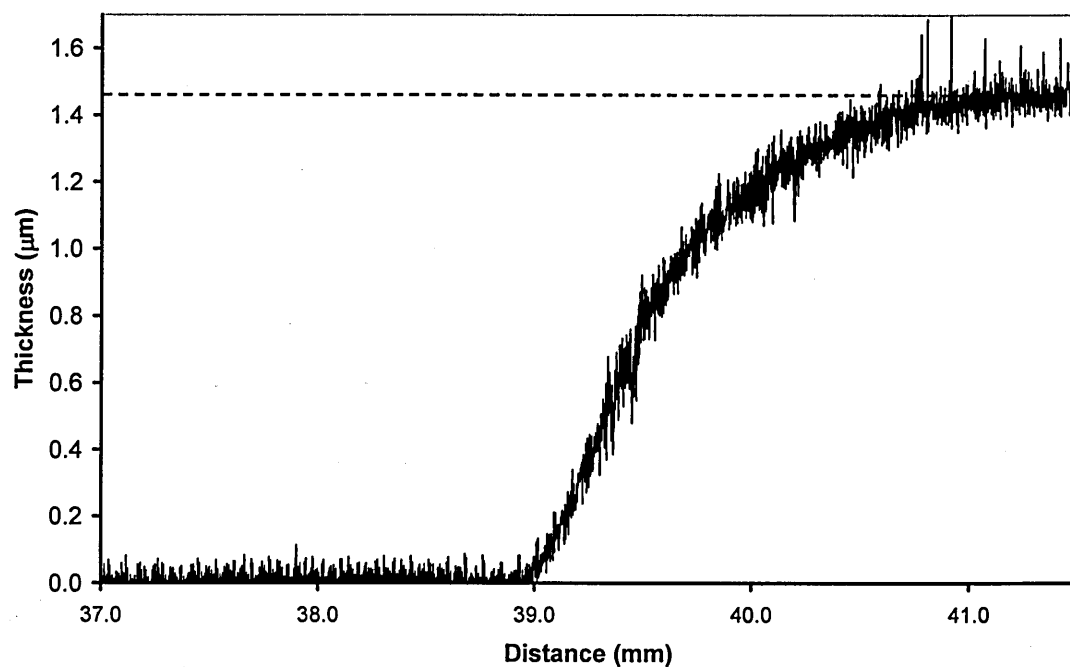
The thickness of the film was determined by three methods; (i) using Faradays equation of electrolysis, (ii) gravimetric analysis and (iii) Talysurf (mechanical method), figure 8.8 shows a plot along the length of a typical sample.

Figure 8.9 shows a plot of current density versus voltage for a typical sample ( $2 \text{ cm} \times 2 \text{ cm}$ ) deposited at -0.576 V. The average current density was found to be  $\sim 0.60 \text{ mAcm}^{-2}$  and this value was used to calculate the thickness used in method (i) (note how stable the current is over time). The large current at the start of deposition is due to the formation of initial nucleation centres.

(i) Faradays equation thickness =  $1.55 \mu\text{m}$

(ii) By weight thickness =  $1.65 \mu\text{m}$

(iii) By Talysurf =  $1.45 \mu\text{m}$



**Figure 8.8.** Talysurf plot of an as-deposited sample, deposited at -0.576 V.

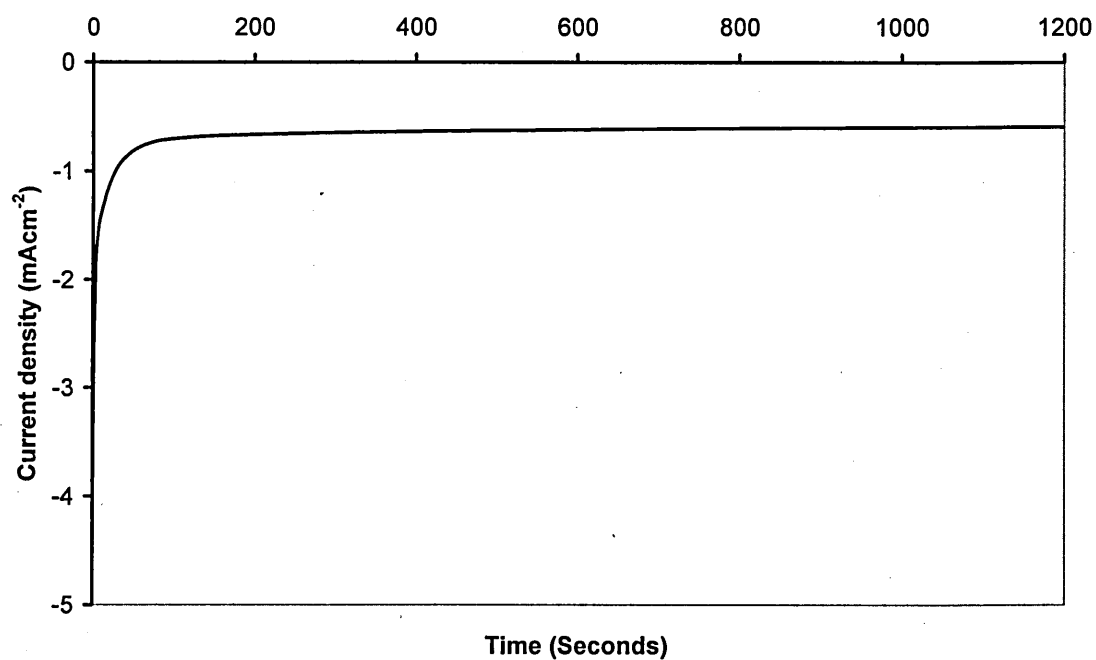


**Figure 8.9.** Plot of current density versus time for typical CuInSe<sub>2</sub> sample, showing average current density  $\sim 0.60 \text{ mA cm}^{-2}$ .

## 8.5 Annealing conditions

All electrodeposited  $\text{CuInSe}_2$  films at room temperature, have poor crystallinity and require an annealing step. It is very important that the sample does not oxidise and that the selenium does not evaporate. Most research groups anneal in  $\text{H}_2\text{Se}$  gas, which is very toxic, and because no safe exposure limit could be identified in the UK, it is not possible to obtain outside the licensed industries [143]. To carry out successful annealing another process method was devised. The basic schematic set up used is shown in figure 8.10.

In order to keep/add selenium to the sample, a conducting glass plate with a layer of electrodeposited selenium was placed over the sample. This was then placed in a graphite tray which held several selenium pellets; this was then placed inside the confinement vessel, which was a glass tube with a small hole in each end. The vessel was then placed inside a pre-heated tube furnace at a temperature of 450-600°C, the tube was then evacuated and filled with  $\text{H}_2$ 5% /Ar gas.

The furnace temperature, the annealing time, the gas flow rate and the number of selenium pellets were investigated as variables. It was found that a temperature of 550°C, for 30 minutes, with two selenium pellets and a gas flow rate of 0.5 l/s gave the best and reproducible results. These parameters gave an average weight gain of 60% to the sample, which equates to an average increase in film thickness of 0.7  $\mu\text{m}$ , (this was reduced to 0.5  $\mu\text{m}$  after etching in KCN), giving a final total film thickness of  $\sim$ 2.0  $\mu\text{m}$ .

If too many selenium pellets were added to the graphite tray they would 'sputter' onto the surface of the sample and destroy it, too few or no selenium pellets would result in sections of the surface evaporating completely. If the gas flow rate was too fast, too much selenium would leave the tube, resulting in a weight loss in the sample, indicating a loss of selenium. If no selenium cover plate was used the sample would sublime completely. An SEM study of annealing time, temperature and inclusion of selenium pellets is given in the next section.

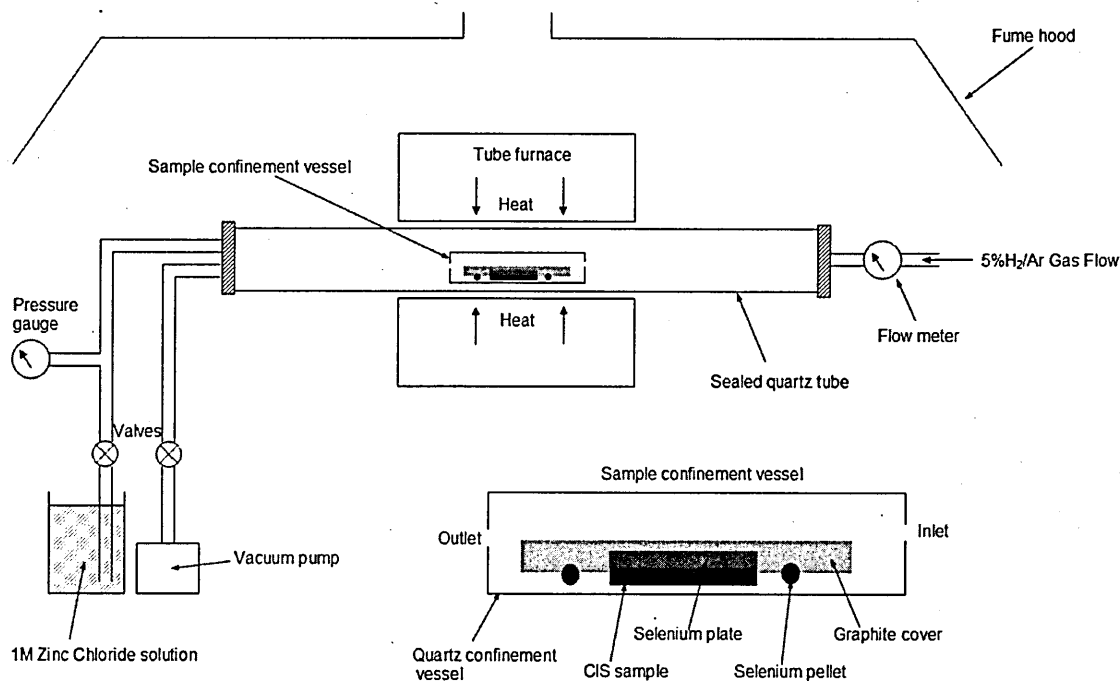


**Figure 8.10.** Schematic diagram of annealing set up used for  $\text{CuInSe}_2$  layers.

## 8.6 SEM study of effects of annealing $\text{CuInSe}_2$ under different conditions

All samples were deposited on Mo, using the multi-voltage technique, as outlined in the introduction; 1 minute at  $-0.476$  V, 20 minutes at  $-0.476$  V and 50 minutes at  $-0.576$  V. These were then annealed under different conditions.

### 8.6.1 Effect of temperature and addition of selenium pellets

Figure 8.11(a) shows a sample annealed at  $500^\circ\text{C}$ , without any selenium pellets, large holes appear in the sample, this is where selenium has sublimated from the sample. Adding 2 selenium pellets clearly improves the layer, figure 8.11(b). Increasing the temperature to  $550^\circ\text{C}$  stops the holes in the layer appearing, but the layer is made up of very small, none inter-connected crystallites, figure 8.11(c). Again adding the selenium pellets clearly improves the quality of the layer, with the layer becoming more homogenous and the crystallite size increasing, figure 8.11(d). Since it was evident that the addition of selenium improves the quality of the layer, two selenium pellets were added to subsequent annealing trials.

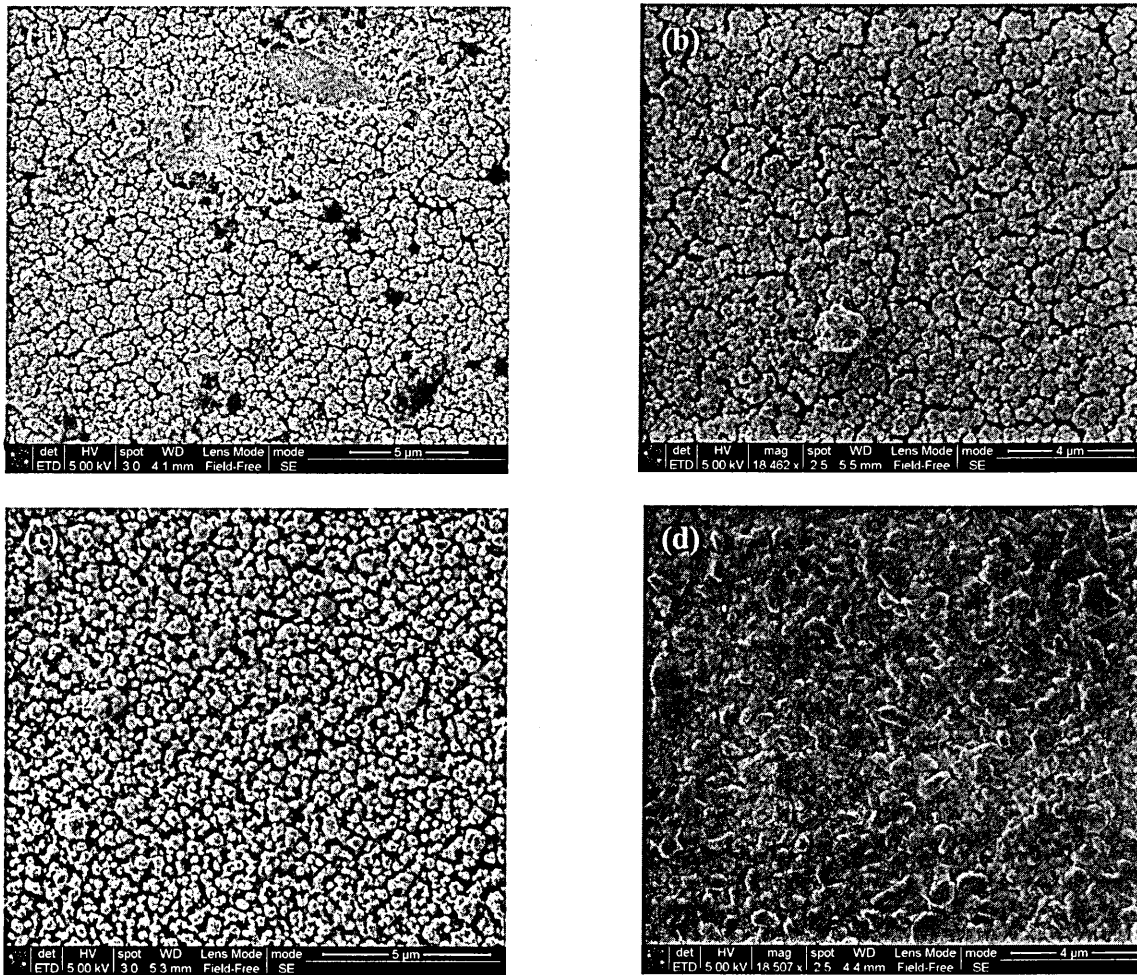


**Figure 8.11.** SEM pictures of annealed CuInSe<sub>2</sub> samples, showing effect of annealing temperature and the addition of selenium pellets, (a) 500°C, no selenium, (b) 500°C, with selenium, (c) 550°C, no selenium and (d) 550°C, with selenium.

### 8.6.2 Effect of annealing temperature

Figure 8.12(a) shows a sample annealed at 500°C, there are spaces around the crystallite clusters, indicating that more selenium needs to enter the layer and the temperature, needs to be higher for crystallisation. In figure 8.12(b) the sample was annealed at 525°C, this clearly shows that the spaces are starting to connect and the layer is becoming more homogenous. Figure 8.12(c) shows a sample annealed at 550°C, the spaces have connected, and the clusters have re-crystallised, forming larger crystals of ~300-400 nm. Figure 8.12(d) is a high magnification SEM of the larger crystallites shown in figure 8.12(c), which shows that each crystallite actually consists of smaller crystals.

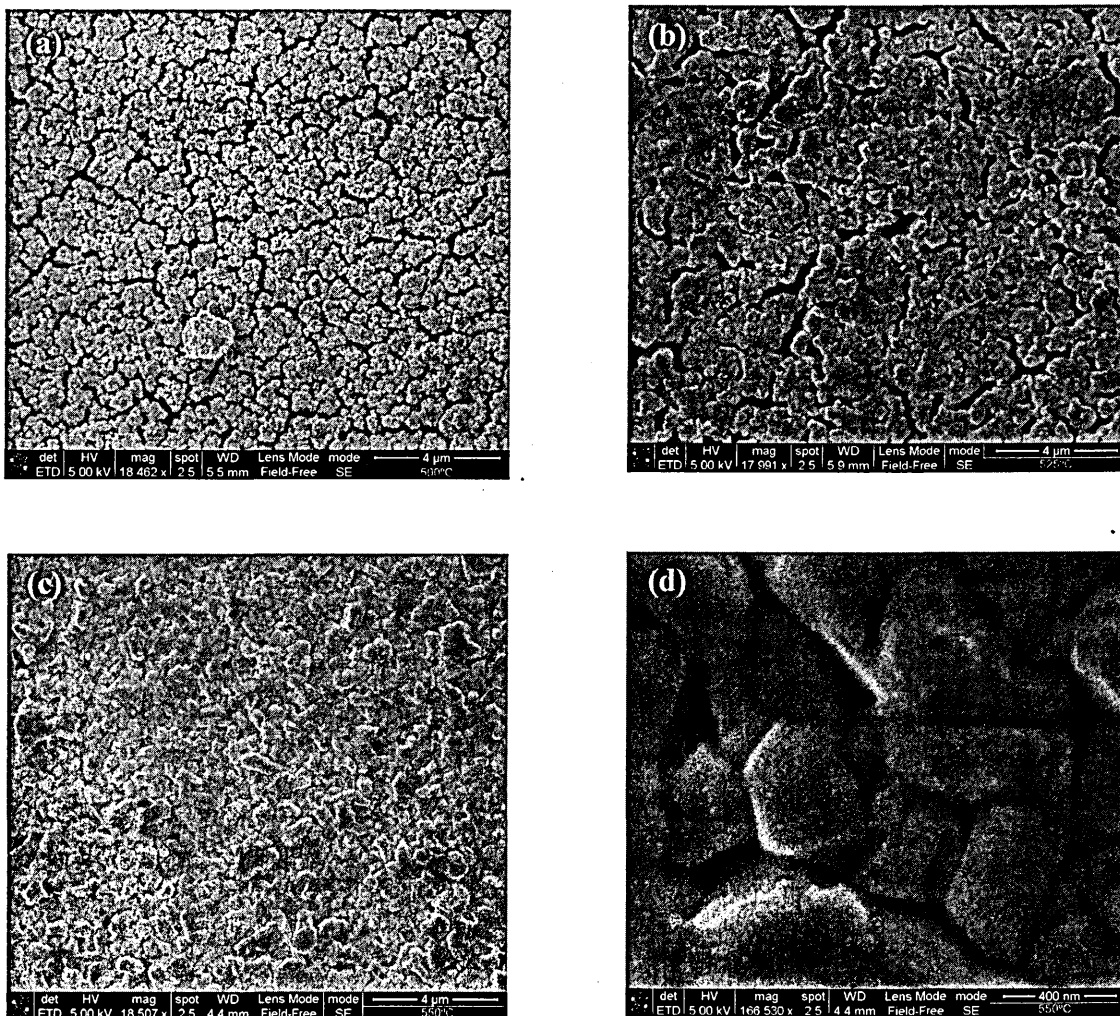


**Figure 8.12.** SEM pictures of CuInSe<sub>2</sub> samples annealed at (a) 500°C, (b) 525°C, (c) 550°C and (d) is a high magnification picture of (c).

### 8.6.3 Effect of annealing time

In order to investigate the effects of annealing time, samples were annealed at 550°C, with selenium pellets for different lengths of time. Figure 8.13 (a)-(d), shows that as the annealing time increases (from 10 through to 30 minutes) the crystallites gradually increase in size. At 30 minutes the crystallites are becoming fused to form a complete layer. Samples annealed for longer than 30 minutes were destroyed.

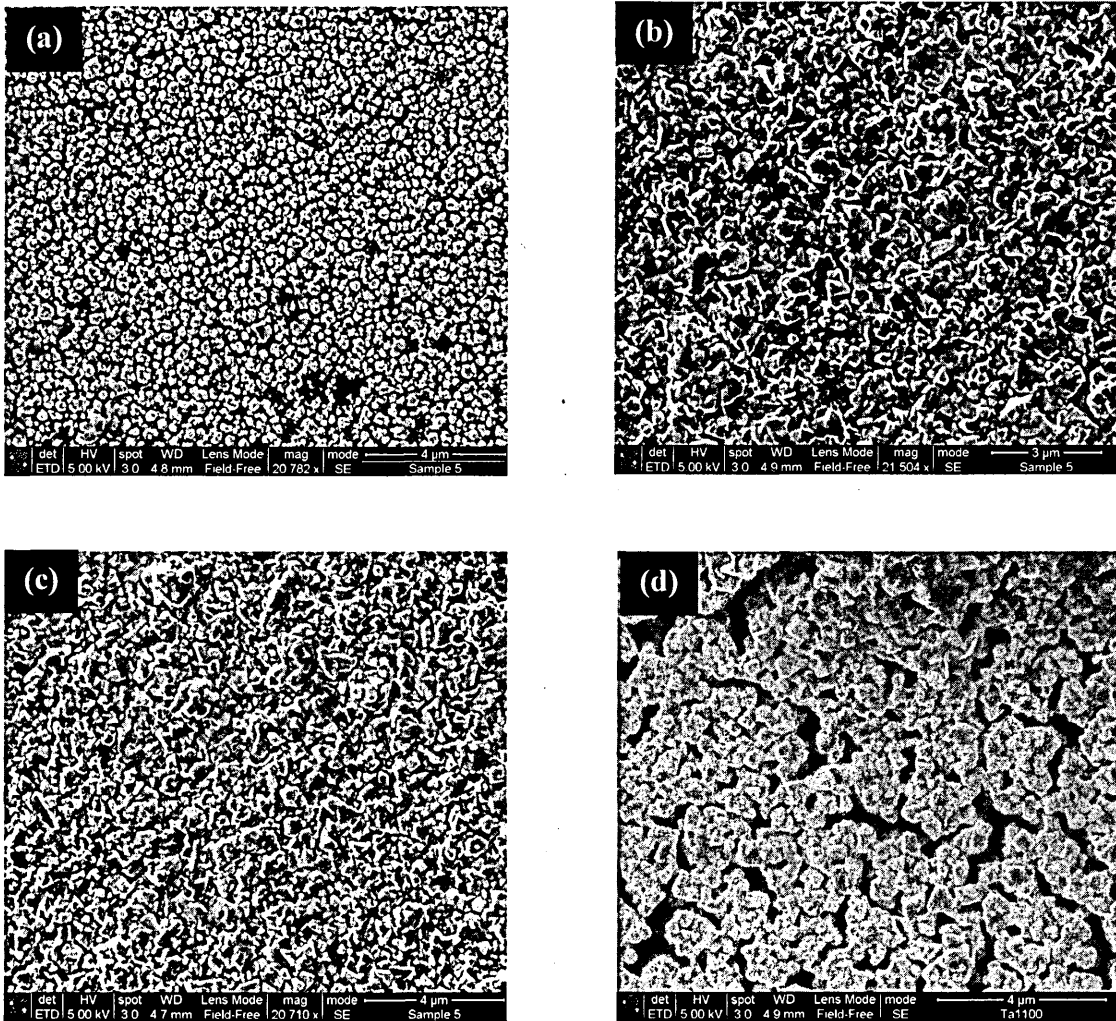


**Figure 8.13.** SEM pictures of  $\text{CuInSe}_2$  samples annealed at  $550^\circ\text{C}$  for (a) 10 mins, (b) 15 mins, (c) 20 mins and (d) 30 mins.

Figure 8.14 shows a cross section of the  $\text{CuInSe}_2$  layer, which shows the thickness after annealing  $\sim 2.0\mu\text{m}$ . This confirms the thickness calculated by weight gain after annealing.

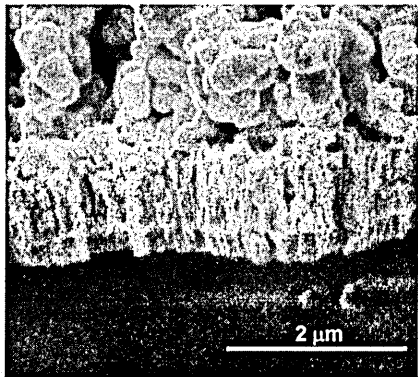


**Figure 8.14.** Cross section of the  $\text{CuInSe}_2$  layer, glass/Mo/CIS.



## 8.7 AFM analysis

AFM concurs with the SEM results, the as-deposited samples have a smaller grain size. Also after annealing the mean surface roughness reduces from 18.59 nm to 7.82 nm, figure 8.15(a) and 8.15(b) respectively as would be expected, as the grains have 'relaxed' and become more crystalline.

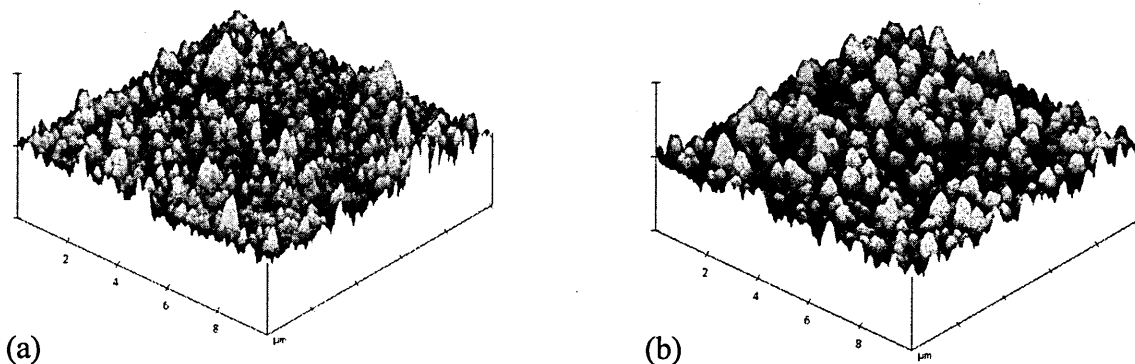


**Figure 8.15.** AFM images of CuInSe<sub>2</sub> samples; (a) as-deposited and (b) annealed.

## 8.8 XRD analysis

XRD studies were carried out to identify the crystallinity, composition and phases of the deposited CIS thin films. A Philips Expert X-ray diffraction system fitted with a CuK $\alpha$ 1 anode was used, operating with a glancing angle of 0.5°.

### 8.8.1 Three voltage deposition

The CuInSe<sub>2</sub> layer was made up of three layers deposited at three different potentials, as described in section 8.2. XRD spectra of these layers are shown in figure 8.16 (a)-(c). All spectra show chalcopyrite structure with major reflections from (112), (220/204) and (312/116) planes. Even the XRD of the layer deposited at -0.476 V for one minute (a), shows these three peaks even though they are of low intensity and broad. The Mo peak at  $2\theta = 40.5^\circ$  has been cut off, as this was a very intense peak due to the thickness of the film. When the deposition time is increased to 20 minutes, with the voltage remaining at -0.476 V (b), the three peaks are now well defined, and fit the standard

data for  $\text{CuInSe}_2$ . The shoulder to the left of the (112) peak marked by an 'x' is identified as  $\text{Cu}_2\text{Se}_3$ . The layer deposited at  $-0.576$  V for 50 minutes (c), the copper selenide phase is no longer present, and the three major peaks are broader and of less intensity than that of (b). This is because copper selenide is easier to deposit and is always very crystalline, with larger grains, this being the main reason for using this multi-voltage regime, as the more copper selenide layer produces a better seed layer than that of Mo to deposit the bulk of the  $\text{CuInSe}_2$  [131].

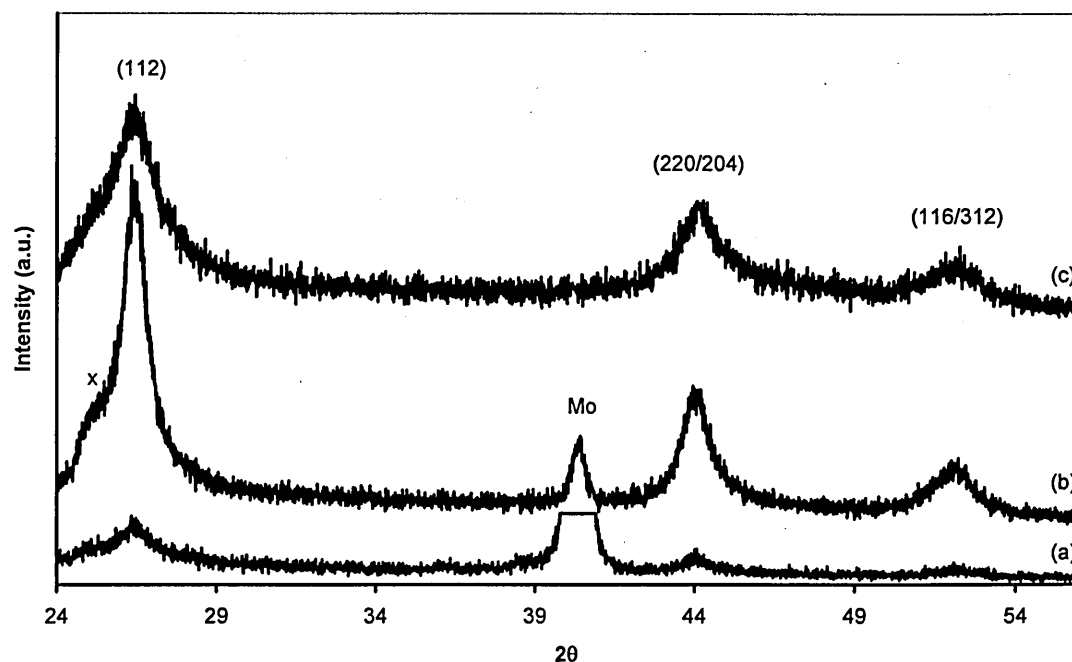


**Figure 8.16.** XRD spectra of  $\text{CuInSe}_2$  layers deposited at; (a)  $-0.476$  V for 1 minute, (b)  $-0.476$  V for 20 minutes and (c)  $-0.576$  V for 50 minutes.

### 8.8.1.1 Effect of annealing

Annealing the sample using the method described in section 8.5, shows that the material becomes very crystalline, figure 8.17 shows sharp and intense peaks for all three major peaks. The crystallite sizes were calculated using the Scherrer equation, which was found to be 5.2 nm for the as-deposited layer and 40.0 nm for the annealed layer.

The strain was calculated using the Hull equation, which is shown in figure 8.18. The as-deposited  $\text{CuInSe}_2$  sample gave a strain of  $1184 \times 10^{-3}$ , and the annealed sample was

$57 \times 10^{-3}$ . As expected the strain 'relaxes' in the annealed sample, due to any defects being 'annealed out'. The crystallite size was also calculated using the Hull equation, the results concur with the ones calculated using the Scherrer equation, with the as-deposited sample equal to 5.9 nm and the annealed sample 40.2 nm.

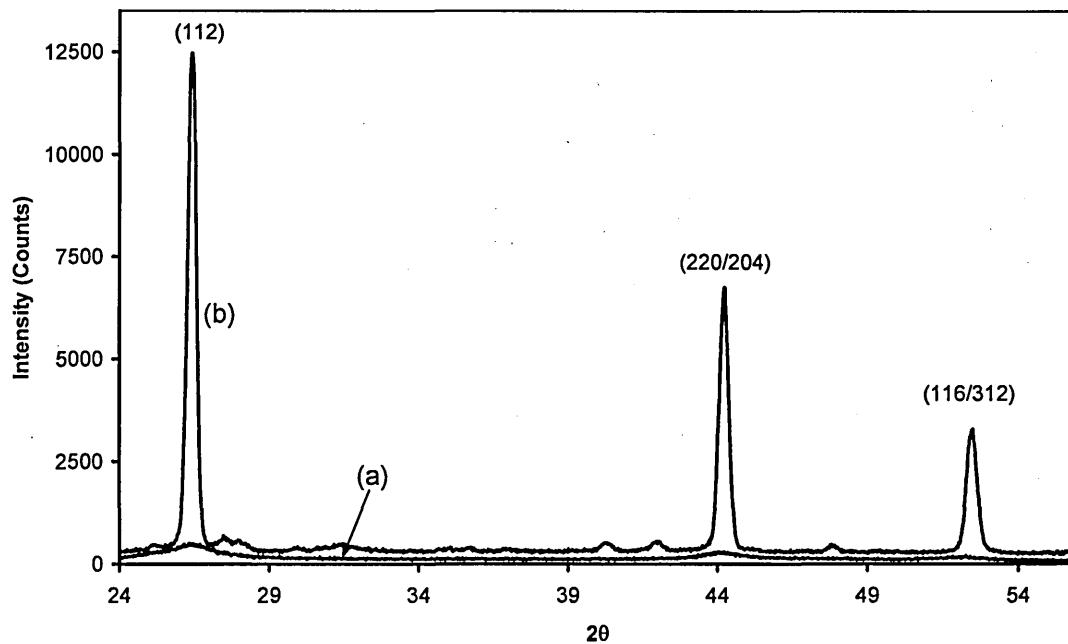


**Figure 8.17.** XRD spectra of CuInSe<sub>2</sub> layers deposited at -0.476 and -0.576 V, (a) as-deposited and (b) annealed.

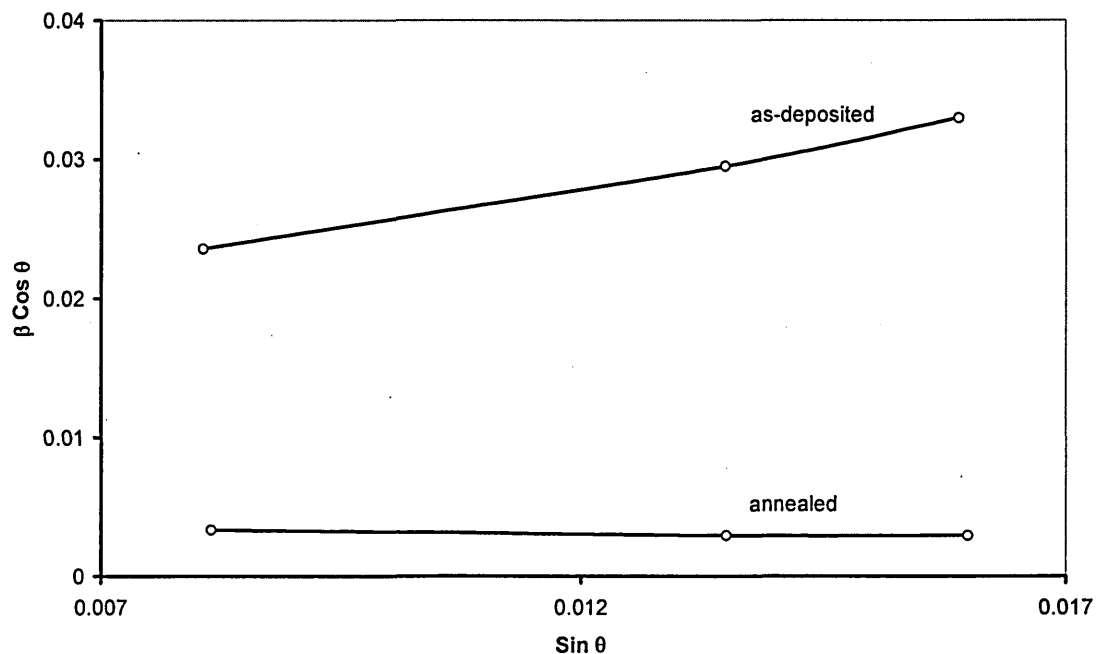


**Figure 8.18.** Graph of  $\beta \cos \theta$  vs  $\sin \theta$  for the 3 main peaks of CuInSe<sub>2</sub> sample, to calculate the strain in the samples.

The lattice parameters were also calculated for the annealed CuInSe<sub>2</sub> sample, using the (112) and (312) peaks and equation 8.1 solving for  $a$  and  $c$  simultaneously.

$$\frac{1}{d^2} = \frac{h^2 + k^2}{a^2} + \frac{l^2}{c^2} \quad (8.1)$$

The lattice parameters were calculated, giving  $a = 0.5697$  nm and  $c = 1.0102$  nm. From the standard data for CuInSe<sub>2</sub>  $a = 0.5784$  nm and  $c = 1.0161$  nm.

## 8.9 I-V characteristics

Due to time constraints and the lack of equipment for the deposition of ZnO and the metal contacts, I-V measurements were carried out using a 0.1 M KCl electrolyte contact after depositing a layer of CBD CdS. Figure 8.19 shows the device is photo-active giving;  $V_{oc} = 866$  mV and  $FF = 0.46$ . The junction formed when using an electrolyte contact is very weak, and is strongly affected by surface states, which can cause Fermi level pinning. This can produce I-V curves with varying shapes, which can often result in an 'S' shape curve. The low current densities could be attributed to the presence of active recombination and generation centres. A recent paper entitled "Effects of defects in semiconductors on reproducibility and performance of thin-film photovoltaic solar cells", by Dharmadasa et al [24], details such anomalies in I-V curves.

Devices were also measured using Showa Shell's CIGSS, which is the best commercially available material with an efficiency of 13.4%. A typical I-V curve is shown in figure 8.20, showing  $V_{oc} = 500$  mV and  $FF = 0.30$ , again current density is low. These parameters are very low for this material and are again due to the weak electrolyte junction.

However, it should be noted that this material is capable of high efficiencies as already stated. Therefore it is possible that the electrodeposited CuInSe<sub>2</sub> devices could achieve much better results if they were completed with the correct final processing steps.

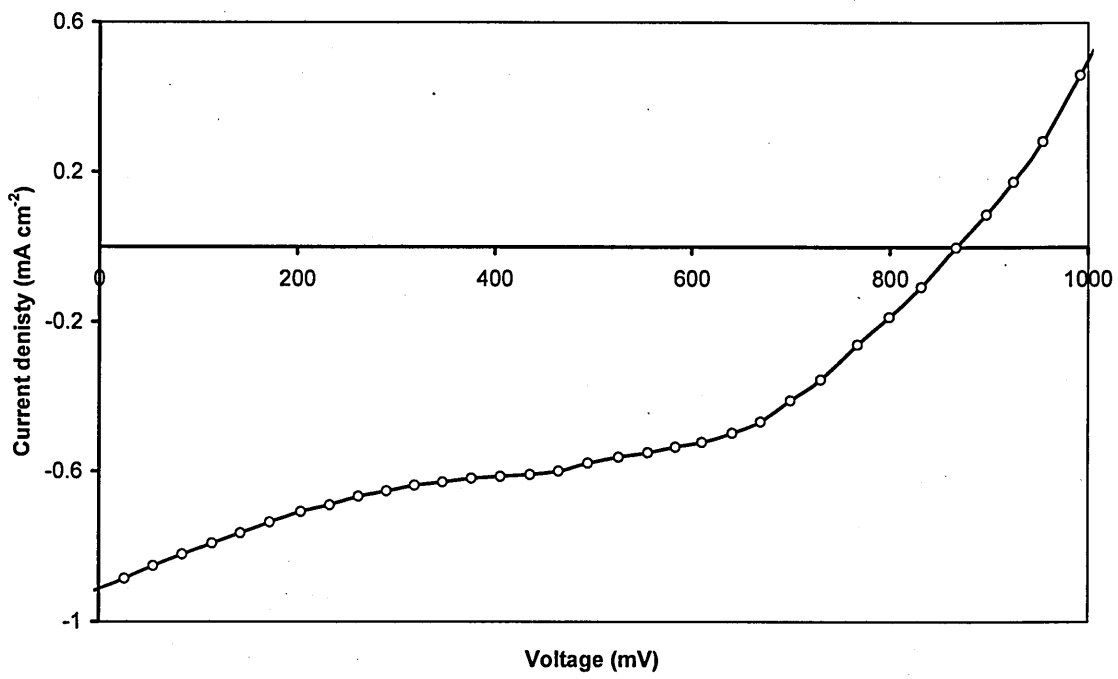


**Figure 8.19.** A typical I-V curve for a  $\text{CuInSe}_2$ /electrolyte junction.

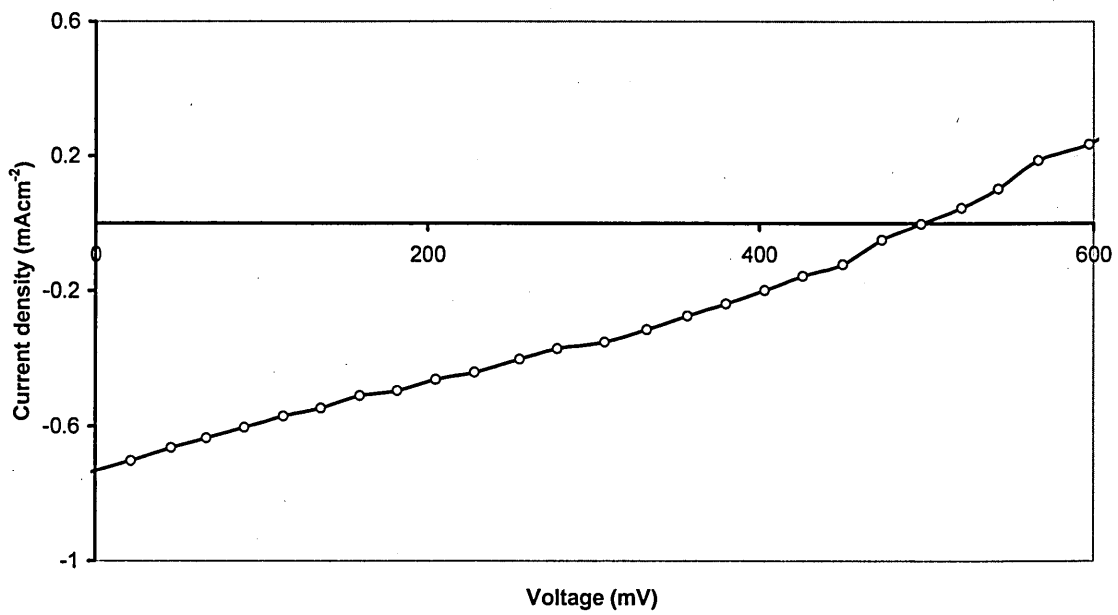


**Figure 8.20.** I-V curve measured for Showa Shell CIGSS/ electrolyte junction.

## 8.10 Discussion of results and conclusions

The results of the work reported in this section on deposition voltages, annealing time, temperature and gas flow rate, have also been reported by various other groups [144,126,145], and have produced good working devices. Lincot et al have produced 11.3% efficient devices using a one step electrodeposition technique [58].

Calixto et al [131], have also confirmed that films grown at -0.476 V for 1 minute are copper and selenium rich, with only a small amount of indium. The mechanism for why this 1 minute treatment and subsequent 20 minute growth, improves the morphology of the layer is also explained. Any pin holes formed during the initial nucleation from the 1 minute growth are filled by the restarting of the deposition (20 minute growth); this therefore reduces the number of pin holes, giving a more uniform film.

Chraibi et al [144] have also found that the best deposition potential for very nearly stoichiometric  $\text{CuInSe}_2$  is -0.570 V (vs Ag/AgCl electrode), which concur with the findings of this work and they have also reported the formation of copper selenide phases at lower negative potentials.

The  $V_{oc}$  obtained from the I-V characteristics, at 866 mV is too high for  $\text{CuInSe}_2$ , as the maximum value for  $\text{CuInSe}_2$  whose bandgap is 1.04 eV is 690 mV [58]. The high  $V_{oc}$  is possibly due to a thin oxide layer forming on the surface of the CdS. This was identified from the XRD spectra of annealed CdS as reported in chapter 6, CdO has a bandgap of 2.28 eV [128]. This oxide layer in effect forms an MIS structure, which will produce a higher open circuit voltage.

A recent paper by Contreras et al [33], reporting on the highest efficiency CIGS solar cells, achieving 19.5% efficiency, report that the optimum bandgap for CIGS solar cells is 1.14 eV and not 1.40 eV which is generally accepted for all solar cells. This has the implication that only a small amount of gallium needs to be included in the film to increase the performance vastly, which is achievable by electrodeposition.

All the results from this chapter show the material is of good quality and is comparable to other groups, who produce good working devices from single step electrodeposition. Therefore it is only the final processing steps, the ZnO layer and metal contacts that needs to be addressed, to complete the fabrication of the device.

## Chapter 9.0 Conclusions and future work

New designs of graded bandgap solar cells based on p-type window materials, using the well researched GaAs and  $\text{Al}_x\text{Ga}_{(1-x)}\text{As}$  alloy system, have been experimentally tested. A systematic exercise of scaling up was carried out from 0.5 mm diameter dots ( $0.002 \text{ cm}^2$ ) to  $3 \times 3 \text{ mm}^2$  ( $0.090 \text{ cm}^2$ ) and finally to  $5 \times 5 \text{ mm}^2$  ( $0.250 \text{ cm}^2$ ). and these were then assessed using I-V, QE and CV techniques. The devices showed  $V_{oc}$  in the range of 1070-1175 mV, exceeding reported values, FF in the range 0.80-0.87, and  $J_{sc}$  in the range 11-12  $\text{mA cm}^{-2}$ . The current density is the parameter limiting the efficiency of the device at present, which is believed to be low because of the presence of the GaAs capping layer at the front of the device. The QE results show considerable losses in both the blue and red regions of the spectrum. These losses are also attributed to the GaAs capping layer, which acts as a filter. To confirm this, a second set of devices was fabricated, replacing the GaAs cap with GaAlP, this increased the  $J_{sc}$  to  $\sim 14 \text{ mA cm}^{-2}$ ,  $V_{oc}$  and FF remained the same.

From the dark I-V curves the barrier height was estimated to be 1.38 eV, which is the reason why this device structure gives high open circuit voltages. This ability to produce high  $V_{oc}$ 's was a design feature of the new model, and hence this result is one validation of the new model. From the CV results the doping concentration was calculated to be  $4 \times 10^{17} \text{ cm}^{-3}$  and the depletion width  $0.34 \mu\text{m}$ . This would indicate that the doping concentration needs to be reduced to increase the depletion width, and hence increase the collected current of the device.

Once the problem of low current density is resolved, these cells could produce efficiencies in the range of 30-40%, as the current density obtained for crystalline GaAs cells is  $\sim 30 \text{ mA cm}^{-2}$  [7]. These new designs of cells have shown quantum efficiencies above unity [unpublished work], which will increase the current density further. EBIC could be carried out to identify the active region of the device and SIMS to look at the doping profiles.

Because these devices are grown by expensive techniques, they are not suitable for large area solar cells, but would make excellent concentrator solar cells. Work is continuing

to identify the mechanisms for the low current densities and remove it, in order to improve the device performance.

New PV device structures based on  $\text{CuInGaSe}_2$ , using the superstrate configuration have been electrodeposited from aqueous solutions from a single bath.

The compositional, structural, morphological and the electrical properties of the layers were investigated. The XRD results showed the layers to be polycrystalline, with a (112) preferential orientation of the chalcopyrite structure. The position of the XRD peaks indicated there was very little gallium incorporated into the lattice, but the XRF results detected the presence of gallium. Therefore it can be concluded that the gallium must be in a different form, possibly gallium hydroxide. SEM confirmed visual inspection that the films deposited at lower negative voltages produce dense regular films, and as the voltage was increased to more negative voltages the films become powdery and not well adhered to the substrate.

This work has shown that it is possible to grow predetermined CIGS layers with  $p^+$ ,  $p$ ,  $i$ ,  $n$  and  $n^+$  type electrical conduction by electrodeposition from a single bath and previous published work has shown that the bandgap increases as the deposition voltage increases [23]. The device structure glass/TCO/ $n$ -CdS/ $n$ -CIGS/ $i$ -CIGS/ $p$ -CIGS/metal, has shown encouraging results as the first step towards the development of low cost graded bandgap thin film solar cells, but the resulting efficiencies have been low. The devices were PV active with parameters  $V_{oc} \sim 235$  mV,  $J_{sc} \sim 22$  mA  $\text{cm}^{-2}$ , FF  $\sim 0.38$  and  $\eta \sim 2.0\%$ .

The main reason for the low efficiencies is believed to be the deterioration of the CdS when annealed at high temperatures, which is a necessary step for the re-crystallisation of the CIGS layer. This problem could be overcome by replacing the CdS with another suitable window layer, as outlined in chapter 2. Another alternative technique would be to use a rapid thermal anneal (RTA) which can anneal the CIGS layer in seconds, and may not deteriorate the CdS layer underneath, as this process only heats the surface layer.

Due to the problems annealing CdS at high temperature and the difficulty of incorporating gallium into the layer, CuInSe<sub>2</sub> cells with Mo as the substrate were deposited. Again the CIS layers were deposited by electrodeposition using a single aqueous electrolyte bath.

The compositional, structural, morphological and the electrical properties of the layers were investigated. Also to understand the mechanisms of film growth, detailed cyclic voltammetry was carried out, leading to the construction of a Pourbaix diagram for the Cu-In-Se system. It was found that depositing the films at -0.476 V for 20 minutes, followed by 50 minutes at -0.576 mV gave the best quality films, with p-type electrical conduction. The films were polycrystalline, with a strong (112) preferential orientation of the chalcopyrite structure and were copper and selenium rich. A method to anneal the CuInSe<sub>2</sub> layers without the use of H<sub>2</sub>Se was devised, and a detailed study using SEM to determine the effects of annealing time and temperature was carried out. Annealing the films at 550°C for 30 minutes in a selenium rich atmosphere produced smooth, dense, well adhered films, with a final thickness of ~2.0 μm. I-V measurements were carried out using an electrolyte contact, the devices were photo active, ( $V_{oc}$ ~866 mV,  $J_{sc}$ ~0.9 mA cm<sup>-2</sup>, FF~0.40).

The results show the material is of good quality and is comparable to other research groups, who produce good working devices from single step electrodeposition. Therefore it is possible that the electrodeposited CuInSe<sub>2</sub> devices could achieve much better results if they were completed with the correct final processing steps.

The eventual device performance could be improved further by the addition of gallium, which is added to increase the bandgap and hence the  $V_{oc}$ . However, as reported in chapter 7, incorporating gallium into the CIS lattice has proved to be difficult, one way this could be achieved is by careful control of the bath chemistry, which is an area that needs to be investigated in the future.

Also controlling impurities is an important step required to improve the final device performance. The highest purity chemicals were used for this work, but the identification of the impurities using ICPMS and the bath self purification process will ensure better device performance in the future.

## References

1. US Department of Energy, 'International Energy Outlook 2007', DOE/EIA – 0484, May 2007, <http://www.eia.doe.gov/oiaf/ieo/index.html>
2. J. W. S. Van Leeuwen and P. Smith, 'Nuclear Power the Energy Balance', <http://www.stormsmith.nl>, (2005).
3. K. S. Ong, *Renewable Energy* 28 7 (2003) 1047-1060.
4. M. A. Green, *Prog. Photovolt: Res. Appl.* 9 (2001) 123-135.
5. L. Kazmerski, *Journal of Electron Spectroscopy and Related Phenomena* 150 (2006) 105-135
6. A. Goetzberger, J. Luther, G. Willeke, *Solar Energy Materials & Solar Cells* 74 (2002) 1-11.
7. M. A. Green, K. Emery, Y. Hisikawa, W. Warta, *Prog. Photovolt: Res. Appl.* 15 (2007) 425-430.
8. M. A. Green, *Solar Energy* 76 (2004) 3-8.
9. Y. Tawada, H. Yamagishi, K. Yamamoto, *Solar Energy Materilas & Solar Cells* 78 (2003) 647-662.
10. J. Kessler, M. Bodegard, J. Hedstrom, L. Stolt. *Proceedings of the 16<sup>th</sup> European Photovoltaic Solar Energy Conference, Glasgow (2000) 2057-2060.*
11. A. Gupta and S. Isomura, *Solar Energy Materials and Solar Cells* 53 (1998) 385-401.
12. M. Kaelin, D. Rudmann, F. Kurdesau, H. Zogg, T. Meyer, A. N. Tiwari, *Thin Solid Films*, 480-481 (2005) 486-490.
13. H. W. Schock and R. Noufi, *Prog. Photovolt. Res. Appl.* 8 (2000) 151-160.

14. I. Repins, M. A. Contreras, B. Egaas, C. DeHart, J. Scharf, C. L. Perkins, B To, R. Noufi, *Prog. Photovolt: Res. Appl.* 16 (2008) 235-239.
15. K. Kushiya, *Solar Energy* 77 (2004) 717-724.
16. T. Takamoto, T. Agui, E. Ikeda, H. Kurita, *Solar Energy Materials & Solar Cells* 66 (2001) 511-516.
17. M. Yamaguchi, T. Takamoto, K. Araki, N. E. Daukes, *Solar Energy* 79 (2005) 78-85.
18. I. M. Dharmadasa, *Solar Energy Materials & Solar Cells* 85 (2005) 293-300.
19. O. Christensen, *J. Appli. Phys.* 47 2 (1976).
20. I. M. Dharmadasa, J. S. Roberts, G. Hill, *Solar Energy Materials & Solar Cells* 88 4 (2005) 413-422.
21. A. Goetzberger, C. Hebling, H. W. Schock, *Materials Science and Engineering* 40 (2003) 1-46.
22. S. M. Sze and Ng. K. Kwok, *Physics of Semiconductor Devices*, 3<sup>rd</sup> Edition, Wiley-Interscience (2007).
23. I. M. Dharmadasa, N. B. Chaure, G. J. Tolan and A. P Samantilleke, *Journal of The Electrochemical Society* 154 6 (2007) H466-H471.
24. I. M. Dharmadasa, G. J. Tolan and M. Cazaux, *Semicond. Sci. Technol.* 23 3 (2008) 035023
25. A. Luque and S. Hededus, *Handbook of Photovoltaic Science and Engineering*, Wiley, (2003).

26. R. D. Lide, CRC Handbook of Chemistry and Physics, 88<sup>th</sup> Edition, CRC, (2005).
27. A. Rockett and R. W. Birkmire, Journal of Applied Physics 70 7 (1991) R 81.
28. R. Scheer, Vacuum Science and Technology 2 (1997) 77.
29. F. Rointan, Handbook of Deposition Technologies for Films and Coatings: Science, Applications and Technology, William Andrew Publishing (1994).
30. K. Kushiya, M. Tachiyuki, Y. Nagoya, A. Fujimaki, B. Sang, D. Okumura, M. Satoh, O. Yamase, Solar Energy Materials & Solar Cells 67 (2001) 11-20.
31. A. Romeo, M. Terheggen, D. Abou-Ras, D. L. Bätzner, F.-J. Haug, M. Kälin, D. Rudmann and A. N. Tiwari, Prog. Photovolt: Res. Appl. 12 (2004) 93-111.
32. K. Ramanathan, M. A. Contreras, C. L. Perkins, S. Asher, F. S. Hasoon, J. Keane, D. Young, M. Romero, W. Metzger, R. Noufi, J. Ward, A. Duda. Prog. Photovolt: Res. Appl. 11 (2003) 225-230.
33. M. A. Contreras, K. Ramanathan, J. AbuShama, F. Hasoon, D. L. Young, B. Egaas and R. Noufi, Prog. Photovolt: Res. Appl. 13 (2005) 209-216.
34. J. A. Hollingsworth, K. K. Banger, M. H. C. Jin, J. D. Harris , J. E. Cowen , E. W. Bohannan, J. A. Switzer, W. E. Buhro , A. F. Hepp, Thin Solid Films 431-432 (2003) 63-67.
35. M. C. Artaud, F. Ouchen, L. Martin, S. Duchemin, Thin Solid Films 324 (1998) 115-123.
36. H. Metzner, J. Cieslak, J. Eberhardt, T. Hahn, M. Muller, U. Kaiser, A. Chuvilin, U. Reislohner, and W. Witthuhn, Applied Physics Letters 83 8 (2003).

37. P. K. Vidyadharan Pillai, P. K. Vijayakumar, *Solar Energy Materials and Solar Cells* 51 (1998) 47-54.
38. M. Krunk, O. Bijakina, T. Varema, V. Mikli, E. Mellikov, *Thin Solid Films* 338 (1999) 125-130.
39. K. S. Ramaiah, V. S. Raja, A. K. Bhatnagar, F. S. Juang, S. J. Chang, Y. K. Su, *Materials Letters* 45 (2000) 251-261.
40. M. Kaelin, D. Rudmann, A. N. Tiwari, *Solar Energy* 77 (2004) 749-756.
41. H. Sakata, H. Ogawa, *Solar Energy Materials & Solar Cells* 63 (2000) 259-265.
42. E. Ahmed, A. E. Hill, R. D. Pilkington and R. D. Tomlinson, *J. Phys. D: Appl. Phys.* 26 (1993) 1787-1792.
43. S. Kuranouchi, A. Yoshida, *Thin Solid Films* 33-344 (1999) 123-126.
44. S. Taunier, J. Six-Kurd, P. P. Grand, A. Chomont, O. Ramdani, L. Parissi, P. Panheleux, N. Naghavi, C. Hubert, M. Ben-Farah, J. P. Fauvarque, J. Connolly, O. Roussel, P. Mogensen, E. Mahe, J. F. Guillemoles, D. Lincot, O. Kerrec, *Thin Solid Films* 480-481 (2005) 526-531.
45. R. N. Bhattacharya, J. F. Hiltner, W. Batchelor, M. A. Contreras, R. N. Noufi, J. R. Sites, *Thin Solid Films* 361-362 (2000) 396-399.
46. A. Rockett, *Thin Solid Films* 480-482 (2005) 2-7.
47. H. A. Al-Thani, D. L. Williamson, F. S. Hasoon, M. Young, S. Asher, J. L. Alleman, M. M. Al-Jassim, NREL Report, NREL/CP-520-32254, (2002).

48. S. Duchemin, V. Chen, J. C. Yoyotte, J. Bougnot, S. M. Backwall, Proceedings of the 8th European Photovoltaic Solar Energy Conference, Florence, (1988) 1038-1042.
49. T. Nakada and T. Mise T, Proceedings of the 17th European Photovoltaic Solar Energy Conference, Munich (2001) 1027-1030.
50. T. Nakada, Y. Hirabayashi, T. Tokado, D. Ohmori, T. Mise, Solar Energy 77 (2004) 739-747.
51. D. Rudmann, D. Brémaud, A.F. da Cunha, G. Bilger, A. Strohm, M. Kaelin, H. Zogg, A.N. Tiwari, Thin Solid Films 480-481 (2005) 55-60.
52. U. P. Singha, W. N. Shafarmanb, R. W. Birkmire, Solar Energy Materials & Solar Cells 90 (2006) 623-630.
53. K. Kushiya, M. Tachiyuki, Y. Nagoya, A Fujimaki, B. Sang, D. Okumur, M. Satoh, O. Yamase, Solar Energy Materials & Solar Cells 67 (2001) 11-20.
54. D. Ohashi, T. Nakada, A. Kunioka, Solar Energy Materials & Solar Cells 67 (2001) 261-265.
55. H. M. Pathan, C. D. Lokhande, Applied Surface Science 239 (2004) 11-18.
56. A. Meeder, A. Neisser, U. Rühle, N. Meyer, Proceedings of the 22<sup>nd</sup> European Photovoltaic Solar Energy Conference and Exhibition, Milan, (2007).
57. Y. Nagoya, K. Kushiya, M. Tachiyuki, O. Yamase, Solar Energy Materials & Solar Cells 67 (2001) 247-253.

58. D. Lincot, J. F. Guillemoles, S. Taunier, D. Guimard, J. Sicx-Kurdi, A. Chaumont, O. Roussel, O. Ramdani, C. Hubert, J. P. Fauvarque, N. Bodereau, L. Parissi, P. Panheleux, P. Fanouillere, N. Naghavi, P. P. Grand, M. Benfarah, P. Mogensen, O. Kerrec, *Solar Energy* 77 (2004) 725-737.
59. O. Lundberg, M. Edoff, L. Stolt, *Thin Solid Films* 480-481 (2005) 520-525.
60. U. P. Singh, W. N. Shafarman, R. W. Birkmire, *Solar Energy Materials & Solar Cells* 90 (2006) 623-630.
61. H. W. Schock and R. Noufi, *Prog. Photovolt. Res. Appl.* 8 (2000) 151-160.
62. H. Miyazaki, R. Mikami, A. Yamada, M. Konagai, *Journal of Physics and Chemistry of Solids* 64 (2003) 2055-2058.
63. D. Liao and A. Rockett, *Applied Physics Letters*, 82 17 (2003).
64. Y. Yan, K. M. Jones, J. Abushama, M. Young, S. Asher, M. M. Al-Jassim, R. Noufi, NREL/CD-520-33586 (2003) 521.
65. D. Liao and A. Rockett, *Applied Physics Letters* 93 11 (2003).
66. I. M. Dharmadasa, J. D. Bunning, A. P. Samantilleke, T. Shen, *Solar Energy Materials & Solar Cells* 86 (2005) 373-384.
67. H. R. Moutinho, D. Albin, Y. Yan, R. G. Dhere, X. Li, C. Perkins, C. S. Jiang, B. To, M. M. Al-Jassim, *Thin Solid Films* 436 (2003) 175-180.
68. I. O. Oladeji and L. Chow, *J. Electrochem. Soc.* 144 7 (1997) 2342-2346.
69. M. A. Contreras, M. J. Romero, B. To, F. Hasoon, R. Noufi, S. Ward, K. Ramanathan, *Thin Solid Films* 403-404 (2002) 204-211.

70. D. Abou-Ras, G. Kostorz, A. Romeo, D. Rudmann, A. N. Tiwari, *Thin Solid Films* 480-481 (2005) 118-123.
71. T. Nakada, *Thin Solid Films* 361-362 (2000) 346-352.
72. V. Nadenau, D. Hariskos, H. W. Schock, M. Krejci, F. J. Haug, A. N. Tiwari, H. Zogg, G. Kostorz, *J. Appl. Phys.* 85 1 (1999) 534.
73. B. Canava, J. Vigneron, A. Etcheberry, D. Guimard, P. P Grand, J. F Guillemoles, D. Lincot, S. O. S Hamatly, Z. Djebbour, D. Mencaraglia, *Thin Solid Films* 431-432 (2003) 289-295.
74. H. W. Schock and R. Noufi, *Prog. Photovolt. Res. Appl.* 8 (2000) 151-160.
75. T. Nakada, *Jpn. J. Appl. Phys.* 37 (1998) 499-501.
76. D. Hariskos, S. Spiering, M. Powalla, *Thin Solid Films* 480-481 (2005) 99-109.
77. M. Powalla, B. Dimmler, R. Schaeffler, G. Voorwinden, U. Stein, H.-D. Mohring, F. Kessler, D. Hariskos, *Proceedings 19th European Photovoltaic Solar Energy Conference Paris, France, (2004)*
78. K. Kushiya, *Proceedings 3rd World Conference of Photovoltaic Energy Conversion, Osaka, Japan, (2003)* 319.
79. B. Dimmler, E. Gross, D. Hariskos, F. Kessler, E. Lotter, M. Powalla, J. Springer, U. Stein, G. Voorwinden, M. Gaeng, S. Schleicher, *Proceedings 2nd World Conference of Photovoltaic Energy Conversion, Vienna, Austria, (1998)* 419.
80. S. Spiering, D. Hariskos, M. Powalla, N. Naghavi, D. Lincot, *Thin Solid Films* 431-432 (2003) 359.

81. S. Spiering, A. Eicke, D. Hariskos, M. Powalla, N. Naghavi, D. Lincot, *Thin Solid Films* 451-452 (2004) 562.
82. A. Ennaoui, S. Siebentritt, M. Ch. Lux-Steiner, W. Riedl, F. Karg, *Sol. Energy Mater. Sol. Cells* 67 (2001) 31.
83. M. Bär, Ch.-H. Fischer, H.-J. Muffler, B. Leupolt, Th.P. Niesen, F. Karg, M.Ch. Lux-Steiner, *Proceedings 29th IEEE Photovoltaic Specialist Conference, New Orleans, USA, (2002)* 636.
84. M. A. Contreras, T. Nakada, M. Hongo, A. O. Pudoy, J. R. Sites, *Proceedings 3rd World Conference of Photovoltaic Energy Convention, Osaka, Japan, (2003)* 570.
85. C. Platzer-Bjfrkman, J. Kessler, L. Stolt, *Proceedings 3rd World Conference of Photovoltaic Energy Convention, Osaka, Japan, (2003)* 461.
86. H. J. Muffler, M. Baer, C. H. Fischer, R. Gay, F. Karg, M. C. Lux-Steiner, *Proceedings 28th IEEE Photovoltaic Specialist Conference, Alaska, (2000)* 610.
87. A. Romeo, R. Gysel, S. Buzzi, D. Abou-Ras, D. L. Bätzner, D. Rudmann, H. Zogg, A. N. Tiwari, *Proceedings 14th Photovoltaic Science and Engineering Conference (PVSEC-14), Bangkok, Thailand, (2004)* 705.
88. Y. Tokita, S. Chaisitsak, H. Miyazaki, R. Mikami, A. Yamada, M. Konagai, *Jpn. J. Appl. Phys.* 41 (2002) 7407.
89. D. Hariskos, M. Ruckh, U. Röhle, T. Walter, H.W. Schock, J. Hedström, L. Stolt, *Sol. Energy Mater. Sol. Cells* 41-42 (1996) 345.
90. N. Naghavi, S. Spiering, M. Powalla, B. Cavana, D. Lincot, *Prog. Photovolt. Res. Appl.* 11 (2003) 437.

91. A. Strohm, L. Eisenmann, R. K. Gebhardt, A. Harding, T. Schlftzer, D. Abou-Ras, H. W. Schock, *Thin Solid Films* 480-481 (2005) 162-167.
92. D. Hariskos, R. Menner, S. Spiering, A. Eicke, M. Powalla, K. Ellmer, M. Oertel, B. Dimmler, *Proceedings 19th European Photovoltaic Solar Energy Conference, Paris, France, (2004)*.
93. A. Ennaoui, S. Siebentritt, M. Ch. Lux-Steiner, W. Riedl, F. Karg, *Sol. Energy Mater. Sol. Cells* 67 (2001) 31.
94. W. Eisele, A. Ennaoui, P. Schubert-Bischoff, M. Giersig, C. Pettenkofer, J. Krauser, M. Lux-Steiner, S. Zweigart, F. Karg, *Sol. Energy Mater. Sol. Cells* 75 (2003) 17.
95. M. Munzel, C. Deibel, V. Dyakonov, J. Parisi, W. Riedl, F. Karg, *Thin Solid Films* 387 (2001) 231.
96. F. Engelhardt, L. Bornemann, M. Kfntges, Th. Meyer, J. Parisi, E. Pschorr-Schoberer, B. Hahn, W. Gebhardt, W. Riedl, U. Rau, *Prog. Photovolt. Res. Appl.* 7 (1999) 423.
97. Y. Ohtake, K. Kushiya, M. Ichikawa, A. Yamada, M. Konagai, *Jpn. J. Appl. Phys.* 34 (1995) 5949.
98. S. Chaisitsak, Y. Tokita, H. Miyazaki, R. Mikami, A. Yamada, M. Konagai, *Proceedings 17th European Photovoltaic Solar Energy Conference, Munich, Germany, (2001)* 1011.
99. M. Konagai, Y. Ohtake, T. Okamoto, *Mater. Res. Soc. Symp. Proc.* 426 (1996) 153.

100. T. Negami, T. Aoyagi, T. Satoh, S. Shimakawa, S. Hayashi, Y. Hashimoto, Proceedings 29th IEEE Photovoltaic Specialist Conference, New Orleans, USA, (2002) 656.
101. R. Mikami, H. Miyazaki, T. Abe, A. Yamada, M. Konagai, Proceedings 3rd World Conference of Photovoltaic Energy Conversion, Osaka, Japan, (2003) 519.
102. M. A. Contreras, B. Egaas, K. Ramanathan, J. Hiltner, A. Swartzlander, F. Hasoon, R. Noufi, Prog. Photovolt. Res. Appl. 7 (1999) 311.
103. K. Ramanathan, F. S. Hasoon, S. Smith, A. Mascarenhas, H. Al-Thani, J. Alleman, H. S. Ullal, J. Keane, P. K. Johnson, J. R. Sites, Proceedings 29th IEEE Photovoltaic Specialist Conference, New Orleans, USA, (2002) 523.
104. S. Chaisitsak, A. Yamada, M. Konagai, Res. Soc. Symp. Proc. 668 (2001) H9.10.1.
105. M. Konagai, Proceedings 14th Photovoltaic Science and Engineering Conference (PVSEC-14), Bangkok, Thailand, (2004) 657.
106. L. C. Olsen, P. Eschbach, S. Kundu, D. J. Gaspar, Proceedings 29th IEEE Photovoltaic Specialist Conference, New Orleans, USA, (2002) 652.
107. D. Gal, G. Hodes, D. Lincot, H.-W. Schock, Thin Solid Films 361-362 (2000) 79.
108. D. Hariskos, R. Herberholz, M. Ruckh, U. Röhle, R. Schäffler, H. W. Schock, Proceedings 13th European Photovoltaic Solar Energy Conference, Nice, France, (1995).
109. Electrochemistry Encyclopedia, <http://electrochem.cwru.edu/ed/encycl/art-e01-electroplat.htm>.

- 110 R. K Pandey, S. Chandra, S. N. Sahu, Handbook of Semiconductor Electrodeposition, Marcel Dekker Ltd (1996).
- 111 M. Pourbaix, Atlas of Electrochemical Equilibria in Aqueous Solutions, Pergmon Press (1996)
112. P. W. Atkins and J. De Paula, Elements of Physical Chemistry, Oxford University Press UK (2005).
113. M. E. Calixto, K. D. Dobson, B. E. McCandless, and R. W. Birkmire, Journal of Electrochemical Society, 153 6 (2006) G521-G528.
114. R. N. Bhattacharya, J. Electrochem. Soc. 130 (1983) 2040-2042.
115. B. D. Cullity and S. R. Stock, Elements of X-Ray Diffraction, 3<sup>rd</sup> Edition, Prentice and Hall (2001).
- 116 R. F. Egerton, Physical Principles of Electron Microscopy: An Introduction to TEM, SEM, and AEM, Springer (2005)
117. A. T. Hubbard, The Handbook of Surface Imaging and Visualization, CRC Press (1995)
- 118 C. R. Brundle, C. A. Evans, S. Wilson, Encyclopedia of Materials Characterisation: Surfaces, Interfaces and Thin Films, Butterworth-Heinemann (1992).
- 119 E. Lorenzo, G. L. Araujo, A. Cuevas, M Egido, J Minana, R. Zilles, Solar Electricity: Engineering of Photovoltaic Systems, Progensa (1994).
- 120 W. R. Runyan, T. J. Saffner, Semiconductor Measurements and Instrumentation, McGraw-Hill Professional (1998).
- 121 B. M. Basol, J.Appl.Phys. 55 2 (1984) 601.

122. I. M. Dharmadasa, A. P. Samantilleke, J. Young and N. B. Chaure, *Semicond. Sci. Technol.* 17 (2002) 1238-1248.
123. X. Wu, *Solar Energy* 77 6 (2004) 803-814.
124. I. M. Dharmadasa, *Prog. Crys. Growth and Charact.* 26 (1998) 249-290.
125. I. M. Dharmadasa, N. B. Chaure, A. P. Samantilleke, A. Hassan, *Solar Energy Materials & Solar Cells* 92 8 (2008) 923-928.
126. K. Takahashi, S. Yamada, T. U. Unno, D.C.621.383.51:523.9-7:  
[546.681'62'19:546. 681'19]
- 127 K. B. Sundaram, G. K. Bhagavat, *J.Phys. D: Phys.*, 14 (1981) 921-925
128. D. Soubane, A. Ihla, G. Nouet, *M. J. Condensed Matter* 9 1 (2007).
- 129 P. H. Jefferson, S. A. Hatfield, T. D. Veal, P. D. C. King and C. F. McConvillee, *Appl. Phys. Lett.* 92 (2008) 022101.
130. N. B. Chaure, A. P. Samantilleke, R. P. Burton, J. Young, I. M. Dharmadasa, *Thin Solid Films* 472 (2005) 212-216.
131. R. N. Bhattacharya and A. M. Fernandez, *Solar Energy Materials & Solar Cells* 76 (2003) 331-337.
132. M. E. Calixto, K. D. Dobson, B. E. McCandless, and R. W. Birkmire, *Journal of The Electrochemical Society* 153 6 (2006) G521-G528.
133. R. P. Raffaele, J. G. Mantovani, S. G. Bailey, A. F. Hepp, E. M. Gordon, R. Haraway, *NASA/TM-97-206322* (1997).

134. C. Guillén, M. A. Martínez, J. Herrero, *Vacuum* 58 (2000) 594-601.
135. D. Braunger, D. Hariskos, G. Bilger, U. Rau, H. W. Schock, *Thin Solid Films* 361-362 (2000) 161-166.
136. M. C. F. Oliveira, M. Azevedo, and A. Cunha, *Thin Solid Films*, 405 (2002) 129.
137. I. M. Dharmadasa and J. Haigh, *Journal of The Electrochemical Society*, 153 (2006) G47-G52.
138. A. M. Fernández and R. N. Bhattacharya, *Thin Solid Films* 474 1-2 (2005) 10-13.
139. M. E. Calixto, K. D. Dobson, B. E. McCandless, R. W. Birkmire, *Mater. Res. Symp. Proc*, 865 (2005) F14-17.
140. M. C. F. Oliveira, M. Azevedo, and A. Cunha, *Thin Solid Films* 405 (2002) 129.
141. K. K. Mishra and K. Rajeshwar, *J. Electroanal. Chem.* 271 (1989) 279-294.
142. F. A. Kröger, *J. Electrochem. Soc.* 125 (1978) 2028.
143. <http://www.hse.gov.uk/ria/chemical/h-selen.htm>.
144. E. K. Ejigu, Thesis, <http://etd.rau.ac.za/theses/available/etd-08292005-091710/restricted/Thesislza.pdf>
145. F. Chraibi, M. Fahoume, A. Ennaoui, J. L. Delplancke, M. J. *Condensed Matter* 5 1 (2004).

## List of Publications

### Journal papers:

I. M. Dharmadasa, G. J. Tolan and M. Cazaux, "Effects of defects in semiconductors on reproducibility and performance of thin-film photovoltaic solar cells", *Semicond. Sci. Technol.* 23 (2008) 035023 (10pp)

I. M. Dharmadasa, N. B. Chaure, G. J. Tolan, and A. P. Samantilleke, "Development of p<sup>+</sup>, p, i, n, and n<sup>+</sup>-Type CuInGaSe<sub>2</sub> Layers for Applications in Graded Bandgap Multilayer Thin-Film Solar Cells", *Journal of The Electrochemical Society*, 154 , (6) (2007) H466-H471.

A. B. M. O. Islam, N. B. Chaure, J. Wellings, G. J. Tolan, I. M. Dharmadasa, "Development of electrodeposited ZnTe layers as window materials in ZnTe/CdTe/CdHgTe multi-layer solar cells", *Materials Characterisation* (2008), doi:10.1016/j.matchar.2008.07.009.

### Conference papers:

G. J. Tolan, N.B . Chaure, S. N. Heavens, I. M. Dharmadasa, "Development of p,i and n-Type Layers for Applications in Thin Film Solar Cells", *Proceedings 22<sup>nd</sup> European Photovoltaic Solar Energy Conference and Exhibition, Milan, Italy (2007).*

I. M. Dharmadasa, G. J. Tolan, J .S. Roberts, G. Hill, S. Ito, P. Liska and M. Grätzel, "The Reproducibility, Uniformity and Scalability of Multi-Layer Graded Bandgap Solar Cells Structures Based on GaAs/AlGaAs System", *Proceedings 21<sup>st</sup> European Photovoltaic Solar Energy Conference and Exhibition, Dresden, Germany (2006).*

### Submitted:

I. M. Dharmadasa, G. J. Tolan, S. Kalyanaratne, S. Ito, P. Liska, M. Grätzel, G .Hill and J. S. Roberts, "Graded bandgap PV solar cell designs to minimise losses and maximise performance", *Semicond. Sci. Technol.* (2009).